TARDEC

--- TECHNICAL REPORT ---

No.

Interface Defeat of Long Rods Impacting Borosilicate Glass Experimental Results

Contract: W56HZV-06-C-0194
SwRI Report 18.12544/009

Prepared for
U.S. Army RDECOM-TARDEC
AMSRD-TAR-R
Warren, MI 48397-5000

February 2009

THE NATIONS'S LABORATORY FOR ADVANCED AUTOMOTIVE TECHNOLOGY

WINNER OF THE 1995 PRESIDENTIAL AWARD FOR QUALITY

U.S. Army Tank Automotive Research,
Development, and Engineering Center
Detroit Arsenal
Warren, Michigan 48397-5000

Interface Defeat of Long Rods Impacting Borosilicate Glass Experimental Results

Charles E. Anderson, Jr.

Thilo Behner

Dennis L. Orphal

Timothy J. Holmquist

Volker Hohler

Matthias Wickert

Prepared for

February 2009

REPORT DOCUMENTATION PAGE	UNCLASSIFIED	*Form Approved* OMB No. 0704-0188

Public reporting burden for this collection of information is estimated to average 1 hour per response, including the time for reviewing instructions, searching data sources, gathering and maintaining the data needed, and completing and reviewing the collection of information. Send comments regarding this burden estimate or any other aspect of this collection of information, including suggestions for reducing this burden to Washington Headquarters Service, Directorate for Information Operations and Reports, 1215 Jefferson Davis Highway, Suite 1204, Arlington, VA 22202-4302, and to the Office of Management and Budget, Paperwork Reduction Project (0704-0188) Washington, DC 20503.
PLEASE DO NOT RETURN YOUR FORM TO THE ABOVE ADDRESS.

1. REPORT DATE (DD-MM-YYYY) February 2009	2. REPORT TYPE Technical	3. DATES COVERED (From - To) 07/07 – 01/09

4. TITLE AND SUBTITLE	5a. CONTRACT NUMBER W56HZV-06-C-0194
Interface Defeat of Long Rods Impacting Borosilicate Glass Experimental Results	5b. GRANT NUMBER
	5c. PROGRAM ELEMENT NUMBER

6. AUTHOR(S)	5d. PROJECT NUMBER 18.12544
Charles E. Anderson, Jr.[1], Thilo Behner[2], Dennis L. Orphal[3], Timothy J. Holmquist[4], Volker Hohler[2], , and Matthias Wickert[2]	5e. TASK NUMBER
	5f. WORK UNIT NUMBER

7. PERFORMING ORGANIZATION NAME(S) AND ADDRESS(ES) [1]Southwest Research Institute, P.O. Drawer 28510, San Antonio, TX 78238; [2]Fraunhofer Institut fur Kurzzeitdynamik (Ernst-Mach-Institut), Eckerstr. 4, 29104 Freiburg, Germany; [3]International Research Associates, 4450 Black Ave, Pleasanton, CA 94566; [4]Southwest Research Institute, 5353 Wayzata Blvd., Minneapolis, MN 55416	8.PERFORMING ORGANIZATION REPORT NUMBER 18.12544/009

9. SPONSORING/MONITORING AGENCY NAME(S) AND ADDRESS(ES) US Army Tank-Automotive Research, Development, and Engineering Center, Warren, MI 48397-5000	10.SPONSOR/MONITOR'S ACRONYM(S) RDECOM-TARDEC
	11.SPONSORING/MONITORING AGENCY REPORT NUMBER

12. DISTRIBUTION AVAILABILITY STATEMENT

Approved for Public Release; Unlimited Distribution

13. SUPPLEMENTARY NOTES
The views, opinion, and/or findings contained in this report are those of the authors and should not be construed as an official Department of the Army position, policy, or decision, unless so designated by other documents.

14. ABSTRACT

Dwell and interface defeat for a brittle material without any lateral confinement was investigated experimentally. Reverse impact experiments with gold rods and borosilicate glass targets without and with a small Cu buffer on top of the glass were performed. Simultaneous flash X-rays and a high-speed optical camera recorded the results of the impacts. Results show that the Cu buffer increases the velocity required for penetration by a factor of ≈ 2. The dwell-penetration velocity is estimated to be 850 ± 50 m/s. Stable dwell is possible for impact velocities up to 890 m/s; whereas without a Cu buffer, penetration starts at impact velocities ≈ 450 m/s with only a short dwell phase after impact. It was also found that no dwell exists above an impact velocity of 896 ± 6 m/s. For experiments where dwell transitioned to penetration, the post-dwell penetration velocity is the same as the penetration velocity where there is little or not dwell.

15. SUBJECT TERMS
interface defeat, dwell, borosilicate glass, long-rod penetration, penetration velocity, consumption velocity

16. SECURITY CLASSIFICATION OF: Unclassified, Unlimited Distribution			17. LIMITATION OF ABSTRACT	18. NUMBER OF PAGES	19a. NAME OF RESPONSIBLE PERSON Dr. Douglas Templeton
a. REPORT Unlimited	b. ABSTRACT Unlimited	c. THIS PAGE Unlimited	None	140	19b. TELEPONE NUMBER (Include area code) 586-574-5325

UNCLASSIFIED

Table of Contents

List of Figures

Page

List of Figures (Cont'd)

List of Figures (Cont'd)

List of Tables

Page

x

1.0 Introduction

The phenomena of dwell and interface defeat continue to be of major interest as they may provide significant improvement to armor systems. Dwell occurs when a high-velocity projectile impacts a target and flows out radially along the surface of the target with no significant penetration. When the projectile is completely eroded at the surface it is referred to as interface defeat. As the impact velocity is increased, there is a point at which dwell is not maintained and penetration occurs; this impact velocity is called the dwell-penetration transition velocity, V_t, and is a function of projectile material, projectile configuration, impact velocity, and target configuration. The phenomenon of interface defeat and, in particular, the transition velocity from dwell to penetration, is not well understood. Researchers have developed very complicated targets with lateral confinements, backings, and different types of cover plate systems and have attributed interface defeat to a large variety of geometric properties, confinement, and hypothesized mechanics [1-4].

Typically, dwell and interface defeat are associated with ceramics, but the authors observed dwell on glass targets during a research study to investigate and to quantify the penetration performance of glass [5-8]. The objective of the present work is to investigate dwell and interface defeat for a brittle material, that is, glass, without any lateral confinement. This eliminates the effect of target configuration so that dwell becomes more of a material property. Consequently, other target configurations, e.g., a cover plate and/or confinement, can then be assessed against this "bare dwell" configuration. The surface stress associated with the transition velocity, for such a bare target, might be considered to be a fundamental property of the specific target material. Borosilicate glass was selected for this research in order to complement and extend the previous borosilicate glass work with the objective of providing further insights into dwell and interface defeat. A major advantage of glass is that it is transparent to light; and therefore, high-speed photography provides another diagnostic tool for studying the phenomena.

Holmquist, *et al.* [9], demonstrated that a copper buffer, attached to the surface of a ceramic, eliminated the high stress produced from the impact shock and allowed for gradual loading of the ceramic. This resulted in a significant increase in the dwell-penetration transition velocity. Thus, another objective is to investigate the effect of the buffer on the transition velocity from dwell to penetration.

Cylindrical borosilicate glass samples were launched in the reverse ballistic mode against stationary gold rods. Penetration/dwell of the gold rod was monitored with 5 flash X-ray tubes. Additionally, a 16-frame high-speed camera was used to visualize the failure propagation in the glass. Impact velocities ranged from 400 to 920 m/s.

Previous work [8] showed that the penetration and consumption velocities for a gold rod into borosilicate glass were linear functions of the impact velocity:

$$u = 0.7539 \text{v}_p - 0.2155 \tag{1}$$

$$\text{v}_c = 0.2493 \text{v}_p + 0.2077 \tag{2}$$

where v_p is the impact velocity, and u and v_c are the penetration and consumption velocities, respectively.[1] The units for the velocities are km/s. These data were obtained between ~450 m/s and 2450 m/s; however, it is noted that only three experiments were conducted with an impact velocity below 1000 m/s. This is important in comparisons with the previous data since the highest impact velocity in the experiments reported here is 900 m/s.

---

[1] Technically, the consumption velocity is negative since the length of the rod decreases with time. It is convenient to think of v_c as a positive number; therefore, we define the time change in rod length as $\dot{L} \equiv -v_c$, where the dot denotes the derivative with respect to time.

2.0 Experimental Set-Up

2.1 Glass Targets and Copper Buffer

The borosilicate glass targets were cylinders with diameter D = 20-21 mm and a length of 60 mm (Fig. 1). The material properties for the glass are given in Table 1.

A cylindrical Cu buffer with a nominal height of 2.5 mm and a diameter from 4 to 5 mm (E-Cu-57, 99.9%, UTS 300-350 MPa, and elongation 10%) was glued to the glass with Loctite 3430 epoxy resin. The bonding gap was below measuring accuracy (< 10 µm or ½ mil). The purpose of the buffer was to attenuate the initial impact shock and provide ramp stress loading on the glass surface [9]. To evaluate the performance of the relatively small buffer, some tests were done with a Cu cover plate of the same material and height as the buffer; the cover plate covered the whole diameter of the glass. Additional tests without a Cu buffer were also performed to obtain reference values of interface defeat for completely bare targets.
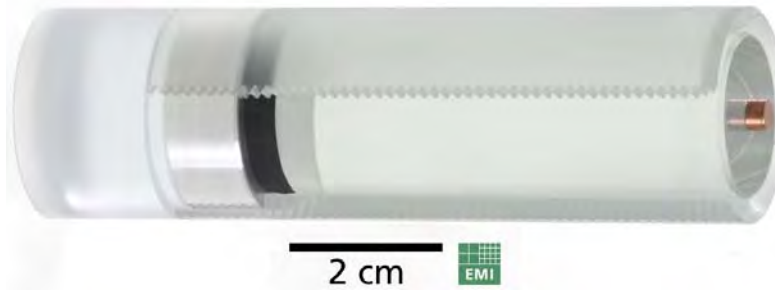
Figure 1. Borosilicate glass target in sabot with attached Cu buffer.

Table 1. Material Properties for Borosilicate Glass (Borofloat$^®$ 33 made by Schott).

Density [g/cm^3]	Young's modulus [GPa]	Knoop hardness [kp/mm^2]	Poisson's Ratio	Longitudinal wave speed [km/s]	Transverse wave speed [km/s]	HEL [10] [GPa]
2.2	64	480	0.2	5.69	3.48	8

2.2 Projectiles

The projectiles were made of pure gold (99.99%) and had a diameter of d = 1 mm and a length L = 70 mm with the following material properties: density ρ_p = 19.3 g/cm³; hardness 65 HV5; UTS 220 MPa, and elongation 30%. The projectiles were suspended from a Styrofoam holder, and then aligned with a laser.

2.3 Reverse Ballistic Test Methodology

The reverse ballistic method was used in conducting the experiments. The impact and dwell process was observed simultaneously with five, independently timed, 180-kV flash X-rays, and an IMACON 200 high-speed optical camera that took 16 pictures to visualize failure propagation inside the glass. The X-ray film was placed 200 mm from the trajectory inside the tank and had the shape of a circular segment. The light flash for background illumination of the glass and the

camera itself were mounted outside the tank. A vellum-type paper was used between the light source and the glass specimen to provide a diffuse background light. A diffused light source was found to produce better images for analysis of the failure front position. The camera and the five flash X-ray tubes were triggered using a laser positioned about 10 mm in front of the Au rod. A second laser, positioned about 350 mm in front of the Au rod, triggered the light flash.

Figure 2 shows the arrangement for the impact tank. The tests were performed with a powder gun, using a separating sabot to launch the glass targets. The Au rod was aligned in the trajectory by laser light reflection from the blunt nose of the rod with yaw angles $< \pm 0.1°$. The rear of the rod was inserted in a Styrofoam holder which allowed adjustment in three dimensions. The rod was positioned about 2 m from the gun muzzle to keep the yaw angle of the glass sample as small as possible, but still permit sabot separation.

The time measurements for the flash X-ray pictures are very accurate (better than ± 5 ns). Thus, the error for the velocities determined from the X-ray pictures rest in the accuracy of the position measurement, which is in the order of ± 0.10 to 0.15 mm. The camera pictures show that the error of the failure front velocity is dominated by irregularities in the shape of the failure front, which are of the order of $< \pm 0.2$ mm. Since the camera and X-rays were triggered on the same time base, the calculated time of impact should be the same for both image sources. The majority of tests showed a difference between these two measures of impact times of less than ± 0.25 µs (250 ns), which is inside the normal measurement error.
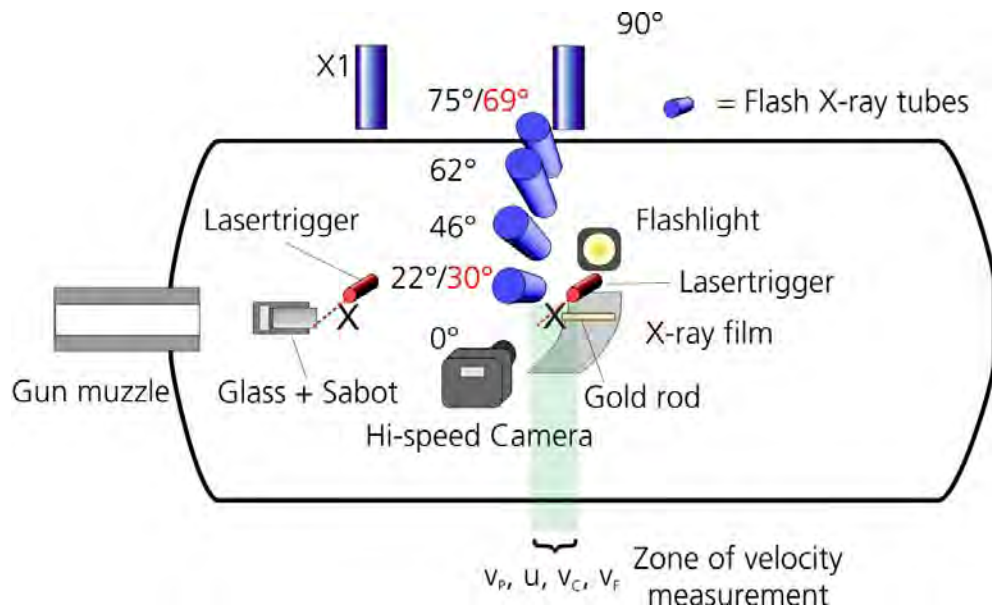
Figure 2. Test setup – modified angles of X-ray tubes for Exp. 11107-11116 in red.

3.0 Experimental Results

3.1 Optical and X-ray Images

The high-speed camera and flash radiography provide the images that are necessary to determine the position time-data for the failure front and the eroding rod. An example for an experiment that shows dwell followed by rod penetration is shown in Fig. 3. The dwell-penetration process is captured at an early and a late stage of rod erosion, with the corresponding picture pairs taken at nearly the same time after impact. While the X-ray images show the position of the gold rod in respect to the glass surface, the optical pictures visualize failure inside the glass.
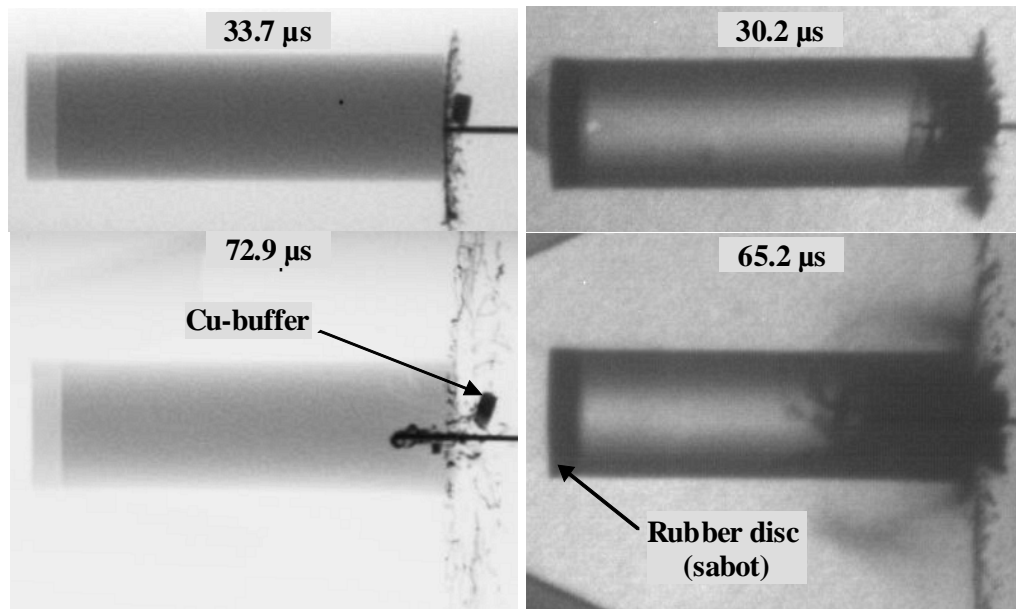
Figure 3. X-ray images (left) and camera pictures (right) for Exp. 10861
(v_p = 816 m/s); times after impact.

3.2 Evaluation of Position-Time Data

An example of the position-time data from the flash X-rays and the high-speed camera is shown in Fig. 4 (the same experiment as shown in Fig. 3). The squares denote the position of the rod nose at the corresponding time after impact. The diamonds represent the position of the *leading edge* of the failure front as determined from the optical camera. For clarity, the length of the rod, which was measured independently, is not shown in this figure. In this experiment, there is a dwell phase followed by a penetration phase. The vertical gray "bar" centered at 49.2 μs denotes the transition from dwell to penetration. The open square plotted at t = 5.45 μs indicates the estimated time at which the rod, after penetrating through the copper buffer, reached the glass interface. How these two times are estimated, as well as how the solid and dashed regression lines are calculated, are described in the following paragraphs.

For experiments that showed a dwell phase, followed by penetration, the rod penetration velocity u and consumption velocity v_c were calculated by a linear regression of the nose
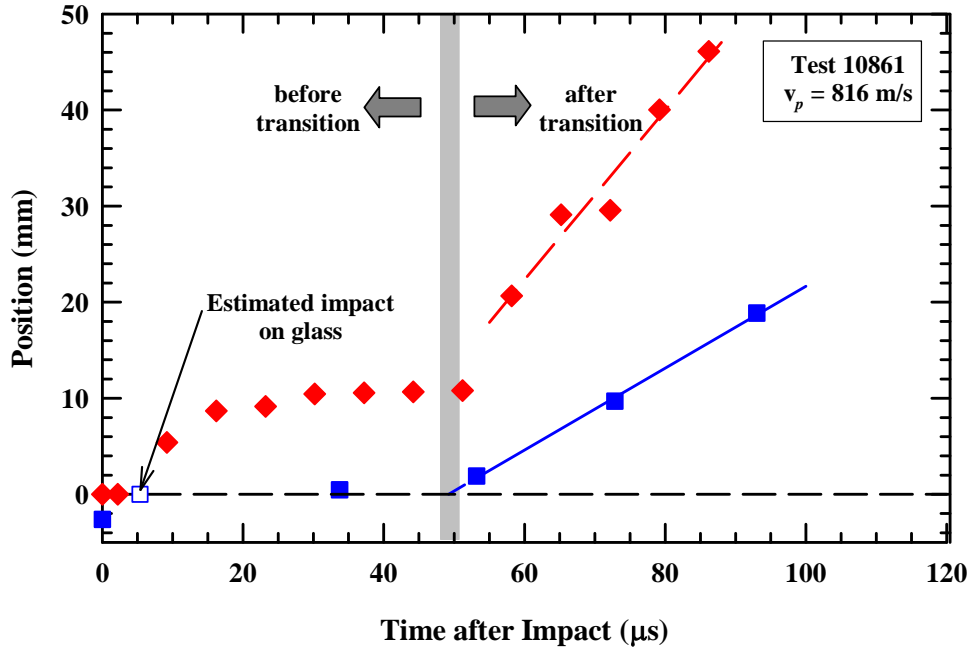
Figure 4. Example of position-time data from the X-rays and high-speed camera, Exp. 10861.
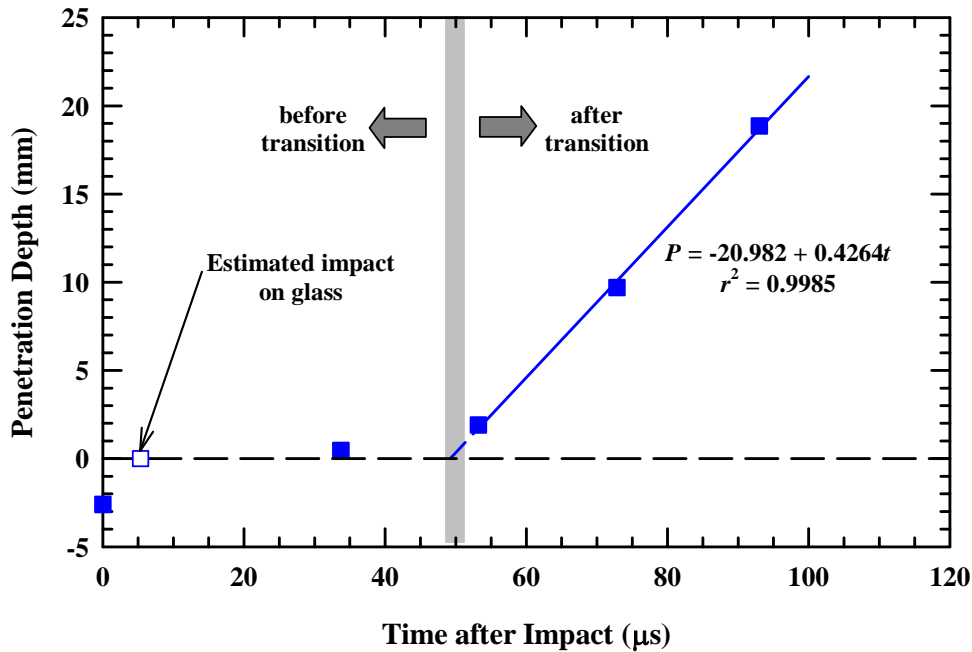
Figure 5. Determination of penetration velocity u for Exp. 10861 (u = 426 m/s), and estimate of the time for onset of penetration.

position and length of the rod over the trigger time of each X-ray image. The penetration-time data shown in Fig. 4 are replotted in Fig. 5. The slope of the regression line[2] is the penetration velocity, u. The consumption velocity, v_c is determined similarly from measurements of the length of the rod versus time (but not shown here). For experiments that showed sustained dwell

---

[2] The units for all regression fits are mm/μs (or km/s) for velocity, and microseconds for time.

until the glass hit the Styrofoam support of the rod, the penetration velocity u is 0, and consequently, v_c should equal the impact velocity v_p. However, as will be discussed later, there are several instances that "sustained dwell" might have resulted in a millimeter or so of penetration; and in these cases, $v_c \neq v_p$, since v_c can be determined independently from the rod length versus time data.

An estimate of when penetration into the glass begins can be made from that regression (x-axis intercept of the regression line). In the example of Fig. 5, it is estimated that penetration began 49.2 µs after impact. However, impact (time = 0) is measured from impact on the leading face of the Cu buffer, which for this experiment, was 2.6-mm high. If simple hydrodynamic penetration theory is used (since the Cu buffer and the Au rod have very low strength), then the time it takes for the projectile to penetrate through the Cu buffer and reach the Cu-glass interface is given by:

$$t_{Cu} = \frac{h}{v_{hydro}}$$
(3)

$$v_{hydro} = \frac{v_p}{1 + \sqrt{\rho_t / \rho_p}}$$
(4)

where h is the height of the buffer, and ρ_t and ρ_p are the target and projectile densities, respectively. The open square—at 5.4 µs—denotes the time calculated from Eqns. (3) and (4).[3] Thus, for Exp. 10861, the Au rod dwelled for approximately 44 µs on the glass surface before transitioning to penetration.

The camera pictures provide an optical assessment of overall glass failure during dwell and can be used to determine the position of the failure front inside the glass. The region where the glass becomes opaque is interpreted as failed material, similar to previous analyses [5-8]. The position of the failure front versus time, shown in Fig. 3, is replotted in Fig. 6.

While penetration of the rod inside the glass is nearly linear with time (steady-state) for all observed experiments, the propagation velocity of the failure front, v_F, can show an erratic non-linear behavior for the v_p range considered here (Fig. 6). The non-linearity results in a smaller correlation coefficient (r^2) and a larger standard error than determined from the experiments reported in Ref. [8], which were conducted at higher impact velocities.

When dwell occurs, there are often only 1 or 2 frames in which the initial propagation of the failure front (FF) can be detected right after the rod hits the glass before the FF comes to a standstill, about 7-10 mm inside the glass for the rest of the dwell phase, e.g., see Fig. 6. In those cases when only 1 to 2 frames show the initial FF propagation, a determination of that first v_F is not made. Additionally, there is an indication that the dark area of the glass, which is normally associated with the FF, may be associated with a spall torus, and thus the result of a different

---

[3] Clearly this is an approximation. The initial penetration velocity, because of the shock pressure, will be higher than the hydrodynamic penetration velocity. On the other hand, as the projectile-target interface nears the glass surface, the penetration resistance will increase, thereby decreasing the penetration velocity below that of the hydrodynamic velocity. These two effects are off-setting. Further, the buffer thickness is only ~2.5 rod diameters. Therefore, it is believed that Eqns. (3) and (4) provide a reasonable estimate for the rod nose to reach the glass surface.
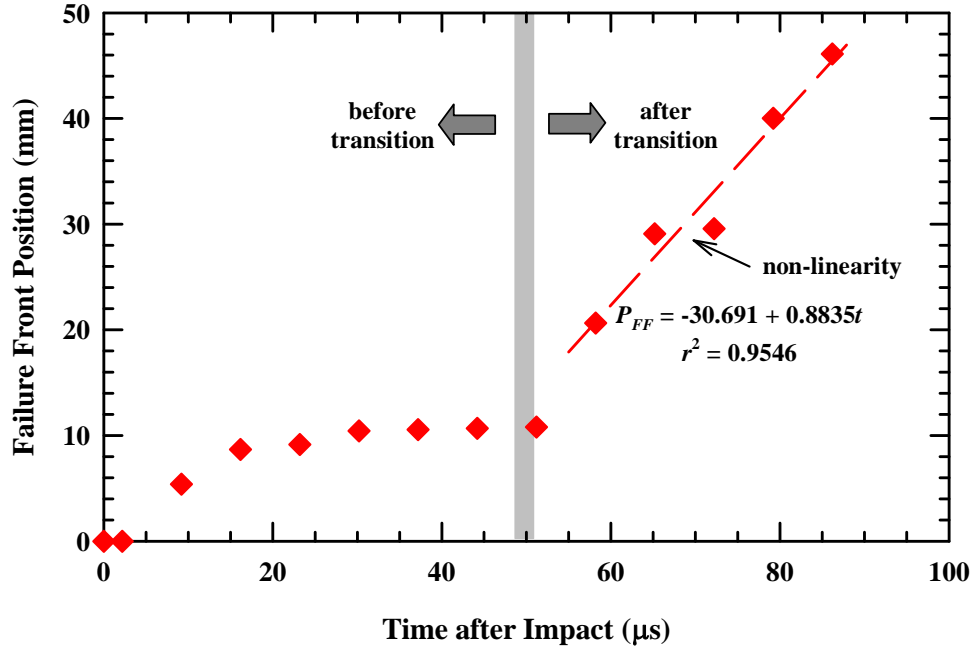
Figure 6. Position of the failure front inside glass (Exp. 10861, v_F= 884 m/s after transition, standard error 111 m/s, v_F before transition could not be determined).

type of failure mechanism, and not a propagating FF as defined in earlier research, e.g., Ref. [8]. This is discussed further in Section 4.5.2.

For a few tests, there was a long dwell period, but a little penetration in the last X-ray image, such as shown in Fig. 7. To estimate the time for the onset of penetration, it was assumed that the penetration velocity after transition is given by Eqn. (1). The estimate for when penetration began for the experiment shown in Fig. 7 is 58.5 μs. Thus, since it took approximately 5.5 μs for the rod to penetrate the buffer to the glass surface, it is estimated that the rod dwelled for 53 μs before it began to penetrate.

There are several other features concerning Fig. 7 that are relevant to analysis of the data. The first data point for the position of the tail (that is, the initial rod length) cannot be used to compute the consumption velocity during dwell for targets that have a copper buffer since the rod erodes during penetration of the copper. The next two data points allow an estimate of the consumption velocity, which is 759 m/s during dwell. Note that calculated consumption velocity is not precisely equal to the impact velocity of 770 m/s (this will be discussed further in Sections 4.5.2 and 4.7). There are not sufficient data in this experiment to estimate the consumption velocity after the onset of penetration since penetration begins sometime between the 3rd and last X-ray image. Nevertheless, it can be seen that that slope of the tail length—the consumption velocity—changes significantly between the 2nd and 3rd X-ray images, and the 3rd and 4th images.

It is somewhat subjective which camera images to select for computing an estimate of the failure front velocity. The dashed line through the diamond data points denotes the range of data used to estimate v_F. Although it appears that something happened about 40 μs since there was a jump in the position of the failure front, the flash X-ray image at 48.4 μs indicates no (or very little) penetration prior to 48 μs. Further, it was observed in experiments with short rods [11-12] that it takes a finite amount of time before there is communication between the rod front
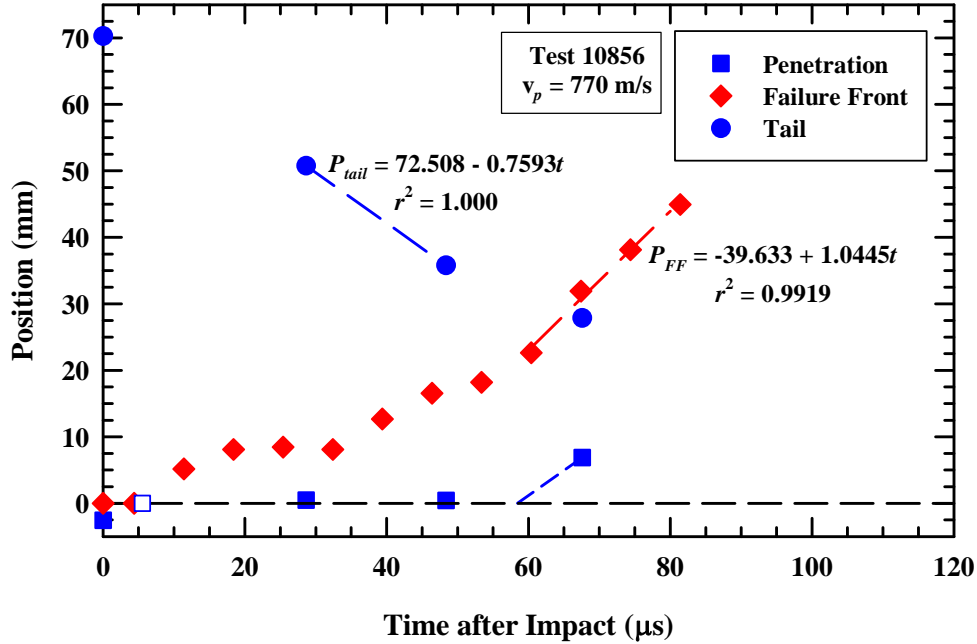
Figure 7. Example of extended dwell with last X-ray showing penetration.

and the leading edge of the failure front. Thus, we have elected to include only data points after the onset of penetration and where the position-time data are fairly linear for estimating the failure front velocity after transition.

3.3 Experimental Data

In total 24 experiments were performed: 4 experiments with a bare glass target[4], 17 experiments with a glass target with a small Cu-buffer (10 with a 4-mm diameter buffer, and 7 with a 5-mm diameter buffer), and 3 experiments of a glass target with a Cu cover plate. The target response was classified in 3 groups:

- **sustained dwell** – no penetration could be detected (combined X-ray and optical confirmation);

- **transition** – a dwell phase of variable length followed by penetration;

- **penetration** – immediate penetration upon impact or a very short dwell phase of only a few microseconds (estimated dwell times of less than 8 μs).

For some of the experiments with a very long dwell period, it was somewhat subjective about whether the classification should be sustained dwell or transition. If there was virtually no movement of the failure front (after the initial propagation of approximately 7-10 mm) over the timeframe of the experiment, then the experiment was categorized as sustained dwell.

The experiments are listed by type and target response in Table 2. Test results are sorted by increasing impact velocity v_p within each group. Table 3 provides a succinct definition of the symbols used in the Table 2, as well as some of the other symbols used throughout the report. The flash X-ray images, camera images, and position-time graphs of the data (similar to Fig. 7)

---

[4] In addition, two experiments on bare targets from previous experiments [8] are included in the analysis.

are given in Appendix A. The times of the flash X-rays and camera images, relative to impact, are provided in Tables A-1 and A-2, respectively.[5] The images are ordered by the categorization of Table 2. Measurements from the X-ray shadowgraphs and the camera images are given in Table A-3.

Table 2. Experimental Results

Exp.	Yaw [°]	oc [mm]	d_{Cu} [mm]	v_p [m/s]	Target Response	Before transition			After transition		
						u [m/s]	v_c [m/s]	v_F [m/s]	u [m/s]	v_c [m/s]	v_F [m/s]
11107	0.7	1.5	-	386±1	sust. dwell	0	384±2	-	-	-	-
11108	2.1	0.4	-	441±1	sust. dwell	0	439±3	-	-	-	-
11110	1.0	0.4	-	463±2	trans.	-	392	-	167±1	283±9	532±67
11109	0.8	0.4	-	475±3	pen.	-	-	-	164±4	301±8	761±55
10850	0.9	1.9	4	583±1	sust. dwell	0	560±5	-	-	-	-
10853	0.9	1.0	4	649±5	sust. dwell	0	603±4	-	-	-	-
10854	1.8	0.6	4	720±1	sust. dwell	0	703±7	-	-	-	-
10858	0.3	0.8	5	782±3	sust. dwell	0	758±10	-	-	-	-
11111	1.0	0.0	5	800±2	sust. dwell	0	784±9	-	-	-	-
10862	0.4	1.7	5	890±5	sust. dwell	0	868±9	-	-	-	-
10852	1.6	1.9	4	616±2	trans.	-	598	-	-	-	-
10856	1.8	1.6	4	770±3	trans.	-	759	-	-	-	1044
10861	0.6	2.0	5	816±5	trans.	-	-	-	426±17	369±22	884±111
10860	0.7	1.1	5	821±3	trans.	-	-	-	487±8	330±4	998±63
10859	0.5	0.8	5	837±4	trans.	-	-	-	477±14	357±11	924±37
11112	1.2	1.2	4	869	trans.	-	-	-	510	331	1018±122
10863*	1.6	0.5	4	882±4	trans.	-	819±2	-	336	-	-
10851	0.2	2.0	4	611±2	pen.	-	-	-	302±11	301±5	744±60
10857	0.9	1.6	4	784±5	pen.	-	-	-	431±4	337±7	1014±68
10855	2.6	1.8	4	794±7	pen.	-	-	-	437±14	337±9	937±154
11114	0.9	1.5	5	902±3	pen.	-	-	-	481±10	409±20	1049±103
11116	0.8	0.2	20	856±2	trans.	-	862	-	436	401	881±62
11113	0.5	0.8	20	889±3	trans.	-	887	-	490	393	853±57
11115	0.0	0.8	20	912±1	pen.	-	-	-	494±16	414±40	1029±98

Yaw: combined horizontal and vertical yaw
Exp. 10863: with a very long dwell phase this Exp. could also be regarded as sustained dwell.

The penetration and consumption (erosion) velocities, u and v_c, respectively, and the failure front velocity, v_F were calculated for each experiment, subject to the procedures described in Section 3.2. These values are calculated in two time domains: 1) before transition (i.e., for the dwell phase), and 2) after transition (i.e., when penetration of the rod into glass occurs). The regression fits, from which the slopes and standard errors were derived, are shown in the figures in the appendix, along with the square of the correlation coefficient. The slopes of the position-time curves, i.e., the velocities, along with the standard errors are listed in Table 2.

---

[5] Time $t = 0$ is impact on the glass surface for bare targets, and impact on the copper buffer or cover plate for the other targets.

Table 3. Nomenclature Definition

Symbol	Definition
oc	measurement of off-centered impact; obtained from analysis of X-rays
d_{Cu}	diameter of Cu buffer
h	buffer thickness (height)
R_t	target resistance, see Eqn. (5), which is a measure of penetration resistance
Y_p	dynamic strength of projectile
u	penetration velocity
v_p	impact velocity
v_c	consumption velocity
v_F	failure front velocity
t_{Cu}	time to penetrate the Cu buffer or cover plate
t_{dwell}	time interval that rod dwelled on glass surface $= t_{pen} - t_{Cu}$
t_{pen}	time to begin penetration after impact
v_{hydro}	hydrodynamic penetration velocity, Eqn. (4)
ρ_t	target density
ρ_p	Projectile (rod) density

4.0 Analyses of Data

4.1 Consumption Velocity and Rod Deceleration

The consumption velocity, as measured here, is the time derivative of the length of the rod; with the rod length measured directly from the flash radiographs. The rod length is also given by the difference in the position of the tail, P_{tail}, and the position of the nose, P_{nose} ($\equiv P$, the projectile-target interface, i.e., depth of penetration). Therefore, the time rate of change of the projectile length is given by:

$$\dot{L} = \dot{P}_{nose} - \dot{P}_{tail} \equiv \mathrm{v}_c \approx u - \mathrm{v}_p \tag{5}$$

where the dot refers to the time derivative. In Eqn. (5), it has been assumed that the tail velocity can be replaced by (is equal to) the impact velocity (this assumption will be substantiated below). Thus, a check on the accuracy of the measurements is provided by the sum of u and v_c, which should be the impact velocity, i.e.:

$$u + |\mathrm{v}_c| = \mathrm{v}_p . \tag{6}$$

Of course, measurement uncertainties will result in the equality in Eqn. (6) being an approximation.

It was assumed that the tail velocity could be replaced by the impact velocity in Eqn. (5). This assumption ignores any deceleration of the rod during dwell and/or penetration.[6] For an eroding rod, the incremental decrease in the tail velocity due to elastic waves is given by [13]:

$$\Delta \mathrm{v}_{tail} = \frac{2Y_p}{c_L \rho_p} \tag{7}$$

where Y_p is the dynamic flow stress of the rod and c_L is the longitudinal sound speed in the rod. For the gold rod, Y_p is 20 MPa,[7] and c_L is 2.03 km/s [14], giving 1.02 m/s for the deceleration of the tail. For an 800-m/s impact velocity, this is only a 0.12% change in the tail velocity, and even less at the higher impact velocities. For a 70-mm-long Au rod, it takes ~34.5 µs for the first decelerating stress pulse to reach the back of the rod, and the time interval of the experiments is typically less than 100 µs. Thus, it is only near the very end of erosion, where the rod length is quite small, that the effects of deceleration could be measured in the experiments. Numerical simulations confirm the above assumptions. The rod velocity changed by only ~3 m/s with 65 mm of the rod eroded at an impact velocity of 800 m/s (3 elastic transits); and approximately 4 m/s for 60 mm of eroded rod at an impact velocity of 450 m/s.

4.2 Dwell on Bare Glass Targets

There were four experiments against bare borosilicate glass targets. Two of these experiments, Fig. 8, showed a very long dwell phase. The times in Fig. 8 are for the last X-ray

---

[6] Technically, since these are reverse ballistic experiments, the rod is not decelerating; rather, there is an acceleration of the rod due to the impact, but the conclusions remain unchanged; therefore, we will often discuss the tests as if the rod is moving.

[7] The initial flow stress is 20 MPa; because of strain hardening, the ultimate strength is 220 MPa, as reported in Section 2.2 and Ref. [14]. There is no strain rate effect reported for Au [14].

images taken during the experiments. During dwell, the rod is deflected (flows radially) at the glass surface and debris shows some characteristic chippings similar to when metal is processed in a lathe. Also, the first few millimeters of the glass (~7 mm), see Fig. 9, show a failed region inside the glass; otherwise, the glass remains intact. This damage may be a circumferential cone crack near the periphery of the glass, which is clearly observed in some experiments (as will be shown later). The consumption velocity, determined from the rod length versus time, was found to be 384±2 m/s, matching the impact velocity of 386±1 m/s; that is, $v_c = v_p$, as expected.
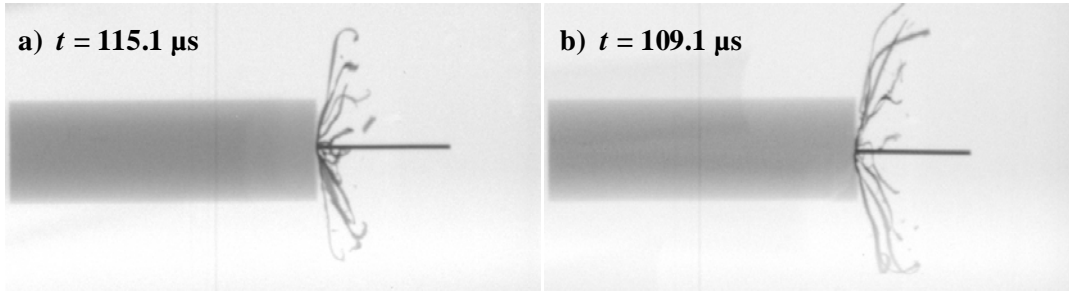
Figure 8. X-ray images for: a) Exp. 11107, v_p = 386 m/s and b) Exp 11108, v_P = 441 m/s; times after impact.
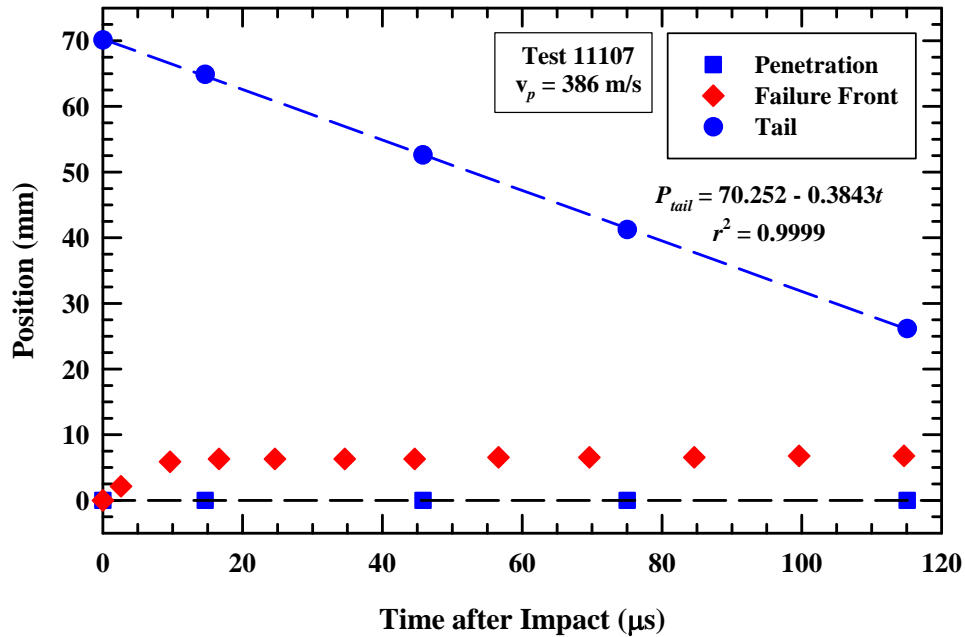
Figure 9. Position-time data for Exp. 11107, bare target, v_p = 386 m/s.

The position-time results for the impact at 441 m/s, Fig. 8(b), are plotted in Fig. 10. The consumption velocity is again equal to the impact velocity; although between 80 and 100 µs, the position of the failure front moves (perhaps an indication of some damage accumulating within the glass). However, there is no penetration at the time of the last X-ray (109 µs).

At only a slightly higher impact velocity of 463 m/s, there is a dwell phase that transitions to penetration, as shown in Fig. 11(a). At v_p = 475 m/s, penetration begins very early after impact, Fig. 11(b). The position-time data for Exp. 11110, Fig. 11(a), are plotted in Fig. 12. Only about 9 mm of the rod is defeated at the interface before the onset of penetration. The consumption
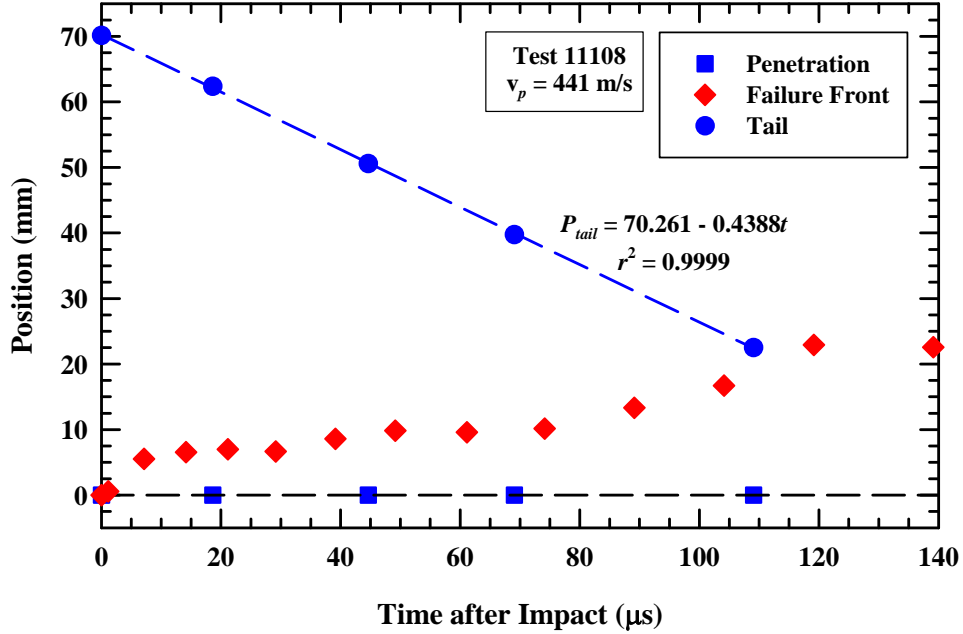
Figure 10. Position-time data for Exp. 11108, bare target, v_p = 441 m/s.
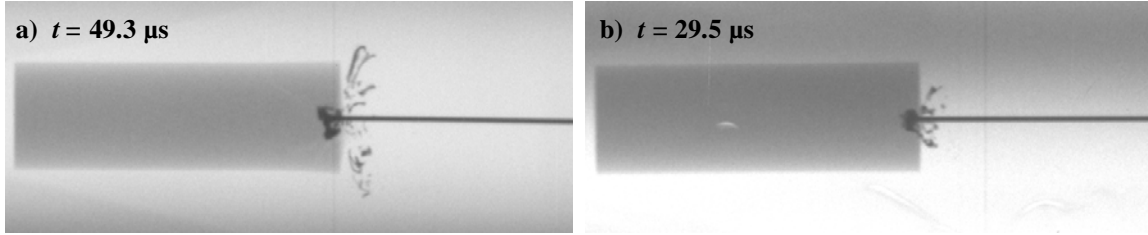
**Figure 11. X-ray images for: a) Exp. 11110, v_P = 463 m/s and
b) Exp 11109, v_P = 475 m/s; times after impact.**

velocity determined from the first two data points is 392 m/s, which is less than the impact velocity. This indicates that during the first ~24 µs, some penetration has occurred. We believe that the projectile dwelled for a period of time, and then began to penetrate. The average penetration velocity over the first 24 µs is 71 m/s ($u \sim v_p - v_c$). If we assume that the 1.9 mm of penetration at 24 µs occurred at approximately the same penetration velocity as given by the regression fit (167 m/s), then penetration began at approximately 11 µs earlier, or about 13 µs after impact. The average penetration velocity would then be:

$$\bar{u} = \frac{0*13 + 0.167*11}{24} = 76 \, \text{m/s} \tag{8}$$

which is very close to the 71 m/s calculated from $v_p - v_c$. This gives confidence in our interpretation that there is dwell before penetration in this experiment.

After transition, the penetration and consumption velocities were determined from linear regression of the nose position-time and length-time data, 167 m/s and 283 m/s, respectively. The sum of the penetration and consumption velocities should be the impact velocity (assuming no deceleration of the rod, as was discussed in Section 4.1). For this experiments, $u + v_c$ =

Figure 12. Position-time data for Exp. 11110, bare target, v_p = 463 m/s.

450±9 m/s, while v_p = 463±2 m/s, using the standard errors from the regression fits to estimate the uncertainties.[8]

Thus, the post-transition data appear to be reasonably consistent. The estimates of the dwell phase durations as a function of impact velocity a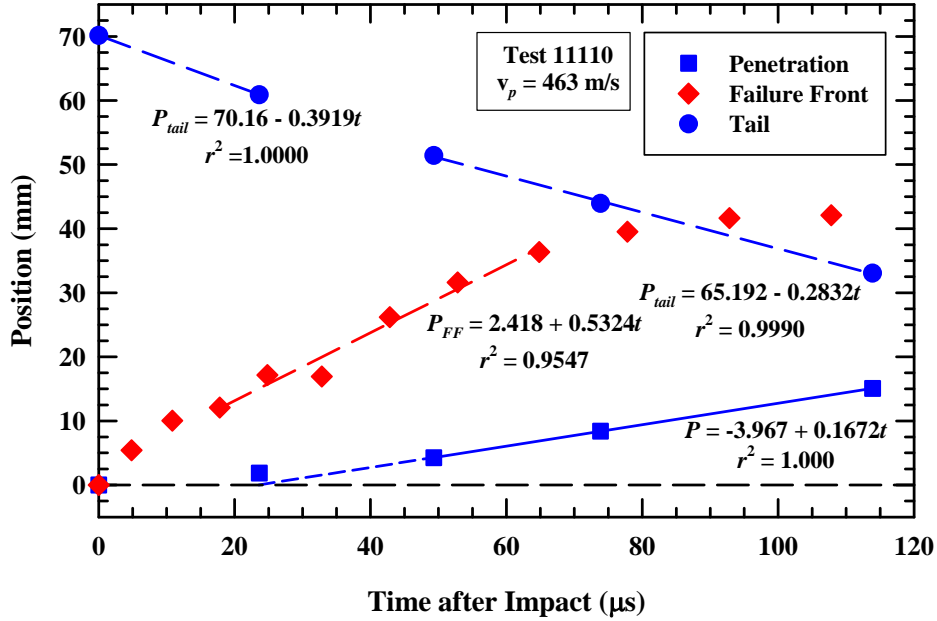re plotted in Fig. 13 for these bare glass targets. The short dashed line represents the time for the 70-mm rod to erode completely at the glass surface. Two of the data points are plotted at the time of the last X-ray images (Fig. 8), with an arrow denoting how much additional time would be required for complete rod erosion, assuming no penetration. The current experiments are shown with open circles, and two earlier experiments [4] are shown as the open diamonds. The experiment with an impact velocity of 412 m/s dwelled for approximately 25 µs before the onset of penetration, but this experiment had the highest yaw (4.2º) of any of the experiments. Whether the low dwell time associated with this experiment is due to inherent scatter in the dwell-transition velocity or due to the relatively large yaw is unknown.

Regardless, as the impact velocity increased from 441 m/s to ~460 m/s, dwell time decreased from over 100 µs to ~20 µs; and then dwell time decreased to ~7 µs at 475 m/s. Thus, it appears that ~450 m/s, denoted by the vertical dashed line, represents a reasonable estimate for the dwell-penetration transition velocity for bare borosilicate glass impacted by an Au rod.

4.3 Results of Additional Analyses of Experimental Data

Prior to proceeding with a discussion of the buffered and cover plate experiments, estimates for the time to penetrate the Cu buffer (or plate), the time for the onset of penetration, total dwell time, and length of remaining rod at the dwell-penetration transition are summarized in Table 4. The procedures for estimating these times are described in Section 3.2. Some of the columns of Table 2 are repeated in Table 4 to aid in evaluation of the experimental results.

---

[8] The uncertainty of the sum of u and v_c is the square root of the sum of the squares of the standard errors.
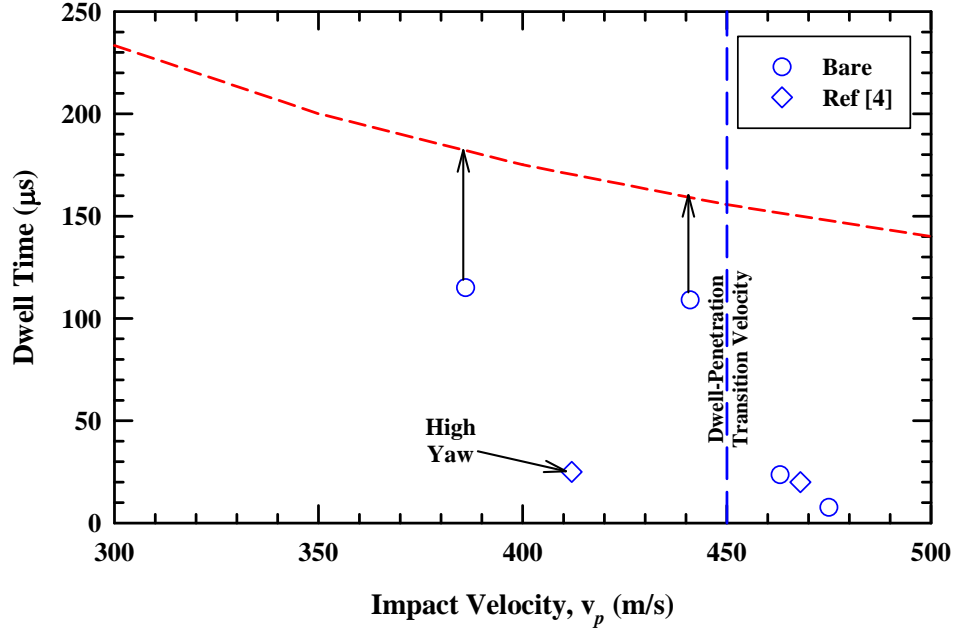
**Figure 13. Estimate dwell time vs. impact velocity for bare borosilicate glass.**

Table 4. Further Analyses of Experimental Data

Exp.	oc [mm]	d_{Cu} [mm]	h [mm]	v_p [m/s]	Target Response	t_{Cu} [µs]	t_{pen} [µs]	t_{dwell} [µs]
11107	1.5	-	-	386±1	sust. dwell	-	-	115+
11108	0.4	-	-	441±1	sust. dwell	-	-	109+
11110	0.4	-	-	463±2	transition	-	23.5	23.5
11109	0.4	-	-	475±3	penetration	-	7.6	7.6
10850	1.9	4	2.60	583±1	sust. dwell	7.5	-	91+
10853	1.0	4	2.60	649±5	sust. dwell	6.7	-	103+
10854	0.6	4	2.53	720±1	sust. dwell	5.9	100	94
10858	0.8	5	2.64	782±3	sust. dwell	5.7	-	89+
11111	0.0	5	2.54	800±2	sust. dwell	5.3	66.8	61
10862	1.7	5	2.54	890±5	sust. dwell	4.8	-	78+
10852	1.9	4	2.54	616±2	transition	6.9	89.6	83
10856	1.6	4	2.54	770±3	transition	5.5	58.5	53
10861	2.0	5	2.60	816±5	transition	5.4	49.2	44
10860	1.1	5	2.56	821±3	transition	5.2	37.9	33
10859	0.8	5	2.57	837±4	transition	5.2	29.5	24
11112	1.2	4	2.55	869	transition	4.9	23.8	19
10863*	0.5	4	2.58	882±4	transition	4.9	60.9	56
10851	2.0	4	2.60	611±2	penetration	7.1	7.2	0
10857	1.6	4	2.60	784±5	penetration	5.6	6.0	0
10855	1.8	4	2.60	794±7	penetration	5.5	6.4	1
11114	1.5	5	2.60	902±3	penetration	4.8	10.2	5
11116	0.2	20	2.53	856±2	transition	5.0	45.8	41
11113	0.8	20	2.63	889±3	transition	5.0	43.1	38
11115	0.8	20	2.56	912±1	penetration	4.7	7.6	3

4.4 Cover Plate Experiments

The cover plate experiments will be examined first since the results are not as dependent on hit location as for the buffer. A Cu cover plate, nominally the same thickness as the buffer, was used for three of the experiments. The primary advantage of the cover plate is that it is not hit-location sensitive. A disadvantage is that the cover plate will tend to impede radially flow of the rod if it is dwelling, which might affect the dwell-penetration transition velocity.

The flash X-ray heads are at the same location relative to the rod, but rotated at different angles around the shot line (see Fig. 2). Thus, the geometry (location) of the flash X-ray heads permit a reasonable estimate of the impact point of the rod relative to the centerline of the glass target.[9] The impact locations for the bare impact and cover plate experiments are shown in Fig. 14. The circles represent the full diameter of the rod (1.0 mm), and the larger outer circle represents the outer perimeter of the glass target. For these experiments, all the impacts were relatively near the centerline of the glass target.
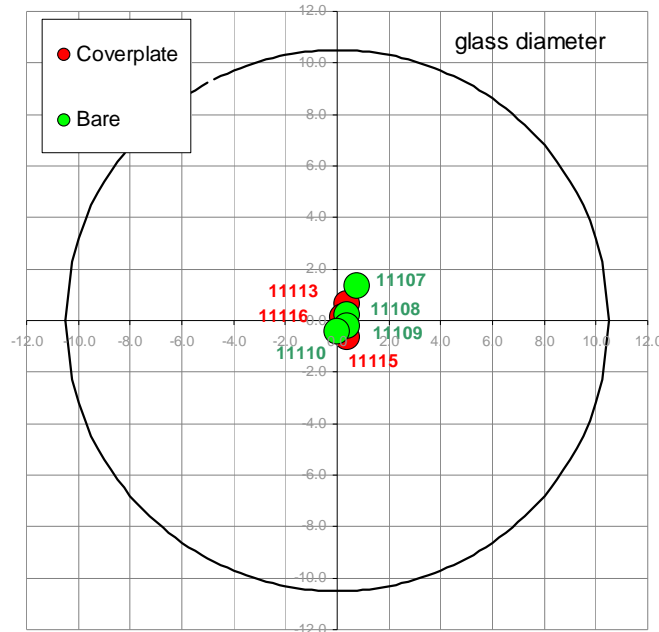
Figure 14. Estimated impact locations for the bare and cover plate experiments.

The flash radiographs for Exp. 11113, Fig. 15, show dwell for at least the first 33 μs after impact on the cover plate; the rod has begun to penetrate by 52.8 μs. The graph of the position-time data for this experiment is shown in Fig. 16. Extrapolation of the penetration-time response after the dwell-penetration transition gives 43.1 μs for the onset of penetration. Since it is estimated that it took 5.0 μs for the rod to penetrate the cover plate and reach the glass surface, the estimated dwell time for this experiment is 38 μs.

During dwell, the two-point estimate for the consumption velocity is 887 m/s, in excellent agreement with the impact velocity of 889±3 m/s (the initial, time-zero point cannot be included

---

[9] It is estimated that the accuracy of the impact locations is good to ±0.5 mm, that is, one-half rod diameter.
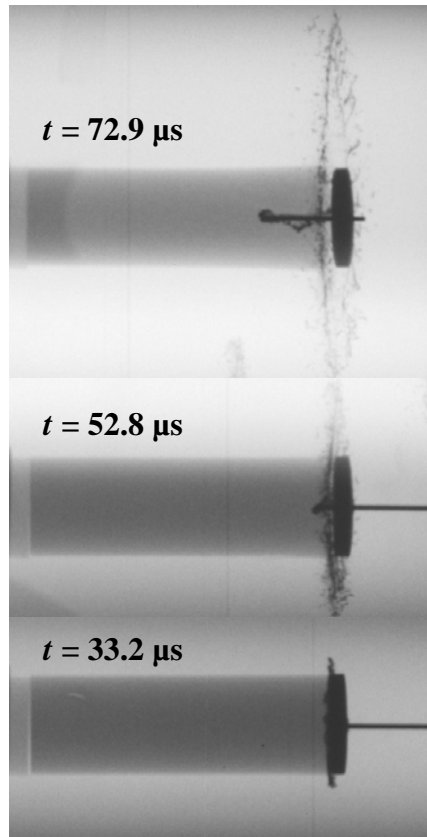
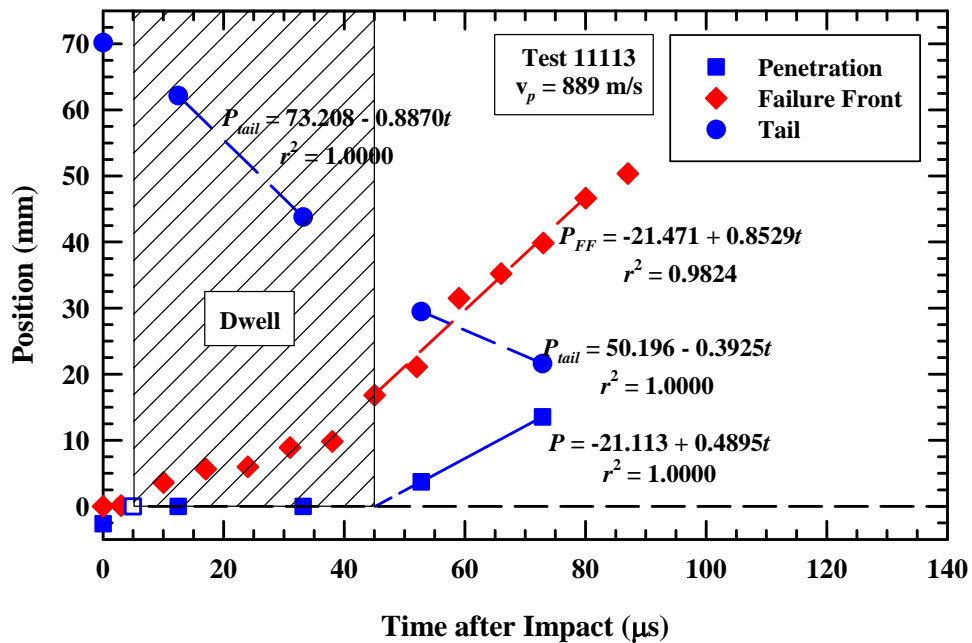**Figure 15. Flash radiographs for Exp 11113, v_p = 889 m/s; times after impact.**

Figure 16. Position-time data for Exp. 11113, an experiment with a Cu cover plate, showing transition from dwell to penetration.

in the regression analysis because the rod erodes as it penetrates the Cu plate). After the dwell-penetration transition, $u + v_c$ is 882 m/s, again in good agreement with the impact velocity.[10] These differences of less than 1% are within the accuracy of the position measurements from the X-ray film. These analyses provide very good confidence in the accuracy of the experimental data.

The X-ray images appear to show an axial component in the expansion of the deflected gold rod, for example, see Fig. A-43 in the Appendix. However, this is due to "optical" distortion as these images are taken outside the focal plane of the X-ray. The optical pictures show that the deflection produces a nearly perfect radial expansion, as shown in Fig. A-44. Only for the lowest impact velocities—for the bare glass targets—is there a relevant axial component present as the rod is redirected, similar to swarfs during machining.

It is seen that the radial flow of the rod while it was dwelling on the glass surface resulted in separating the cover plate from the glass surface, Fig. 15. The cover plate also separated from the glass in Exp. 11116, which was at a slightly lower impact velocity (v_p = 856 m/s), and which dwelled for about the same time as Exp. 11113. However, for Exp. 11115, which impacted at a slightly higher impact velocity (v_p = 912 m/s), the dwell phase was estimated to be less than 3 µs, and the cover plate appears to have remained attached to the glass surface during the timeframe of the experiment. The separation of the cover plate for sustained dwell in these glass experiments is in contrast to the experiments with silicon carbide, where the cover plate remained attached during sustained dwell [15].

4.5 Dwell on Buffered Glass Targets

4.5.1 Impact Locations

Analysis of the buffered targets is somewhat more difficult because the rod had a glancing impact on some of the buffers. The dwell time depended on the impact velocity as well as where the rod impacted. The estimate for the impact locations for the 4-mm-diameter buffers are shown in Fig. 17. This figure is similar to Fig. 14 except that the diameter of the Cu buffer is also shown. It is estimate that for at least 4 of the experiments, the rod only contacted a portion of the buffer. This is in contrast to the experiments with a 5-mm-diameter Cu buffer, Fig. 18, where it appears that all the rod impacts were within the buffer diameter.
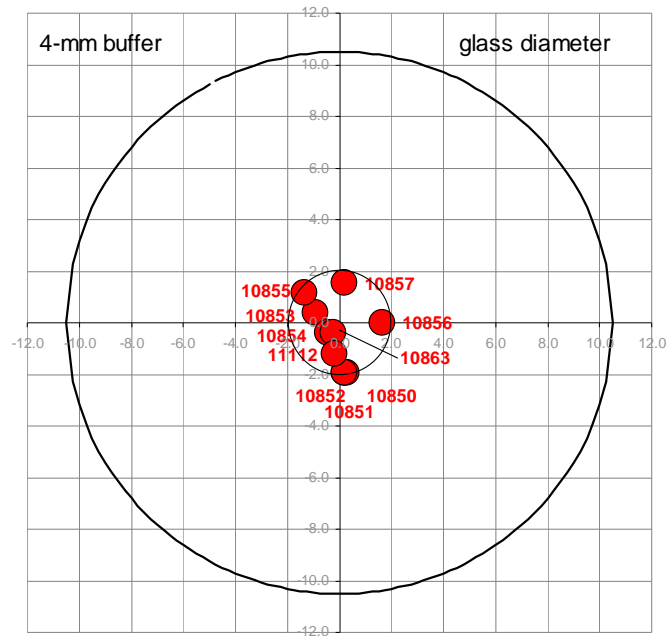
4.5.2 Sustained Dwell

A long period of sustained dwell is shown in Fig 19, for Exp. 10862, at an impact velocity of 890 m/s, which is the highest impact velocity showing sustained dwell. The definition of sustained dwell adopted for this study is little-to-no movement of the damage front after the initial 7-10 mm that is observed in all experiments having more than ~20 µs of dwell.[11] Experiment 10862 is representative of all the experiments in the "sustained dwell" category. The failure front—the diamonds in Fig. 19—does not move after the initial jump of ~10 mm. X-ray and camera images at nominally 23, 60, and 80 µs are shown for this experiment in Fig. 20. The

---

[10] Two-point linear fits to the experimental data do not provide any measure for a standard error.

[11] The damage front did not move, after initial formation, in Exp. 10862, even though there is a small amount of penetration at the latest times. Experiment 11108, Fig. 10, represents one of the few cases where there is movement of the damage front, with little to no penetration, but this movement of the damage front is very slow. As there was no penetration, Exp 11108 was still identified as sustained dwell.

Figure 17. Estimated impact locations for experiments with a 4-mm-diameter Cu buffer.
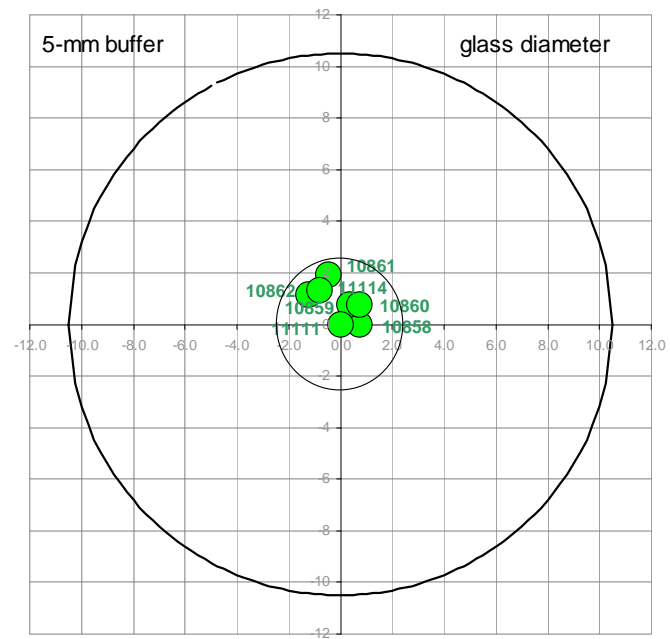
Figure 18. Estimated impact locations for experiments with a 5-mm-diameter Cu buffer.

Figure 19. Example of Cu buffer experiment showing sustained dwell.

**Figure 20. X-ray images (left) and camera pictures (right)
for Exp. 10862 (v_p = 890 m/s); times after impact.**

rod is fully consumed in the last image. The measured consumption velocity is 868 m/s, whereas the impact velocity is 890 m/s. The length-time measurements of the rod are quite accurate. If, i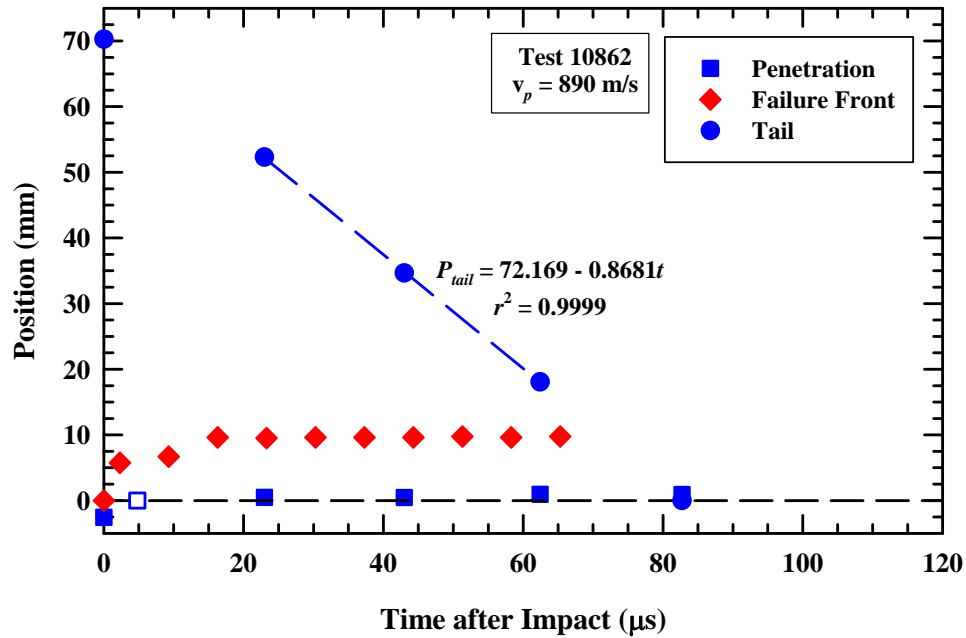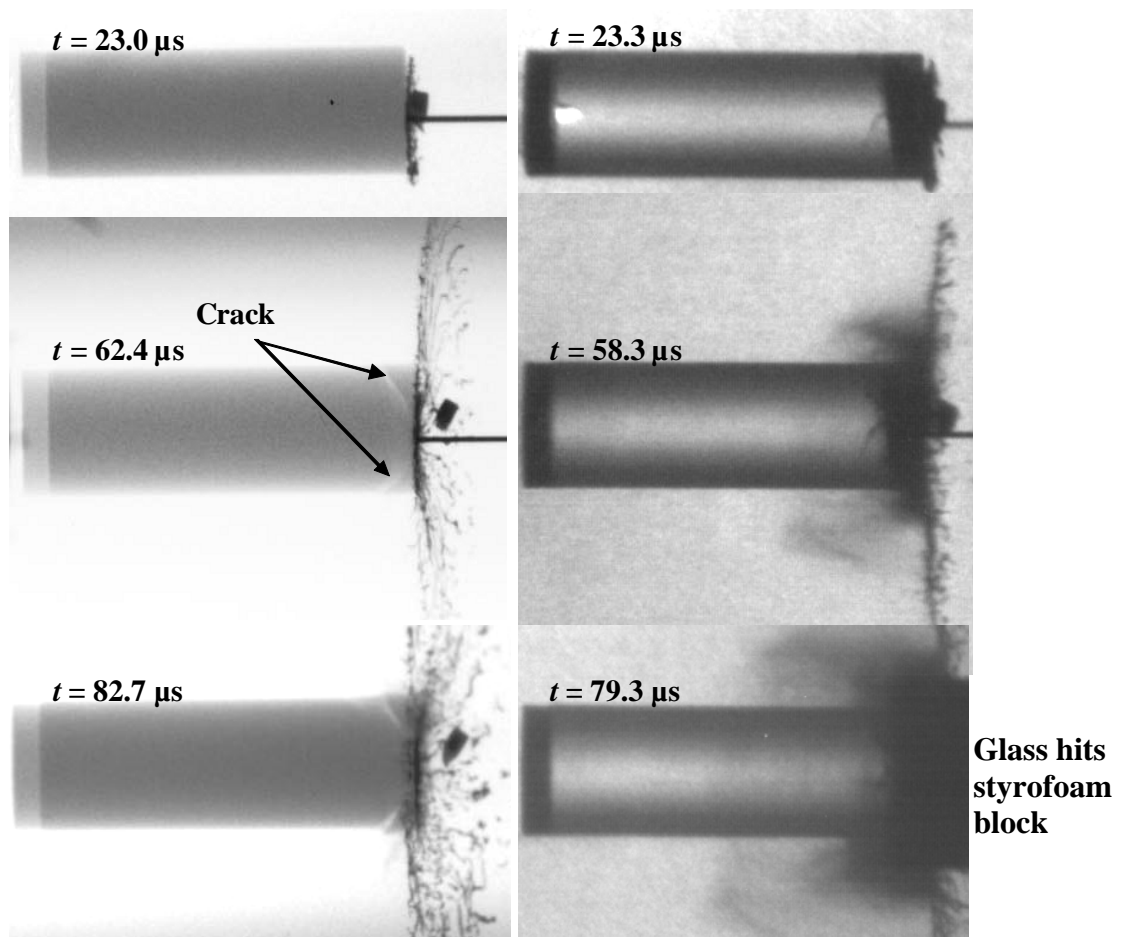nstead, we assume that the difference in the consumption velocity and the impact velocity is a penetration velocity, then the data in Fig. 19 suggests that there is a penetration velocity of approximately 22 m/s. Assuming this penetration velocity, there would only be 0.9 mm of penetration over a time period of 40 µs; 0.9 mm of penetration is the estimated penetration at 62 µs and 83 µs from the flash radiographs (admittedly, difficult measurements).

All the "sustained dwell" experiments show similar discrepancies between the rod consumption rate during dwell and the impact velocity. At first, we were inclined to accept the differences in v_c and v_p as "measurement error/uncertainty." However, such discrepancies are not present in many of the experiments conducted, e.g., see Figs. 10, 12, and 16. Additionally, measuring the very small penetration depths corresponding to a very, very small penetration velocity (on the order of a few 10's of m/s) within measurement uncertainties is virtually impossible over the timeframe of the experiment. Several of the sustained dwell experiments show a small amount of penetration, of a millimeter or so, from which a calculation of a penetration velocity is fraught with errors and uncertainties.

However, as already stated, rod length measurements have been shown to be quite accurate. Therefore, we now attribute the differences between v_p and v_c for sustained dwell experiments as due to a very small and virtually immeasurable penetration velocity that is inferred indirectly from the difference between the impact velocity and the consumption velocity.[12]

This very low penetration velocity distinguishes dwell like behavior from more traditional penetration, such as shown in Fig. 4 and Fig. 16, where there is an abrupt change in penetration velocity. For dwell, the state of the material resists penetration, although there might be some very slow erosion-like phenomenon at the target surface. This is in contrast to penetration where a distinct penetration channel is formed as the rod penetrates into the target.

An interesting observation for dwell is that there is only a small failed region of the glass (about ½ a target diameter, optical pictures) near the impact surface while most of the glass length stays intact for the rest of the dwell process. This effect seems analogous to that described in Ref. [16] for a much different projectile and target combination. Some of the X-ray images for the buffered glass reveal a circular, symmetric crack in the glass, as shown in the late-time X-ray of Fig. 20 at 62.4 µs, and even more clearly at 82.7 µs. This damage region is coincident with the dark region in the camera images. Thus, the initial failure front for many of the experiments, and in particular for the experiments that showed sustained dwell, is most likely the result of this conical (torus) damage ring.[13] This crack evidently occurs quite early during the interaction, but clearly, the glass sustains dwell. Furthermore, it seems that the crack development is induced at the edge of the buffer which transmits effects of projectile loading into the glass via its surface. However, the tests with bare glass and the tests with a cover plate show no signs of crack development, but still the small failed region is visible in the optical images. So, it is very likely that conical, circumferential crack results from impact loading, but it is hard to imagine that the glass underneath the projectile has failed.

---

[12] If a rod other than gold, i.e., a rod that had sufficient strength that deceleration—acceleration in the case of the reverse ballistic experiment—could not be neglected, a penetration velocity would be much more difficult to estimate.

[13] Further observations of this phenomenon will be discussed in Section 4.9.

4.5.3 Transition from Dwell to Penetration

An example of an experiment with a dwell-to-penetration transition is shown in Fig. 21, which is one of the experiments with a 5-mm diameter Cu buffer. The rod begins to penetration at 49.2 µs, and penetrates at a velocity of 426 m/s. The sum of the penetration and rod consumption velocities is 796±17, which agrees reasonably well with 816±3 for the impact velocity. The onset of penetration triggers propagation of the failure front. The failure front position looks similar to that of Fig. 19 for the first 50 µs, after which the failure front begins to propagate at an average velocity of 884 m/s.
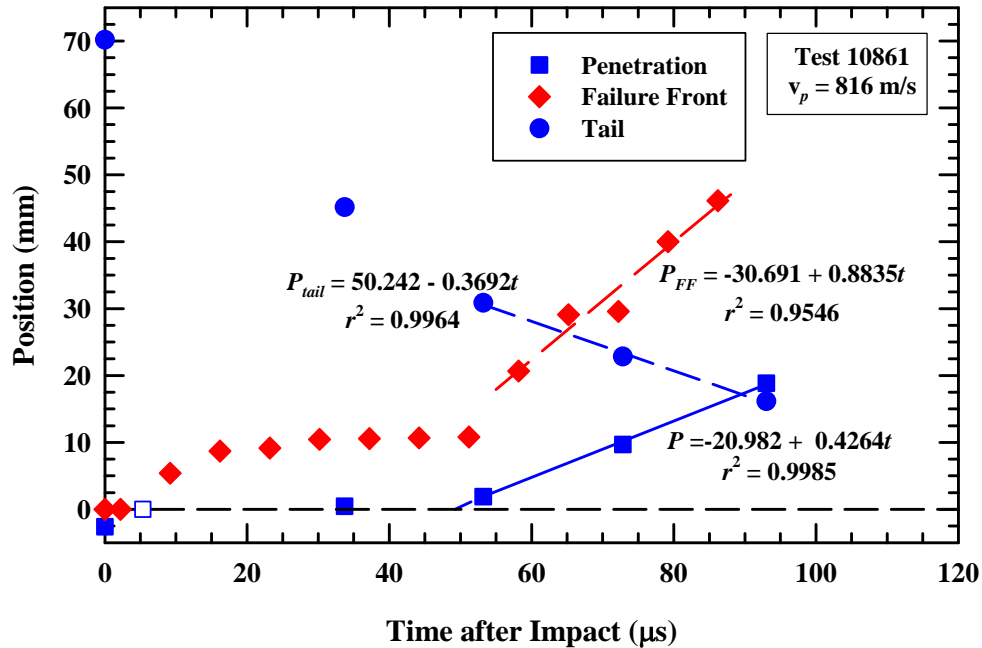

Figure 21. Example of dwell to penetration transition.

4.5.4 Penetration

There were five experiments with Cu buffers that had estimated dwell times less than 5 µs (including one of the cover plate experiments). Two experiments, Exps. 11114 and 11115, had impact velocities over 900 m/s. But the other three experiments had impact velocities less than 800 m/s, and in particular, were experiments that had edge hits on the buffer, Fig. 17. Although it appears that Exp. 10851 and 10855 hit the edge of the buffer from Fig. 17, the accuracy in estimating the hit location is one-half rod diameter. Examining the X-rays images in the Appendix combined with the experimental results supports an interpretation that the rod just grazed the buffer for these two experiments. Similar analysis of Exp. 10857 suggests that the rod did not make substantial contact with the buffer in this experiment.

If the rod impacts the glass at the velocities of these experiments, which are well above the dwell-penetration transition velocity for a bare target (Section 4.2), then the glass sees impact stresses associated with the shock, and penetration begins almost immediately. Figure 22 plots the position-time data for Exp. 10851, which had virtually no dwell phase.

The two high-velocity tests that had "good" impacts on the buffer show different behavior than the experiments that had a glancing blow on the buffer. Experiment 11114 is a buffer experiment with a center hit on the 5-mm buffer. The position-time data are plotted for

Exp. 11114 in Fig. 23 (and the high-velocity cover plate experiment, Exp. 11115, shows a very similar behavior); these data exhibit a short but finite dwell phase before transitioning to steady-state penetration.
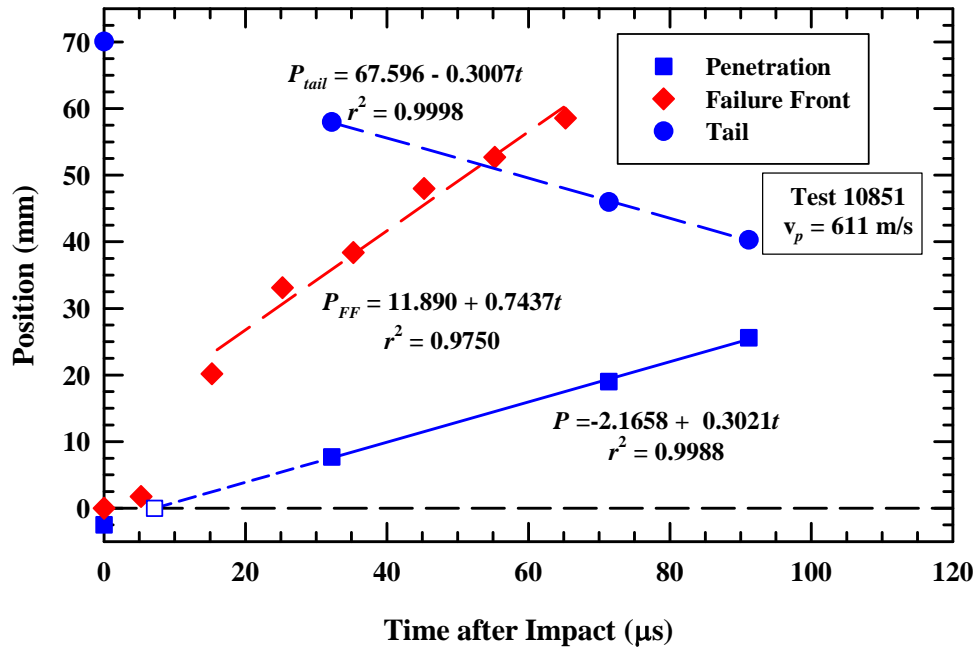

Figure 22. Example of almost immediate penetration for a case where the rod had a glancing impact on the Cu buffer.
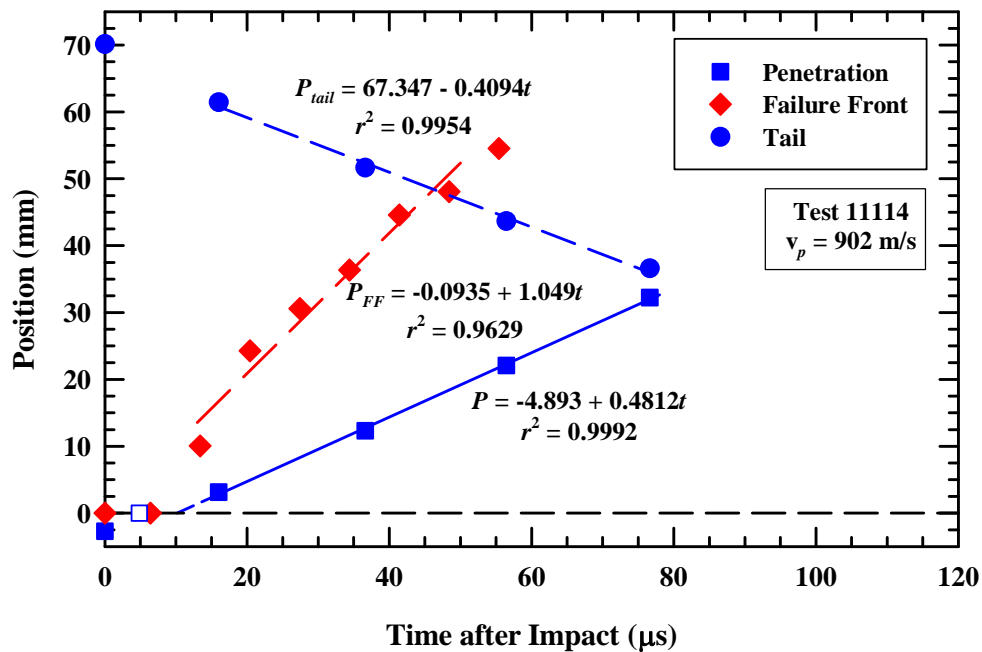

Figure 23. Example of penetration for an impact that is above the dwell-penetration transition velocity for borosilicate glass with a Cu buffer.
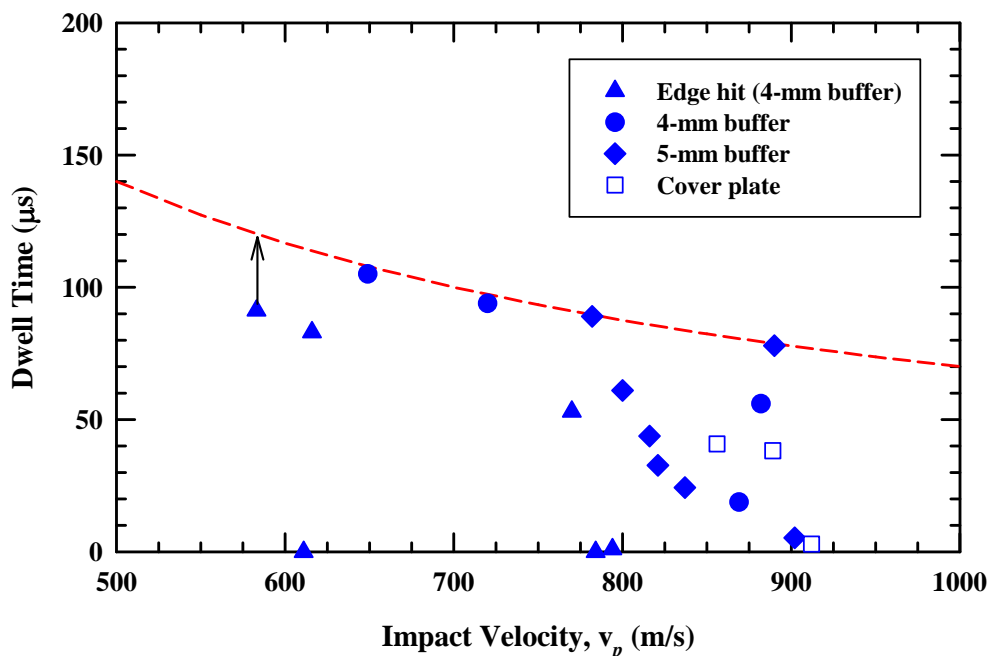
4.5.5 Cu Buffer

It is not necessary to hit the small Cu-cylinder in the center to achieve a stable dwell condition, but it has been shown that if the impact is too far off-center, the dwell-penetration transition time can be affected considerably (also discussed in the next section). It has also been observed, for many of the experiments, that the buffer separates quite early from the glass. This supports our interpretation that the buffer serves only to eliminate the impact shock on the glass (and possibly provide ramp loading, as discussed in Section 4.11).

For those experiments where transition was observed at relatively early times compared to other experiments at the same impact velocity, it seems that the Cu buffer was hit very near the edge (or missed the buffer completely). Thus, the impact shock was not fully dissipated, resulting in either prompt penetration or substantially less dwell time.

4.6 Estimates of Dwell Times and Dwell-Transition Velocity

The dwell times were estimated as described in Section 3.2, accounting for the time for the rod to penetrate the Cu buffer or cover plate. These times are given in Table 4, and plotted in Fig. 24 as a function of impact velocity. The short dashed line represents the time for the 70-mm rod to erode completely at the glass interface (ignoring the time it takes to penetrate the Cu buffer).

The solid triangles denote experiments that had a 4-mm-diameter buffer where the rod hit the edge of the buffer. It is observed that the higher the impact velocity, the more detrimental the effects of an edge hit on the buffer (presumably because the impact shock is not totally dissipated). Missing the buffer, or having essentially a glancing impact on the buffer, results in immediate penetration at an impact velocity of 611 m/s.

Figure 24. Estimated dwell times for borosilicate glass with Cu buffer or cover plate.

Sustained dwell is achieved consistently up to impact velocities of almost 800 m/s provided reasonably centered impacts on the buffer. Between 800 and 900 m/s, there is a period of dwell

that then transitions to penetration. Results with the 5-mm-diameter buffer (and one 4-mm-diameter buffer) show for cases of transition that the dwell time diminishes relatively monotonically with increasing impact velocity. An example of the transition from dwell to penetration is shown in Fig. 25. Although this experiment is for a cover plate experiment, it is representative of the other results.
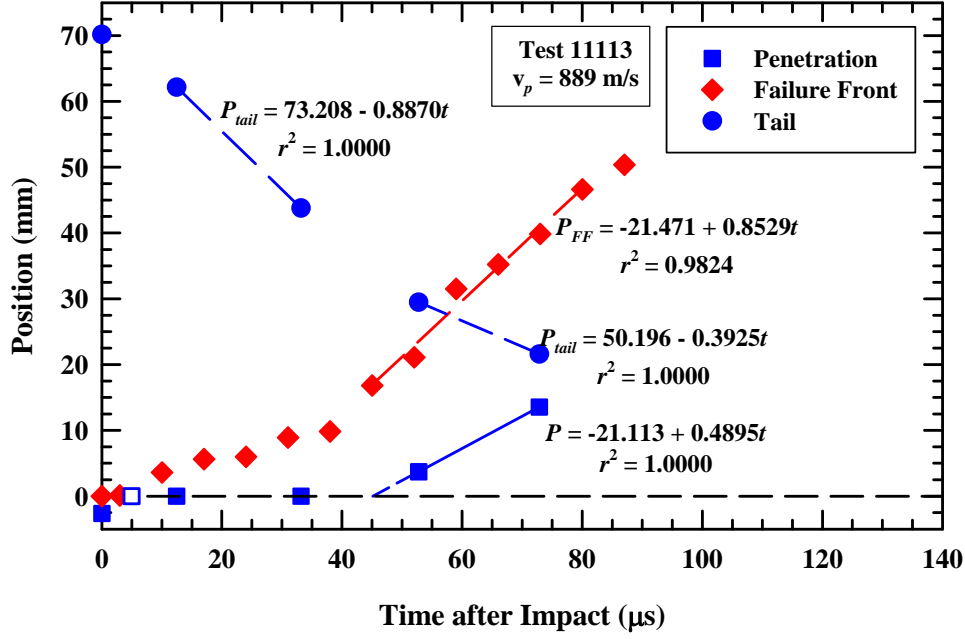
Figure 25. Example of dwell-to-penetration transition at relatively high impact velocity.

There are two data points at approximately 890 m/s where the monotonic decrease in dwell time is suddenly reversed, with one experiment having sustained dwell at 890 m/s. This reversal in dwell duration, we believe, is not due to small differences in impact location and/or impact yaw as there is no consistent correlation of dwell time with these variables. Further, the two cover plate experiments at impact velocities below 900 m/s have dwell times comparable to the other experiments between ~810 – 880 m/s. However, at impact velocities above 900 m/s, there is effectively no dwell, as represented by the data in Fig. 26.

We conclude that the scatter in dwell times between ~800 and 900 m/s is probably due to the inherent scatter in what is nominally an instability condition (the transition from dwell to penetration). Thus, we estimate the dwell-penetration transition velocity to be 850±50 m/s for borosilicate glass with a Cu buffer impacted by an Au rod. The use of the Cu buffer increased the dwell-penetration transition velocity by approximately 400 m/s as compared to a bare borosilicate glass target. We can also conclude that there is virtually no dwell phase, using a Cu buffer, for impact velocities above 896±6 m/s. These two ranges are denoted in Fig. 27 by the shaded rectangles. The stresses from the impact shock and the Bernoulli stresses associated with dwell for these impact velocities are discussed in Section 4.11.
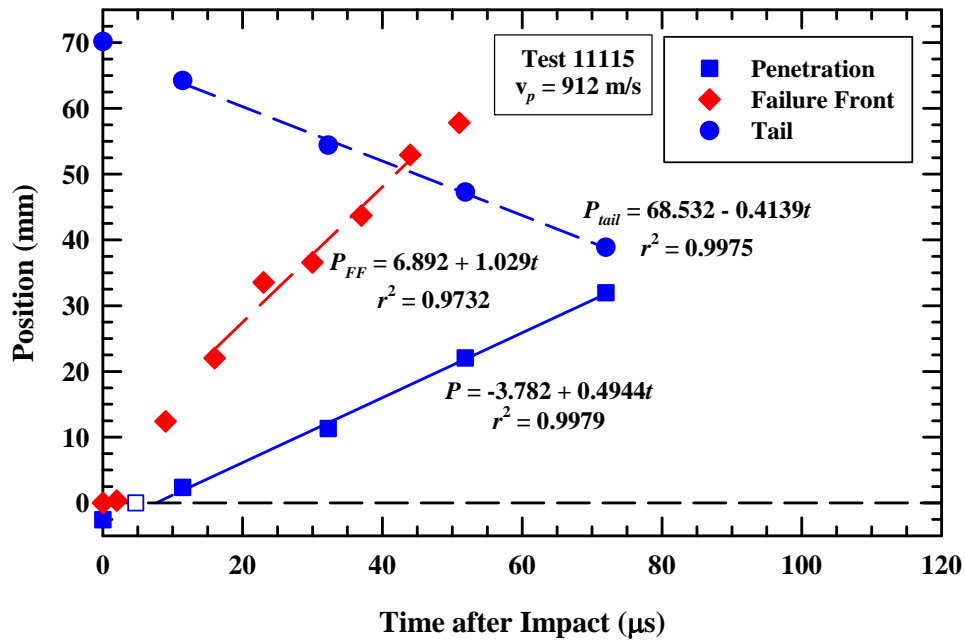
Figure 26. Example of impact where there is little to no dwell phase.
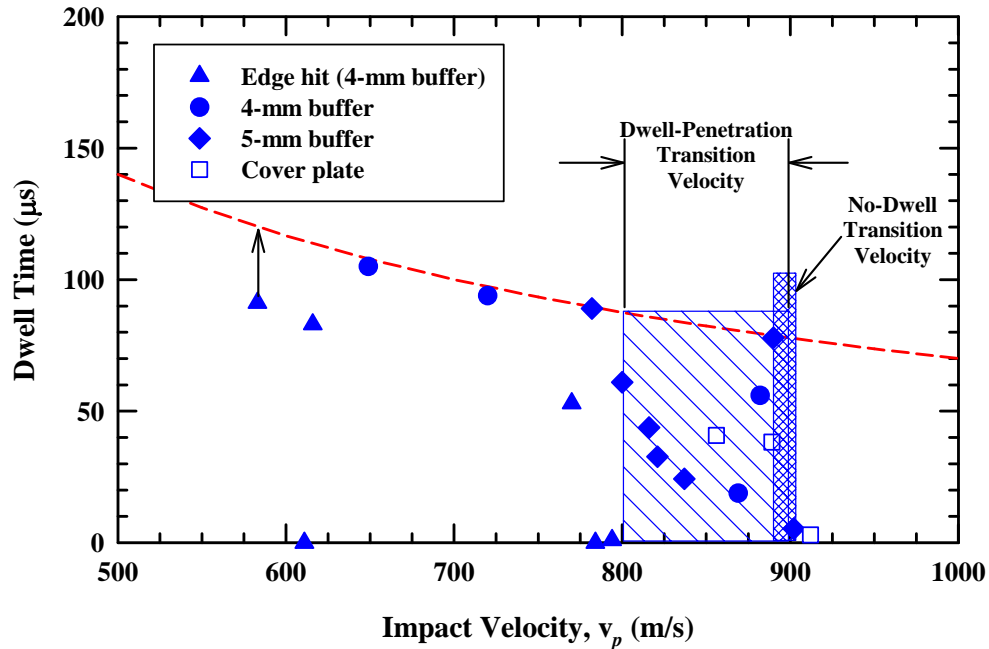
**Figure 27. Estimates for the dwell-penetration transition velocity and
no-dwell transition velocity using a Cu buffer.**

4.7 Assessment of Overall Accuracy of Experimental Measurements

One of the ways to evaluate the accuracy of the experimental measurements is to sum the penetration and consumption velocities determined for each experiment. The penetration velocity is determined from the depth of penetration versus time, while the consumption velocity is determined from the length of the projectile versus time. Thus, the penetration and

consumption velocities are independent measurements. The sum of $u + v_c$ should be identically equal to the impact velocity v_p (for the Au rod since it effectively does not decelerate during the timeframe of the experimental measurements, Section 4.1).

The first comparison is between the consumption velocity and v_p during dwell (when u is ostensibly identically equal to zero), shown as the open triangles in Fig. 28. Although there are a few experiments in which v_c appears to be identical to v_p, there are a number of experiments where v_c is less than v_p, indicating a small but finite, non-zero u. This was discussed in Section 4.5.2. As noted in that Section, penetrations of a millimeter or so were estimated for some of the experiments that had "sustained dwell."

The next comparison is between the post-transition $u + v_c$ with v_p (the values for u and v_c are from Table 2). The dashed line in Fig. 28 represents the condition where $u + v_c = v_p$. Generally, it is observed that the sum of the penetration and consumption velocities yields the impact velocity within the uncertainty of the measurements (recall, also, that v_p generally has an uncertainty of $\sim\pm3$ m/s, Table 2). This gives confidence in the experimentally determined values for the penetration and consumption velocities.
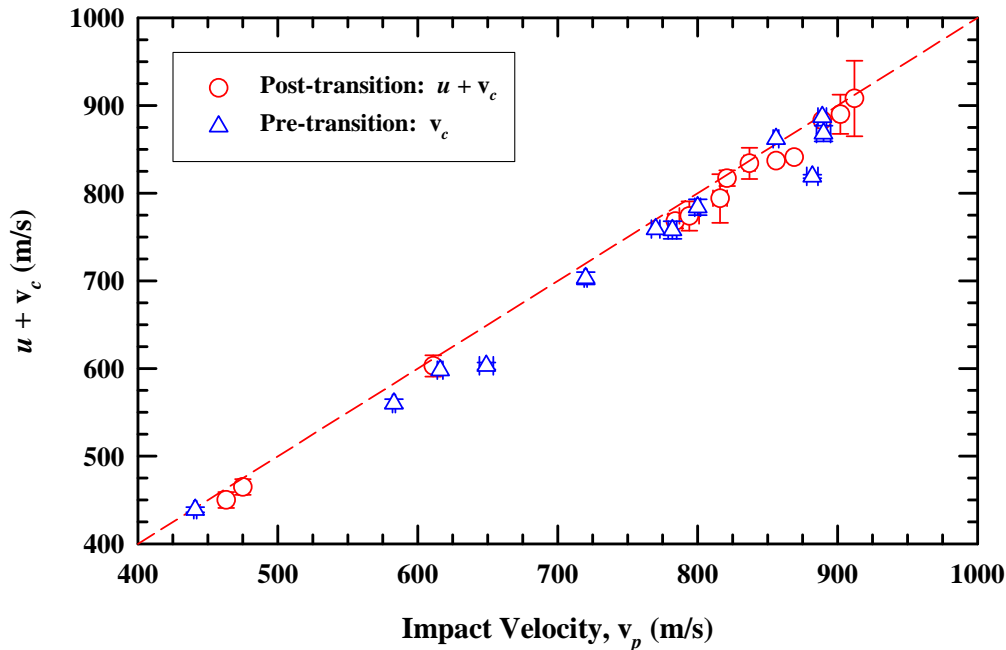

Figure 28. Accuracy assessment: comparison of $u + v_c$ with v_p.

4.8 Comparison of Post-Dwell and Prompt Penetration and Consumption Velocities with Previous Data

The penetration and consumption velocities were estimated from the flash X-ray data. These penetration and consumption velocities are listed in Table 2. The experimental results fall into nominally three categories: sustained dwell, dwell followed by penetration, and nominally prompt penetration (those experiments that had little-to-no dwell phase). The definitions of these various target responses are given in Section 3.3. Tables 2 and 4 denote the target response for each of the experiments.

The post-transition penetration velocities and the prompt penetration velocities are compared to previous data for penetration into borosilicate glass [8] in Fig. 29. The solid square
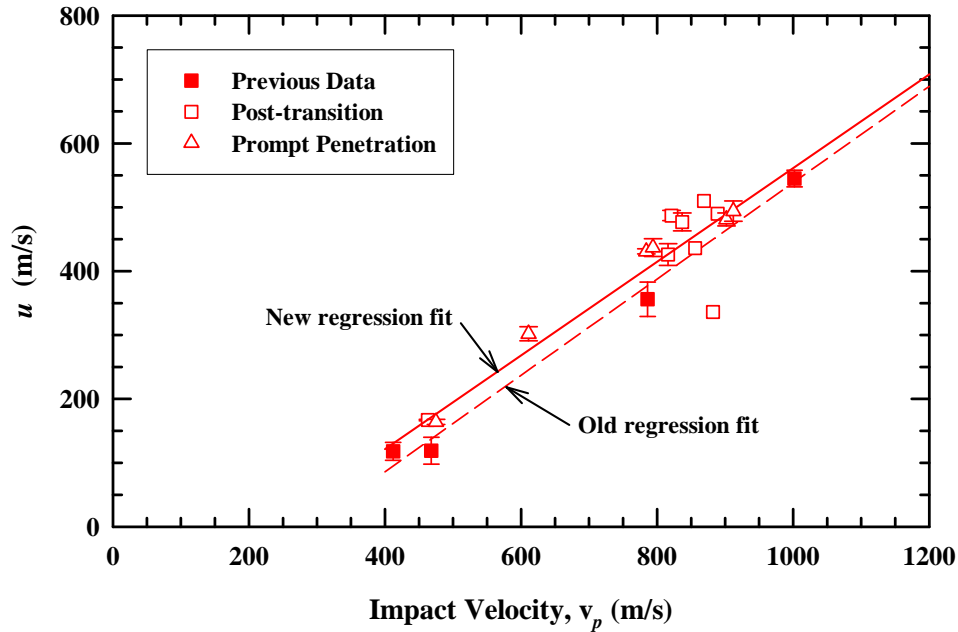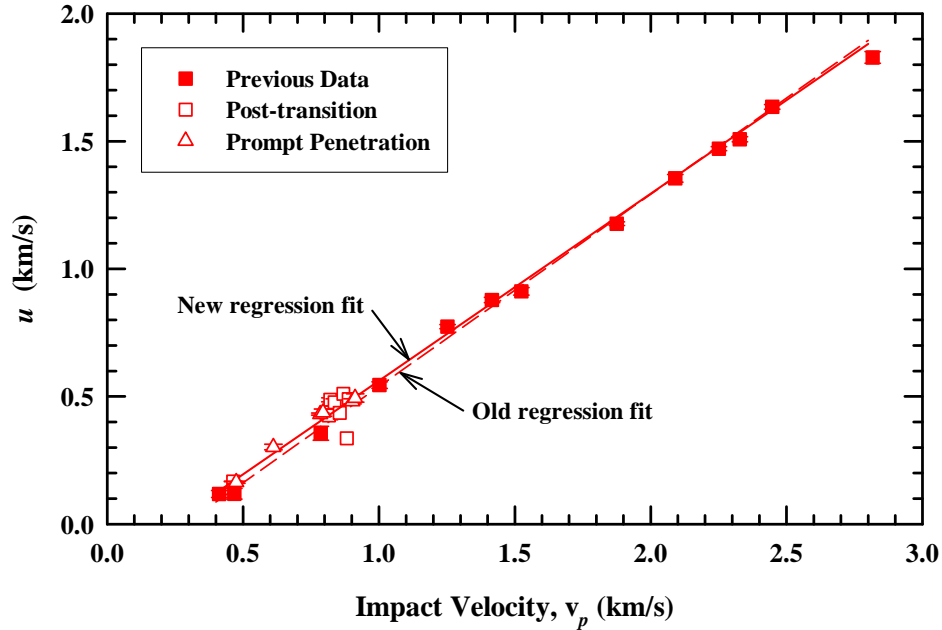
Figure 29. Comparison of post-transition and prompt penetration velocities with previous data [8].

symbols denote the results from the previous experiments; the open squares denote the post-transition penetration velocity, and the open triangles denote the prompt penetration velocities from the current study. The dashed line is the regression fit, Eqn. (1), obtained for the previous data.

There appears to be no discernable difference, as a function of impact velocity, in the prompt penetration velocities and the post-transition penetration velocities. However, the penetration velocities from the current experiments lie slightly above the regression line for the previous data. It is noted, though, that there are only four data points below 1000 m/s from the previous data. It was decided to conduct another regression fit of u versus v_p, including the new data (post-transition and prompt) with the previous data. The results are summarized in Table 5, and the new regression line is shown as the solid line in Fig. 29 (the very low u data point at $v_p =$ 882 m/s was not included in the regression analysis). The slope of the $u - v_p$ regression changed by 2.8%, and the effect is largely confined to impact velocities below 1000 m/s, as can be seen from Fig. 30 where all the data are plotted. The standard error of the new regression fit only increased by 2 m/s. We thus conclude that the new regression fit is as good a predictor of the penetration velocity as the old fit.

Table 5. Summary of Regression Analyses on Penetration and Consumption Velocities

	Regression Fit [km/s]	r^2	Standard Error [km/s]	Standard Error on Slope
Penetration Velocity				
Previous Fit	$u = 0.7539v_p - 0.2155$	0.9970	±0.028	±0.0110
New Fit	$u = 0.7330v_p - 0.1716$	0.9958	±0.030	±0.0092
Consumption Velocity				
Previous Fit	$v_c = 0.2493v_p + 0.2077$	0.9634	±0.033	±0.0130
New Fit	$v_c = 0.2718v_p + 0.1609$	0.9659	±0.033	±0.0100

Figure 30. Comparison of post-transition and prompt penetration velocities with previous data [8], all impact velocities.

A similar analysis was performed for the consumption velocity. Again, no difference, as a function of impact velocity, is apparent between the post-transition and the prompt consumption velocities. The results of a new regression analysis, including all these data from the current experiments with the previous experiments, are summarized in Table 5. The new regression fit is compared to the old fit in Fig. 31. The standard error for the new fit is the same as for the old fit, although the slope for $v_c – v_p$ changed by 9%. As with the penetration velocity, low-velocity predictions are the ones mostly affected by the new regression fit, as can be seen in Fig. 32.
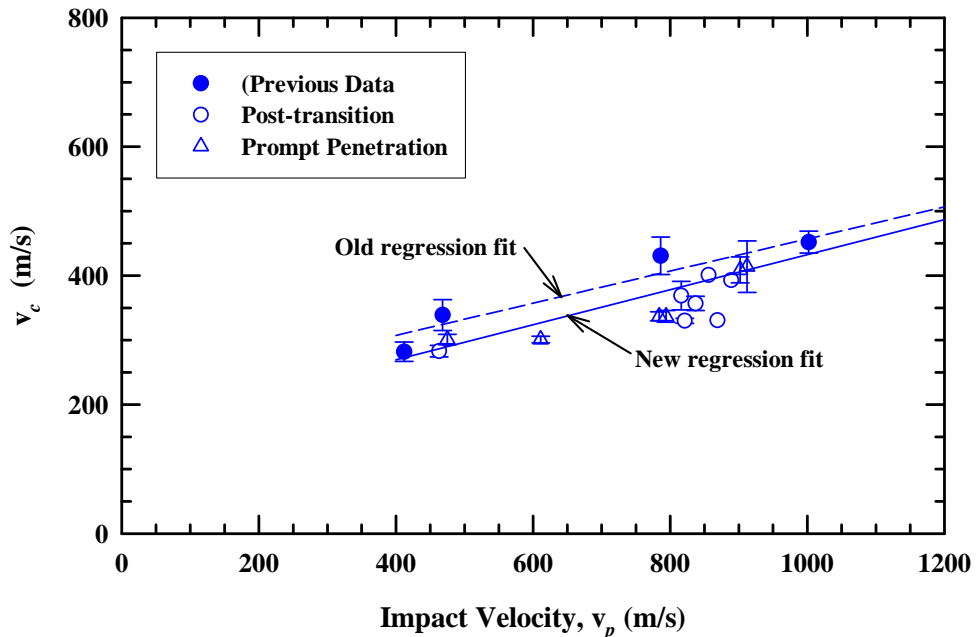
Figure 31. Comparison of post-transition and prompt consumption velocities with previous data [8].
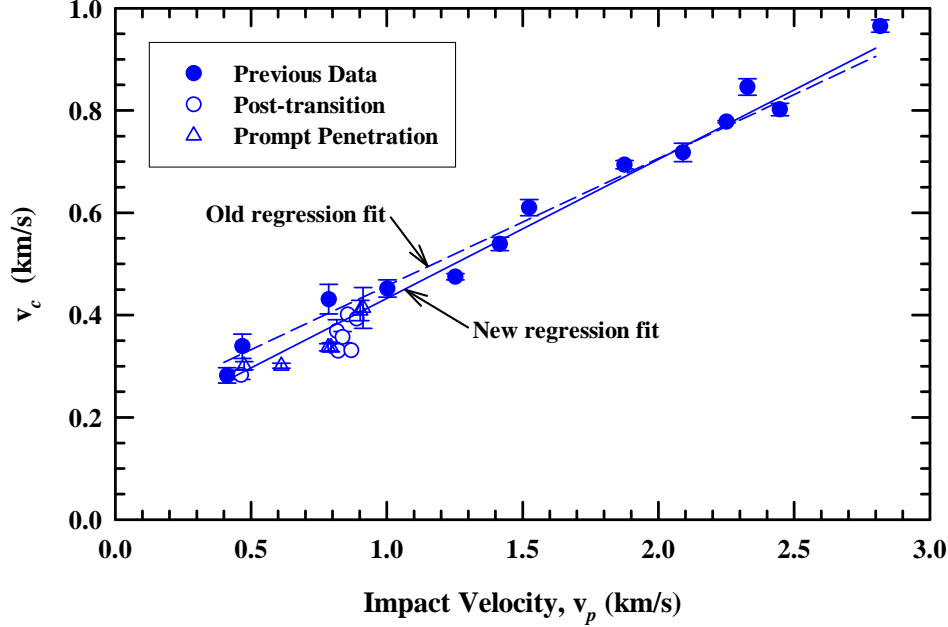
Figure 32. Comparison of post-transition and prompt consumption velocities with previous data [8], all impact velocities.

A check on accuracy of the regression fits can be done by comparing the sum of the penetration and consumption velocities—since the regression fits were determined independently of each other—with the impact velocity:

Old Fit $\qquad u + v_c = 1.0032v_p - 0.0078$ $\qquad\qquad$ (9)

New Fit $\qquad u + v_c = 1.0048v_p - 0.0107$ $\qquad\qquad$ (10)

The sum of u and v_c should be identically equal to the impact velocity, v_p. At 1.0 km/s, the old fit is accurate (in returning v_p) to 5 m/s, and the new fit is accurate to 6 m/s.

However, examining Figs. 29 – 32, there appears to be somewhat more scatter in the new data than the previous data. This increased scatter as a function of v_p could be for several reasons: 1) in most cases, there were a limited number of flash X-ray data points available to determine u and v_c (and in many cases, only two points); 2) only for the new set of experiments do we have many "repeat" tests that might indicate a natural scatter in results; 3) incipient damage could be generated in the glass during dwell, thereby making it slightly easier to penetrate after transition (higher penetration velocity and lower consumption velocity). The scatter could be a combination of all three possibilities, but we believe that the second reason is the most likely source of the larger scatter, since we showed that, even with very few position-time points, that $u + v_c \approx v_p$.

4.9 Comparison of Post-Dwell Failure Front Velocities with Previous Data

The post-transition failure front (FF) velocities, v_F, are compared to the FF velocities from Ref. [8] in Fig. 33. The previous data are represented by the solid triangles. The prompt penetration FF velocities are denoted by the inverted triangles, and the open upright triangles denote the FF velocities associated with post-transition penetration.
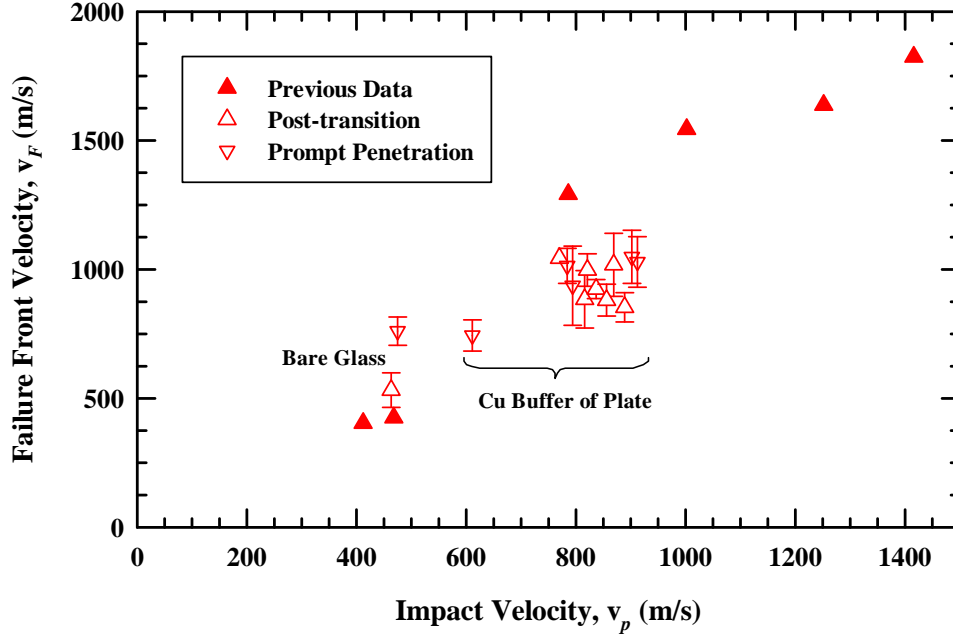
**Figure 33. Comparison of post-transition and prompt failure front velocities
with previous data [8].**

Although the FF velocity for the two or three lowest impact velocities of the new data set appear to agree well with the previous data, v_F for the present data between 800 and 900 m/s appears to be considerably slower than for the previous data set. However, even in the new data set, there is considerable variation and uncertainty in the determined values for v_F (as represented by the "error bars"). The geometry of the FF is highly irregular at the lower impact velocities (the leading edge of the opaque region is used as the position of the FF). This is true of the new data set as well as the previous data set. Further, there are fewer optical images available to include in determination of the FF position versus time, from which the FF velocity is determined. It is interesting to note that the two data points at the lowest v_p are for impact onto bare glass, while all the other data points are for experiments where there was a Cu buffer (although the data point at 611 m/s is an experiment where the rod just grazed the buffer). Therefore, low values for v_F in the present experiments may be an effect of the Cu buffer (or plate) on initiating damage within the glass.

The FF velocities as a function of impact velocity are shown in Fig. 34 for the all the previous and current data. It was observed in Ref. [8] that lead (DEDF) glass had a linear $v_F - v_p$ relationship. A linear regression analysis of all the data is shown as the dot-dashed line in Fig. 34. It is evident that a linear $v_F - v_p$ relationship for borosilicate glass provides a very poor estimate of v_F as a function of v_p.

A regression analysis using the nonlinear function

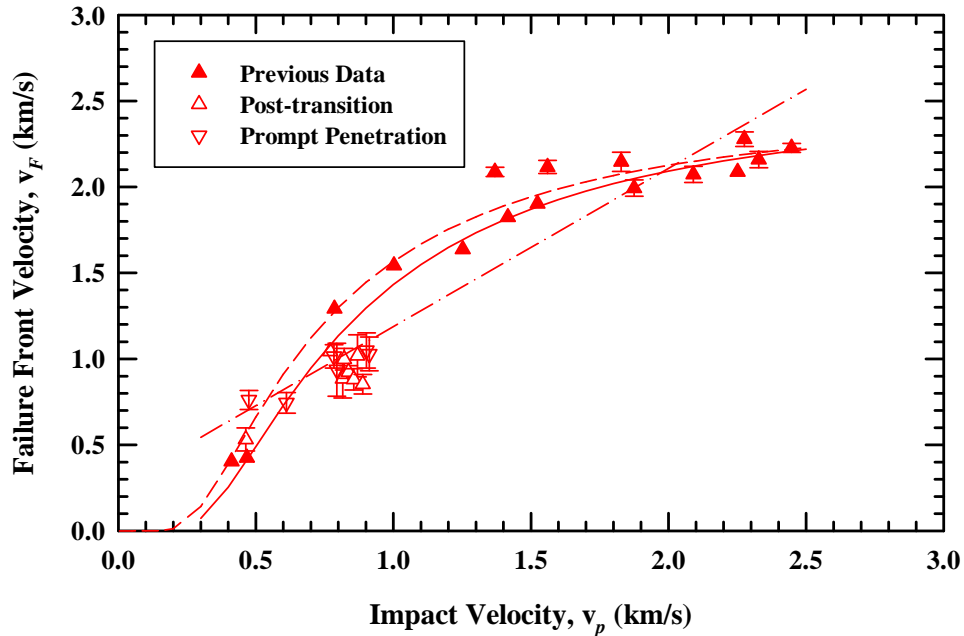$$\ln v_F = a + \frac{b}{v_p^{1.5}} \tag{11}$$

Figure 34. Comparison of post-transition failure front velocities with previous data [8], all impact velocities.

Table 6. Results for Regression Analysis Using Eqn. (11)

	a	b	r^2	Standard Error
All Data	0.9455	–0.5863	0.9008	0.197 km/s
Bare Glass	0.9209	–0.4720	0.9721	0.116 km/s

was conducted.[14] The result of the regression using all the data is shown as the solid line in Fig. 34; whereas, the dashed line does not include the buffer (and cover plate) data in the regression analysis. The coefficients of Eqn. (11) are given in Table 6 for the two fits, where the impact and consumption velocities are in km/s.

Clearly, the FF velocity as a function of impact velocity is nonlinear for borosilicate glass. It also appears that the FF velocity is lower, for whatever reason, for a buffered target than it is for a bare target. This may be due to elimination of the high stresses from the impact shock in the buffered targets. It has been proposed that the penetration stress drives the failure front [12]. Although the impact shock is quickly dissipated by rarefaction waves, the high stresses from the shock probably result in a faster FF velocity (since it is observed that the FF velocity is dependent on the impact velocity, i.e., the driving stress).

There were three experiments (10863, 11113, and 11116) that had a sufficient number of optical images to estimate the speed of formation of the damage ring observed for all the sustained dwell and dwell-transition penetration experiments (for example, see Fig. 20 for the optical and X-ray images, and Fig. 4 for an example of the position-time data). These velocities are 293±40, 224±28, and 242±9 m/s, respectively, for the three experiments. These three data

---

[14] There is no theoretical justification for a fit of the form of Eqn. (11). It is simply a function that does reasonably well at providing an estimate for v_F as a function of v_p.

points are plotted as the solid squares in Fig. 35 for comparison with the FF velocities, v_F. The velocity for developing this damage torus is considerably less than the failure front velocities associated with penetration; thus, these data support our interpretation that the formation of the damage torus represents a different failure mechanism than damage associated with penetration and what we have defined as the failure front.
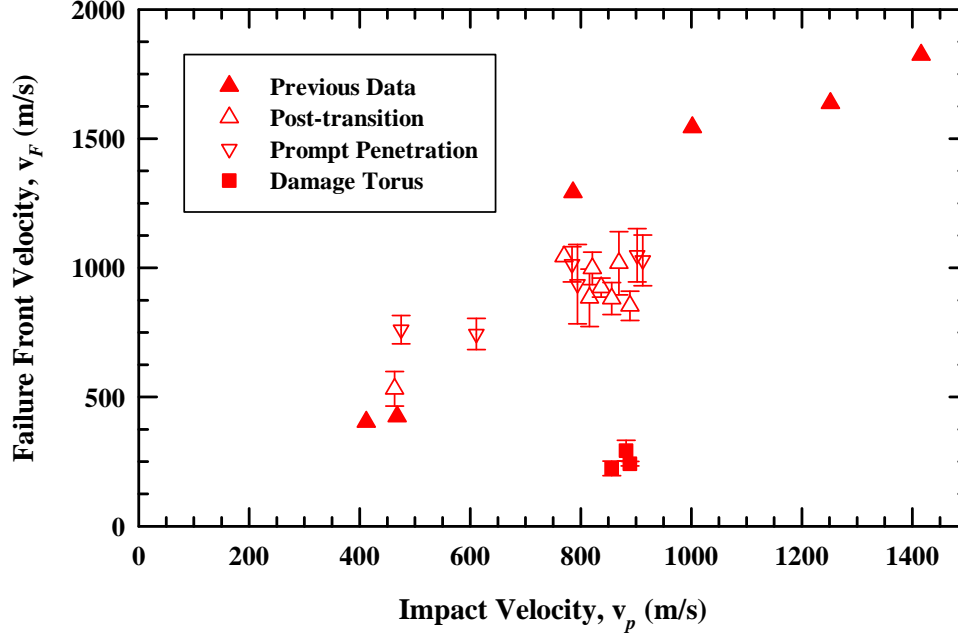

Figure 35. Failure front velocities and formation speed of damage torus (previous data from Ref. [8]).

4.10 Penetration Resistance

Target resistance R_t of the glass was calculated from the Tate equation [16-17]:

$$R_t - Y_p = \frac{1}{2}\rho_p v_c^2 - \frac{1}{2}\rho_t u^2 \qquad (12)$$

with the u and v_c values obtained from the experiments, and with a penetrator strength (since the gold is relatively soft) $Y_p \approx 0$. The Bernoulli pressure for sustained dwell is given by $\frac{1}{2}\rho_p v_p^2$, which is a lower bound on R_t, and is shown as the dashed line in Fig. 36.

The solid squares denote the target resistance for borosilicate glass from the previous experiments [8]. The values for v_c and u for the present experiments are given in Table 2, and the calculated values for the pre- and post-transition R_t's are given in Table 7. The solid circles denote the target resistance during dwell. Note that these are either equal to or very close to the dashed line. Recall that, in some instances of dwell, the measured consumption velocity was not equal to the impact velocity, denoting some very small but immeasurable penetration velocity. These data points lie a little below the dashed line.

Experiments that had estimated dwell times less than 10 µs are denoted with the open squares, while the post-transition target resistance is represented by the open circles. Within the data scatter, there is no distinction between the target resistances for the no-dwell and post-transition data. Additionally, within the data scatter, there appears to be no distinction between the target resistances, as a function of impact velocity, calculated for the previous data.
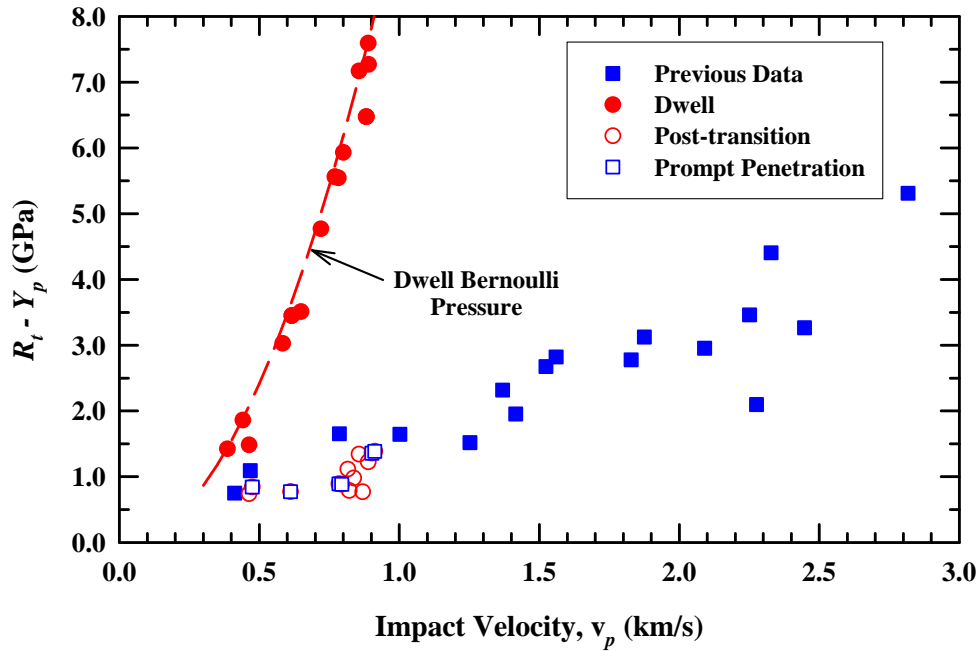
Figure 36. Penetration resistance as a function of impact velocity.

Table 7. Target Resistance Before and After Transition

Exp.	v_p [m/s]	Target Response	R_t [GPa] Before Transition	R_t [GPa] After Transition
11107	386±1	sust. dwell	1.42	-
11108	441±1	sust. dwell	1.86	-
11110	463±2	transition	1.48	0.74
11109	475±3	penetration	-	0.84
10850	583±1	sust. dwell	3.03	-
10853	649±5	sust. dwell	3.51	-
10854	720±1	sust. dwell	4.77	-
10858	782±3	sust. dwell	5.54	-
11111	800±2	sust. dwell	5.93	-
10862	890±5	sust. dwell	7.27	-
10852	616±2	transition	3.45	-
10856	770±3	transition	5.56	-
10861	816±5	transition	-	1.11
10860	821±3	transition	-	0.79
10859	837±4	transition	-	0.98
11112	869	transition	-	0.77
10863*	882±4	transition	6.47	
10851	611±2	penetration	-	0.77
10857	784±5	penetration	-	0.89
10855	794±7	penetration	-	0.88
11114	902±3	penetration	-	1.36
11116	856±2	transition	7.17	1.34
11113	889±3	transition	7.59	1.23
11115	912±1	penetration	-	1.38

In case of bare glass targets, the transition velocity of 450 m/s gives a R_t value of ≈2 GPa for dwell, almost three times as much as for penetration at around the same impact velocity. In case of buffered glass, values for R_t up to 7.6 GPa were achieved for v_p = 890 m/s (Exp. 10862), a value very close to the HEL of borosilicate glass [10,19]. However, once penetration begins (for those experiments with transition), R_t drops dramatically to values around 1 GPa.

4.11 Buffer Mechanics

It was concluded in Ref. [9] that the buffer was effective in dissipating the impact shock, so that the surface of the ceramic (in the case of Ref. [9]) was subjected only to the steady-state Bernoulli stress. For the case of SiC-N [15], this increased the dwell-penetration transition stress from approximately 800 m/s to 1550 m/s, as determined in the experiments.

Referring to Fig. 13, dwell is observed on bare glass up to impact velocities of 450 m/s. The shock stress for the Au rod into glass at 450 m/s is 3.78 GPa. The velocity of the rod to achieve a Bernoulli stress of 3.78 GPa is 625 m/s. Dwell times for the experiments with a Cu buffer or cover plate are shown in Fig. 27. With the Cu buffer, dwell conditions persist up to an impact velocity of ~850 m/s. The Bernoulli stress for a velocity of 850 m/s is 6.97 GPa, which is substantially higher than the shock stress. However, as already evident, bare glass cannot sustain a shock stress of 6.97 GPa (which would occur at an impact velocity of ~780 m/s).

Thus, we conclude that the buffer is doing more than simply removing the shock stress. Simulations in Ref. [9] show that the loading stress is considerably more gradual with the buffer; the loading profile is relatively linear over ~1.0-1.5 µs (which is about 10 times longer than the unloading time from the shock for the 1-mm diameter Au rod), with the ramp becoming somewhat less steep as the buffer thickness increases (for the conditions examined). Therefore, it appears that ramp loading is another important feature—in addition to eliminating the shock stress—provided by the buffer. At this point, the operable mechanics is not fully understood, so we simply report our observations.

5.0 Summary and Conclusions

Twenty-four experiments were performed to provide fundamental data and insight into the phenomenon of interface defeat and dwell transition for brittle materials. The tests were for long gold rods impacting borosilicate targets. The glass targets were of three types: 1) bare, 2) had a Cu buffer which the rod impacted initially and penetrated before impacting the glass, and 3) had a full Cu cover plate. The Cu buffers and cover plates had a nominal thickness of 2.5 mm (2.5-rod diameters). The tests were performed in the reverse ballistic mode with impact velocities ranging from 386 m/s to 912 m/s. Interface defeat, dwell transition, and penetration were measured using multiple tube flash radiography and high-speed photography. The flash X-ray data provided penetration-time and rod length-time data. The high-speed photography allowed observation and measurement of the development of the failed region (failure front) in the glass.

Essential results of these experiments are as follow.

1. Interface defeat is observed for $v_p \leq$ ~450 m/s for bare borosilicate glass. Transition from interface defeat to penetration occurs at about 450 m/s, i.e., $v_t \approx$ 450 m/s, which produces a shock stress of 3.78 GPa.

2. A Cu buffer attached to the glass surface increases the velocity required for penetration by a factor of ~2. With a small Cu buffer, interface defeat was observed for $v_p \leq$ 800 m/s as long as the gold rod was fully engaged by the buffer. If the rod only partially overlapped the buffer, or missed the buffer all together, performance was the same as for a bare (i.e., no-buffer) target.

3. The duration of dwell decreases approximately monotonically for $800 < v_p < 900$ m/s. We estimate the transition velocity to be $v_t = 850 \pm 50$ m/s. In one experiment, interface defeat occurred for $v_p = 890$ m/s.

4. A full cover plate showed similar v_p-dwell response as a finite-diameter buffer; however, the full cover plate eliminated the possibility of an edge or near-edge hit on the buffer.

5. No dwell is observed for impact velocities, $v_p > 896 \pm 6$ m/s for any of the three target types.

6. The stress at the surface of the glass for sustained dwell is approximately 7.0 GPa, which is substantially above the 3.78 GPa shock stress for sustained dwell on bare glass. Therefore, the mechanics of the Cu buffer is more complex than simply eliminating the impact shock. Simulations show that the buffer results in ramp loading of the surface; thus, ramp loading may be another important attribute for the effectiveness of the buffer.

7. Penetration and consumption velocities could be measured to relatively high accuracies before and after dwell transition (as appropriate).

8. Some erosion of the front surface of the glass is inferred from the experimental data for many of the sustained dwell experiments. This erosion is on the order of a couple of millimeters or so (1 to 2 rod diameters).

9. For experiments where dwell transitioned to penetration, the post-dwell penetration velocity is no different than the penetration velocity where there

was little or no dwell. Thus, it can be stated that penetration of the rod is not influenced by an earlier dwell phase.

10. The post-dwell penetration and consumption velocities agree well with previous long-rod data [8].

11. During dwell, the optical pictures reveal a damage region near the impact surface of the glass (depth ~10 mm = 10 rod diameters) that remains constant. The remaining length of the glass stays intact. The velocity of the formation of this damage region is very small compared to the failure front velocity associated with penetration. These observations support an interpretation that this damage formation is the result of different mechanics (e.g., a failure cone) than the failure front associated with penetration.

12. Once penetration sets in—for those experiments where there is a dwell-penetration transition—failure starts to propagate further into the glass and the distance between the failure front and rod tip increases.

13. Failure front velocities measured during the dwell-penetration transition seem to be somewhat lower than values for instant penetration. This could be because of the evaluation procedure (fewer camera images) or to differences in loading rate of the glass.

14. Target resistance in terms of the Tate parameter R_t, assuming strength of the gold rod is zero, is calculated from the measured values for penetration and consumption velocities. During dwell R_t is then found to be at or just slightly less than the Bernoulli (stagnation) pressure of $\frac{1}{2} \rho_p v_p^2$.

15. Experiments with dwell at the highest investigated velocities show R_t values near the HEL (8 GPa) of borosilicate glass. It is remarkable that such strengths can be achieved with a brittle material under rod impact conditions. Although this might suggests that the pressure associated with the onset of dwell to penetration could be the HEL, or a related material property, the transition stress for silicon carbide is considerably higher than its HEL [15].

16. For experiments in which dwell transitions to penetration, after penetration begins R_t is reduced from the value associated with dwell (approximately the Bernoulli pressure) to a constant value of about 1 GPa, the same as observed if there was is no dwell at all (for impact velocities of 800-900 m/s).

6.0 Acknowledgements

7.0 References

1. G. E. Hauver, P. H. Netherwood, R. F. Benck, and L. J. Kecskes, "Ballistic performance of ceramic targets," *Proc. 13th Army Symp. Solid Mech.*, Plymouth, MA (1993).

2. P. Lundberg, R. Renstrom, and B. Lundberg, "Impact of metallic projectiles on ceramic targets: transition between interface defeat and penetration," *Int. J. Impact Engng.*, **24**(3): 259-275 (2000).

3. P. Lundberg and B. Lundberg, "Transition between interface defeat and penetration for tungsten projectiles and four silicon carbide materials," *Int. J. Impact Engng.*, **31**(7): 781-792 (2005).

4. G. E. Hauver, E. J. Rapacki, Jr., P. H. Netherwood, and R. F. Benck, "Interface Defeat of Long-Rod Projectiles by Ceramic Armor," Army Research Laboratory Report, ARL-TR-3590, Aberdeen Proving Ground, MD (2005).

5. C. E. Anderson, Jr., T. Behner, D. L. Orphal, V. Hohler, and M. Moll, "Failure Kinetics of Lead and Borosilicate Glass Against Long-Rod Impact," SwRI Report 18.10174/04, prepared for U.S. Army RDECOM-TARDEC, Warren, MI, August (2006).

6. D. L. Orphal, Th. Behner, V. Hohler, C. E. Anderson, Jr., and D. W. Templeton, "Failure Wave in DEDF and Soda-Lime Glass During Rod Impact," *Shock Compression in Condensed Matter–2005*, (M. D. Furnish, M. Elert, T. P. Russell, and C. T. White, Eds.), AIP Conf. Series 845, 1391-1394, AIP, Melville, NY (2006).

7. D. L. Orphal, C. E. Anderson, Jr., T. Behner, V. Hohler, M. Wickert, and D. W. Templeton, "Failure Kinetics in Borosilicate Glass During Rod Impact," *Shock Compression of Condensed Matter— 2007*, (M. Elert, *et al.*, Eds.), AIP Conf. Series 955, pp. 759-762, AIP, Melville, NY (2007).

8. T. Behner, C. E. Anderson, Jr., D. L. Orphal, V. Hohler, M. Moll, and D. W. Templeton, "Penetration and Failure of Lead and Borosilicate Glass against Rod Impact," *Int. J. Impact Engng.*, **35**(6), 447-456 (2008).

9. T. J. Holmquist, C. E. Anderson, Jr., and Th. Behner, "Design, Analysis and Testing of an Unconfined Ceramic Target to Induce Dwell," *Proc. 22nd Int. Symp. Ballistics*, **2**, 860-867, DEStech Publications, Inc., Lancaster, PA (2005).

10. N. K. Bourne, J. C. F. Millett, Z. Rosenberg, and N. H. Murray, "On the shock induced failure of brittle solids", J. Mech. Phys. Solids, 46: 1887-1908 (1998).

11. C. E. Anderson, Jr., D. L. Orphal, T. Behner, and M. Wickert, "Failure and Penetration Response of Borosilicate Glass During Short-Rod Impact," SwRI Report 18.12544/004, prepared for U.S. Army RDECOM-TARDEC, AMSRD-TAR-R, Warren, MI, May (2008)

12. C. E. Anderson, Jr., D. L. Orphal, and T. Behner, "The Failure and Penetration Response of Borosilicate Glass During Short-Rod Impact," *Int. J. Impact Engng.*, doi: 10.1016/ j.ijimpeng.2008.12.002 (2009).

13. C. E. Anderson, Jr. and J. D. Walker, "An Examination of Long-Rod Penetration," *Int. J. Impact Engng.*, **11**(4), 481-501 (1991).

14. D. J. Steinberg, "Equation of State and Strength Properties of Selected Materials," UCRL-MA-106439, Rev. 1, Lawrence Livermore National Laboratory, Livermore, CA (1996).

15. C. E. Anderson, Jr., T. Behner, T. J. Holmquist, Dennis L. Orphal, and M. Wickert "Dwell and Interface Defeat of Long Rods Impacting Silicon Carbide," SwRI Report 18.12544/008, prepared for RDECOM-TARDEC, AMSRD-TAR-R, Warren, MI, March (2009).

16. A. S. Vlasov, E. L. Zilberbrand, A. A. Kozhushko, A. I. Kozachuk, A. B. Sinani and M. I. Stepanov. "Ballistic behavior of strengthened silicate glass", *Proc. 20th Int. Symp. Ballistics*, 982-987, Orlando, FL (2002).

17. A. Tate, "Theory for the Deceleration of Long Rods after Impact," *J. Mech. Phys. Solids*, **15**, 387-399 (1967).

18. A. Tate, "Further Results in the Theory of Long Rod Penetration," *J. Mech. Phys. Solids*, **17**, 141-150 (1969).

19. A. A. Wereszczak, K. E. Johanns, Ch. E. Anderson Jr., Th. Behner, P. Patel and D. W. Templeton, "Strength and contact damage response in a soda-lime-silicate and a borosilicate glass", *Proc. 25th Army Science Conf.*, Orlando, Florida, November 27-30 (2006).

20. Th. Behner, M. Moll, V. Hohler. "Failure Kinetics of DEDF and Borosilicate Glass against Rod Impact", EMI-Report I-61/05, 2005.

Appendix

The appendix contains the table with the trigger times of the X-ray and camera as well as the X-ray and camera pictures for each of the experiments. The pictures are sorted according to the experimental table (bare – buffered – cover plated).

A-2

Table A-1.   Times in μs before/after impact for each individual frame of the Flash X-rays.

Exp./frame	1	2	3	4	5
10850	-45.916	-5.789	23.415	53.350	98.650
10851	-37.149	32.196	71.358	91.148	-
10852	-35.301	34.951	74.454	94.144	126.184
10853	-19.578	52.933	89.733	109.383	131.953
10854	-24.405	35.094	54.499	74.381	99.831
10855	-16.811	33.001	52.511	72.032	97.326
10856	-20.512	28.642	48.380	67.577	-
10857	-22.724	27.322	46.953	66.366	86.584
10858	-20.410	29.481	49.224	68.712	88.709
10859	-15.405	34.021	53.748	73.223	93.711
10860	-14.088	33.224	53.010	72.376	92.660
10861	-16.207	33.721	53.207	72.850	93.008
10862	-16.761	22.980	42.988	62.429	82.727
10863	-9.875	29.067	48.389	67.958	88.284
11107	-25.122	14.633	45.819	75.032	115.082
11108	-21.263	18.639	44.656	69.073	109.061
11109	-10.435	29.464	54.866	79.731	119.620
11110	-16.130	23.648	49.327	73.844	113.894
11111	-18.089	11.789	32.742	52.210	72.329
11112	-11.074	18.786	39.846	-	79.220
11113	-17.446	12.469	33.173	52.773	72.863
11114	-13.891	16.015	36.615	56.447	76.629
11115	-18.413	11.429	32.238	51.862	71.976
11116	-17.080	12.792	33.335	53.022	73.085

**Table A-2. Times in μs before/after impact for each individual frame
of the high-speed camera pictures.**

Exp/frame	1	2	3	4	5	6	7	8	9	10	11	12	13	14	15	16
10850	-47.984	-37.984	-27.984	-17.984	-7.984	2.016	12.016	22.016	32.016	42.016	52.016	62.016	72.016	82.016	92.016	102.016
10851	-39.758	-24.758	-14.758	-4.758	5.242	15.242	25.242	35.242	45.242	55.242	65.242	75.242	85.242	95.242	105.242	115.242
10852	-36.285	-21.285	-11.285	-1.285	8.715	18.715	28.715	38.715	48.715	58.715	68.715	78.715	88.715	98.715	108.715	118.715
10853	-21.000	-6.000	4.000	14.000	24.000	34.000	44.000	54.000	64.000	74.000	84.000	94.000	104.000	114.000	124.000	134.000
10854	-26.825	-18.825	-10.825	-2.825	5.175	13.175	21.175	29.175	37.175	45.175	53.175	61.175	69.175	77.175	85.175	93.175
10855	-18.715	-11.715	-4.715	2.285	9.285	16.285	23.285	30.285	37.285	44.285	51.285	58.285	65.285	72.285	79.285	86.285
10856	-23.606	-16.606	-9.606	-2.606	4.394	11.394	18.394	25.394	32.394	39.394	46.394	53.394	60.394	67.394	74.394	81.394
10857	-24.838	-17.838	-10.838	-3.838	3.162	10.162	17.162	24.162	31.162	38.162	45.162	52.162	59.162	66.162	73.162	80.162
10858	-22.798	-15.798	-8.798	-1.798	5.202	12.202	19.202	26.202	33.202	40.202	47.202	54.202	61.202	68.202	75.202	82.202
10859	-17.964	-10.964	-3.964	3.036	10.036	17.036	24.036	31.036	38.036	45.036	52.036	59.036	66.036	73.036	80.036	87.036
10860	-18.736	-11.736	-4.736	2.264	9.264	16.264	23.264	30.264	37.264	44.264	51.264	58.264	65.264	72.264	79.264	86.264
10861	-18.807	-11.807	-4.807	2.193	9.193	16.193	23.193	30.193	37.193	44.193	51.193	58.193	65.193	72.193	79.193	86.193
10862	-18.711	-11.711	-4.711	2.289	9.289	16.289	23.289	30.289	37.289	44.289	51.289	58.289	65.289	72.289	79.289	86.289
10863	-13.462	-6.462	0.538	7.538	9.538	11.538	13.538	15.538	17.538	26.538	36.538	46.538	56.538	66.538	76.538	86.538
11107	-25.334	-15.384	-9.384	-3.384	2.616	9.616	16.616	24.616	34.616	44.616	56.616	69.616	84.616	99.616	114.616	134.616
11108	-20.812	-10.862	-4.862	1.138	7.138	14.138	21.138	29.138	39.138	49.138	61.138	74.138	89.138	104.138	119.138	139.138
11109	-10.834	-0.884	5.116	11.116	17.116	24.116	31.116	39.116	49.116	59.116	71.116	84.116	99.116	114.116	129.116	149.116
11110	-17.120	-7.170	-1.170	4.830	10.830	17.830	24.830	32.830	42.830	52.830	64.830	77.830	92.830	107.830	122.830	142.830
11111	-18.431	-11.481	-4.481	2.519	9.519	16.519	23.519	30.519	37.519	44.519	51.519	58.519	65.519	72.519	79.519	86.519
11112	-11.841	-4.891	2.109	9.109	16.109	23.109	30.109	37.109	44.109	51.109	58.109	65.109	72.109	79.109	86.109	93.109
11113	-17.927	-10.977	-3.977	3.023	10.023	17.023	24.023	31.023	38.023	45.023	52.023	59.023	66.023	73.023	80.023	87.023
11114	-14.538	-7.588	-0.588	6.412	13.412	20.412	27.412	34.412	41.412	48.412	55.412	62.412	69.412	76.412	83.412	90.412
11115	-18.959	-12.009	-5.009	1.991	8.991	15.991	22.991	29.991	36.991	43.991	50.991	57.991	64.991	71.991	78.991	85.991
11116	-17.092	-10.142	-3.142	3.858	10.858	17.858	24.858	31.858	38.858	45.858	52.858	59.858	66.858	73.858	80.858	87.858

A-3

Table A-3. X-Ray and Photographic Measurements
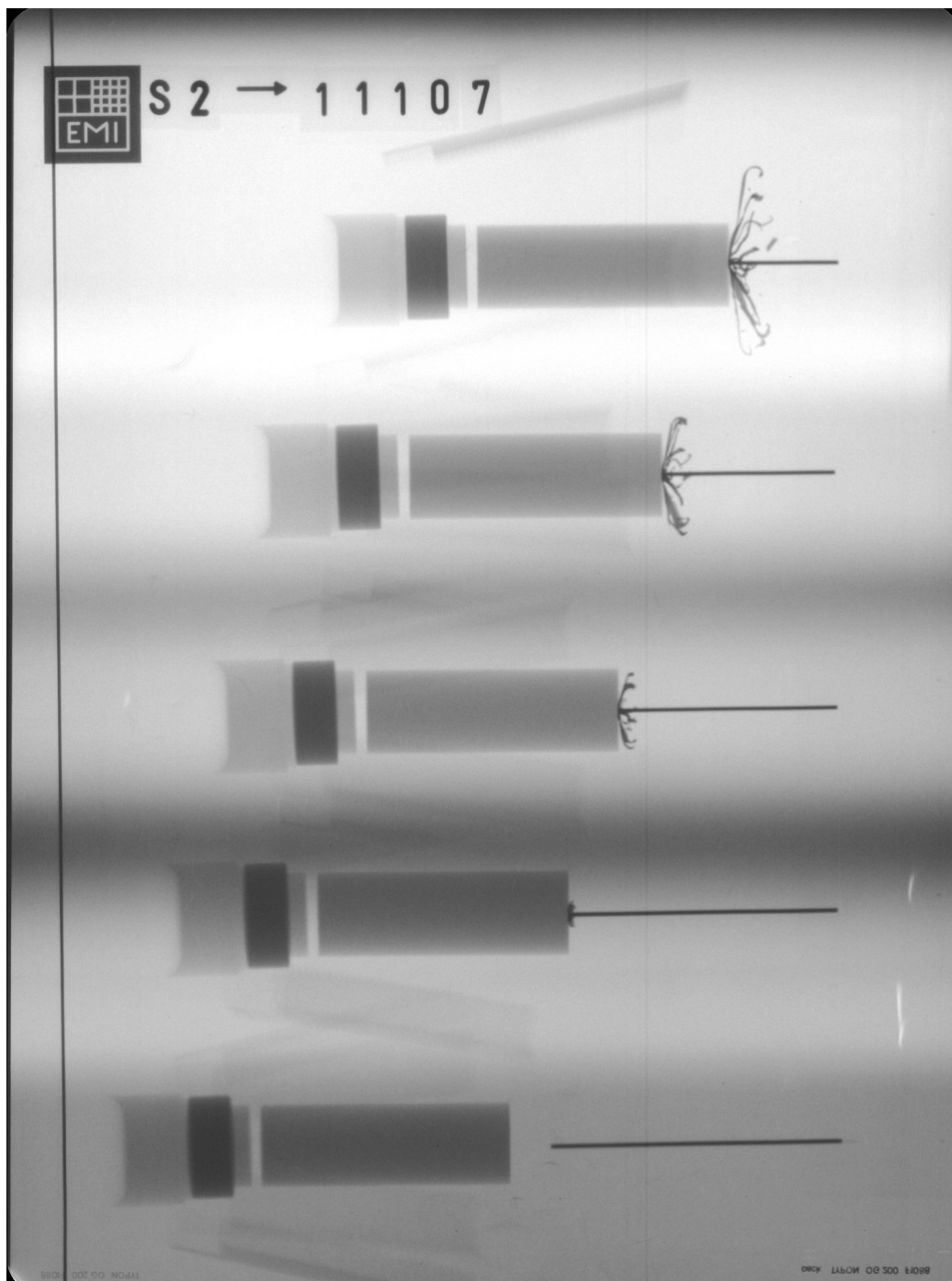
|	Time [μs]	Pen Depth [mm]	Rod Length [mm]	Time [μs]	FF Position [mm]		Time [μs]	Pen Depth [mm]	Rod Length [mm]	Time [μs]	FF Position [mm]
10850	98.65	0.55	17.26	0.00	0.00	**10851**	91.15	25.61	40.29	0.00	0.00
	53.35	0.53	42.33	12.02	4.34		71.36	19.03	45.98	5.24	1.76
	23.41	0.33	59.41	22.02	7.04		32.20	7.68	57.97	15.24	20.19
	0.00	-2.60	70.23	32.02	8.45		0.00	-2.50	70.05	25.24	33.10
				42.02	8.45					35.24	38.38
				52.02	8.45					45.24	48.00
				62.02	8.33					55.24	52.69
				72.02	8.33					65.24	58.56
				82.02	8.33						
				92.02	8.45						
				102.02	8.33						

	Time [μs]	Pen Depth [mm]	Rod Length [mm]	Time [μs]	FF Position [mm]		Time [μs]	Pen Depth [mm]	Rod Length [mm]	Time [μs]	FF Position [mm]
10852	94.14	3.40	18.06	0.00	0.00	**10853**	131.95	1.69		0.00	0.00
	74.45	0.55	27.26	8.72	2.11		109.38	1.50	4.02	4.00	0.00
	34.95	-0.01	50.89	18.72	5.99		89.73	0.64	15.65	14.00	6.10
	0.00	-2.54	70.15	28.72	6.34		52.93	0.27	38.00	24.00	6.34
				38.72	5.99		0.00	-2.60	70.17	34.00	6.69
				48.72	11.38					44.00	6.57
				58.72	15.26					54.00	6.69
				68.72	23.71					64.00	6.81
				78.72	26.05					74.00	7.04
				88.72	26.29						
				98.72	27.11						
				108.72	38.85						
				118.72	38.61						

Table A-3. X-Ray and Photographic Measurements (Cont'd)

	Time [μs]	Pen Depth [mm]	Rod Length [mm]	Time [μs]	FF Position [mm]		Time [μs]	Pen Depth [mm]	Rod Length [mm]	Time [μs]	FF Position [mm]
10854	99.83	1.83	4.39	0.00	0.00	**10855**	97.33	39.26	32.84	0.00	0.00
	74.38	0.29	20.13	13.17	4.81		72.03	29.45	42.15	2.28	0.00
	54.50	0.27	33.86	21.17	5.52		52.51	20.22	48.28	9.28	10.68
	35.09	0.26	47.74	29.17	5.52		33.00	11.29	54.58	16.28	18.78
	0.00	-2.53	70.18	37.17	5.52		0.00	0.00	70.15	23.28	30.63
				45.17	5.87					30.28	36.03
				53.17	5.87					37.28	44.36
				61.17	5.87					44.28	44.71
				69.17	5.99					51.28	46.83
				77.17	5.75					58.28	50.23
				85.17	5.87					65.28	53.40
										72.28	57.04

	Time [μs]	Pen Depth [mm]	Rod Length [mm]	Time [μs]	FF Position [mm]		Time [μs]	Pen Depth [mm]	Rod Length [mm]	Time [μs]	FF Position [mm]
10856	67.58	6.87	27.88	0.00	0.00	**10857**	86.58	34.68	37.49	0.00	0.00
	48.38	0.44	35.77	4.39	0.00		66.37	26.17	43.93	3.16	0.00
	28.64	0.49	50.76	11.39	5.16		46.95	17.50	50.38	10.16	11.62
	0.00	-2.54	70.26	18.39	8.10		27.32	9.23	57.47	17.16	17.84
				25.39	8.45		0.00	-2.50	70.16	24.16	26.88
				32.39	8.10					31.16	32.27
				39.39	12.67					38.16	35.21
				46.39	16.55					45.16	42.84
				53.39	18.19					52.16	44.13
				60.39	22.65					59.16	53.75
				67.39	31.92					66.16	57.27
				74.39	38.14						
				81.39	44.95						

Table A-3. X-Ray and Photographic Measurements (Cont'd)

	Time [μs]	Pen Depth [mm]	Rod Length [mm]	Time [μs]	FF Position [mm]		Time [μs]	Pen Depth [mm]	Rod Length [mm]	Time [μs]	FF Position [mm]
10858	88.71	0.00	0.00	0.00	0.00	**10859**	93.71	30.77	25.81	0.00	0.00
	68.71	0.77	20.07	5.20	0.00		73.22	20.53	32.31	3.04	0.00
	49.22	0.42	34.49	12.20	5.28		53.75	11.73	39.49	10.04	4.34
	29.48	0.44	49.81	19.20	9.27		34.02	3.01	47.03	17.04	5.75
	0.00	-2.64	70.23	26.20	9.15		0.00	-2.57	70.15	24.04	5.99
				33.20	9.27					31.04	25.94
				40.20	9.39					38.04	34.15
				47.20	9.39					45.04	39.55
				54.20	9.27					52.04	47.88
				61.20	9.27					59.04	52.46
				68.20	9.15					66.04	58.56
				75.20	24.88						
				82.20	24.88						

	Time [μs]	Pen Depth [mm]	Rod Length [mm]	Time [μs]	FF Position [mm]		Time [μs]	Pen Depth [mm]	Rod Length [mm]	Time [μs]	FF Position [mm]
10860	92.66	26.57	23.35	0.00	0.00	**10861**	93.01	18.86	16.16	0.00	0.00
	72.38	16.96	30.18	2.26	0.00		72.85	9.70	22.84	2.19	0.00
	53.01	7.26	36.44	9.26	3.40		53.21	1.90	30.86	9.19	5.40
	33.22	0.35	45.25	16.26	7.63		33.72	0.46	45.16	16.19	8.68
	0.00	-2.56	70.18	23.26	7.86		0.00	-2.60	70.19	23.19	9.15
				30.26	16.55					30.19	10.45
				37.26	27.23					37.19	10.56
				44.26	37.67					44.19	10.68
				51.26	40.37					51.19	10.80
				58.26	48.12					58.19	20.66
				65.26	54.34					65.19	29.11
										72.19	29.57
										79.19	40.02
										86.19	46.12

Table A-3. X-Ray and Photographic Measurements (Cont'd)

	Time [μs]	Pen Depth [mm]	Rod Length [mm]	Time [μs]	FF Position [mm]		Time [μs]	Pen Depth [mm]	Rod Length [mm]	Time [μs]	FF Position [mm]
10862	82.73	0.91	0.00	0.00	0.00	**10863**	88.28	9.19	0.00	0.00	0.00
	62.43	0.95	18.07	2.29	5.75		67.96	2.37	15.66	0.54	0.00
	42.99	0.46	34.65	9.29	6.69		48.39	1.10	31.61	7.54	4.22
	22.98	0.49	52.32	16.29	9.62		29.07	0.33	47.49	9.54	5.40
	0.00	-2.54	70.26	23.29	9.51		0.00	-2.58	70.26	11.54	5.63
				30.29	9.62					13.54	6.10
				37.29	9.62					15.54	6.81
				44.29	9.62					17.54	7.75
				51.29	9.74					26.54	7.63
				58.29	9.62					36.54	8.22
				65.29	9.74					46.54	9.51

	Time [μs]	Pen Depth [mm]	Rod Length [mm]	Time [μs]	FF Position [mm]		Time [μs]	Pen Depth [mm]	Rod Length [mm]	Time [μs]	FF Position [mm]
11107	115.08	0.00	26.13	0.00	0.00	**11108**	109.06	0.00	22.51	0.00	0.00
	75.03	0.00	41.24	2.62	2.14		69.07	0.00	39.74	1.14	0.56
	45.82	0.00	52.61	9.62	5.87		44.66	0.00	50.59	7.14	5.53
	14.63	0.00	64.89	16.62	6.32		18.64	0.00	62.37	14.14	6.55
	0.00	0.00	70.11	24.62	6.32		0.00	0.00	70.14	21.14	7.00
				34.62	6.32					29.14	6.66
				44.62	6.32					39.14	8.58
				56.62	6.55					49.14	9.82
				69.62	6.55					61.14	9.60
				84.62	6.55					74.14	10.16
				99.62	6.77					89.14	13.32
				114.62	6.77					104.14	16.71
				134.62	6.77					119.14	22.92
										139.14	22.58

Table A-3. X-Ray and Photographic Measurements (Cont'd)

	Time [μs]	Pen Depth [mm]	Rod Length [mm]	Time [μs]	FF Position [mm]		Time [μs]	Pen Depth [mm]	Rod Length [mm]	Time [μs]	FF Position [mm]
11109	119.62	18.56	32.35	0.00	0.00	**11110**	113.89	15.07	33.05	0.00	0.00
	79.73	11.61	43.48	5.12	5.42		73.84	8.41	43.94	4.83	5.42
	54.87	7.56	51.24	11.12	12.42		49.33	4.26	51.42	10.83	10.05
	29.46	3.82	59.55	17.12	20.43		23.65	1.85	60.89	17.83	12.08
	0.00	0.00	70.15	24.12	23.03		0.00	0.00	70.16	24.83	17.16
				31.12	31.27					32.83	16.93
				39.12	35.67					42.83	26.19
				49.12	44.14					52.83	31.61
				59.12	48.65					64.83	36.35
				71.12	50.46					77.83	39.51
				84.12	50.46					92.83	41.66
				99.12	50.57					107.83	42.11
				114.12	50.57					122.83	42.45
				129.12	50.57					142.83	42.56
				149.12	50.69						

	Time [μs]	Pen Depth [mm]	Rod Length [mm]	Time [μs]	FF Position [mm]		Time [μs]	Pen Depth [mm]	Rod Length [mm]	Time [μs]	FF Position [mm]
11111	72.33	4.17	18.94	0.00	0.00	**11112**	79.22	28.29	32.56	0.00	0.00
	52.21	0.00	31.73	2.52	0.00		39.85	8.20	45.60	2.11	0.00
	32.74	0.00	46.66	9.52	2.48		18.79	0.00	56.36	9.11	2.48
	11.79	0.00	63.40	16.52	3.84		0.00	-2.55	70.09	16.11	10.84
	0.00	-2.54	70.17	23.52	4.52					23.11	18.17
				30.52	4.40					30.11	27.54
				37.52	4.74					37.11	31.04
				44.52	4.97					44.11	40.75
				51.52	4.85					51.11	46.51
				58.52	5.87					58.11	47.86
				65.52	6.55					65.11	53.51
										72.11	56.90

A-8

Table A-3. X-Ray and Photographic Measurements (Cont'd)

	Time [µs]	Pen Depth [mm]	Rod Length [mm]	Time [µs]	FF Position [mm]		Time [µs]	Pen Depth [mm]	Rod Length [mm]	Time [µs]	FF Position [mm]
11113	72.86	13.56	21.60	0.00	0.00	**11114**	76.63	32.25	36.59	0.00	0.00
	52.77	3.72	29.48	3.02	0.11		56.45	22.07	43.67	6.41	0.00
	33.17	0.00	43.78	10.02	3.61		36.61	12.32	51.67	13.41	10.05
	12.47	0.00	62.15	17.02	5.64		16.01	3.15	61.43	20.41	24.27
	0.00	-2.63	70.17	24.02	5.98		0.00	-2.70	70.14	27.41	30.59
				31.02	8.92					34.41	36.35
				38.02	9.82					41.41	44.59
				45.02	16.82					48.41	48.09
				52.02	21.11					55.41	54.52
				59.02	31.50						
				66.02	35.22						
				73.02	39.85						
				80.02	46.62						
				87.02	50.35						

	Time [µs]	Pen Depth [mm]	Rod Length [mm]	Time [µs]	FF Position [mm]		Time [µs]	Pen Depth [mm]	Rod Length [mm]	Time [µs]	FF Position [mm]
11115	71.98	31.98	38.86	0.00	0.00	**11116**	73.09	11.92	22.20	0.00	0.00
	51.86	22.04	47.28	1.99	0.34		53.02	3.17	30.24	3.86	0.00
	32.24	11.31	54.41	8.99	12.42		33.34	0.00	43.97	10.86	2.26
	11.43	2.36	64.24	15.99	22.01		12.79	0.00	61.67	17.86	3.84
	0.00	-2.56	70.16	22.99	33.53		0.00	-2.53	70.05	24.86	5.64
				29.99	36.58					31.86	5.42
				36.99	43.69					38.86	12.30
				43.99	52.94					45.86	18.51
				50.99	57.80					52.86	22.24
										59.86	28.90
										66.86	38.49
										73.86	40.41
										80.86	46.62
										87.86	54.41

**Figure A-1. X-ray picture for Exp. 11107: bare glass, $v_p = 386$ m/s.**
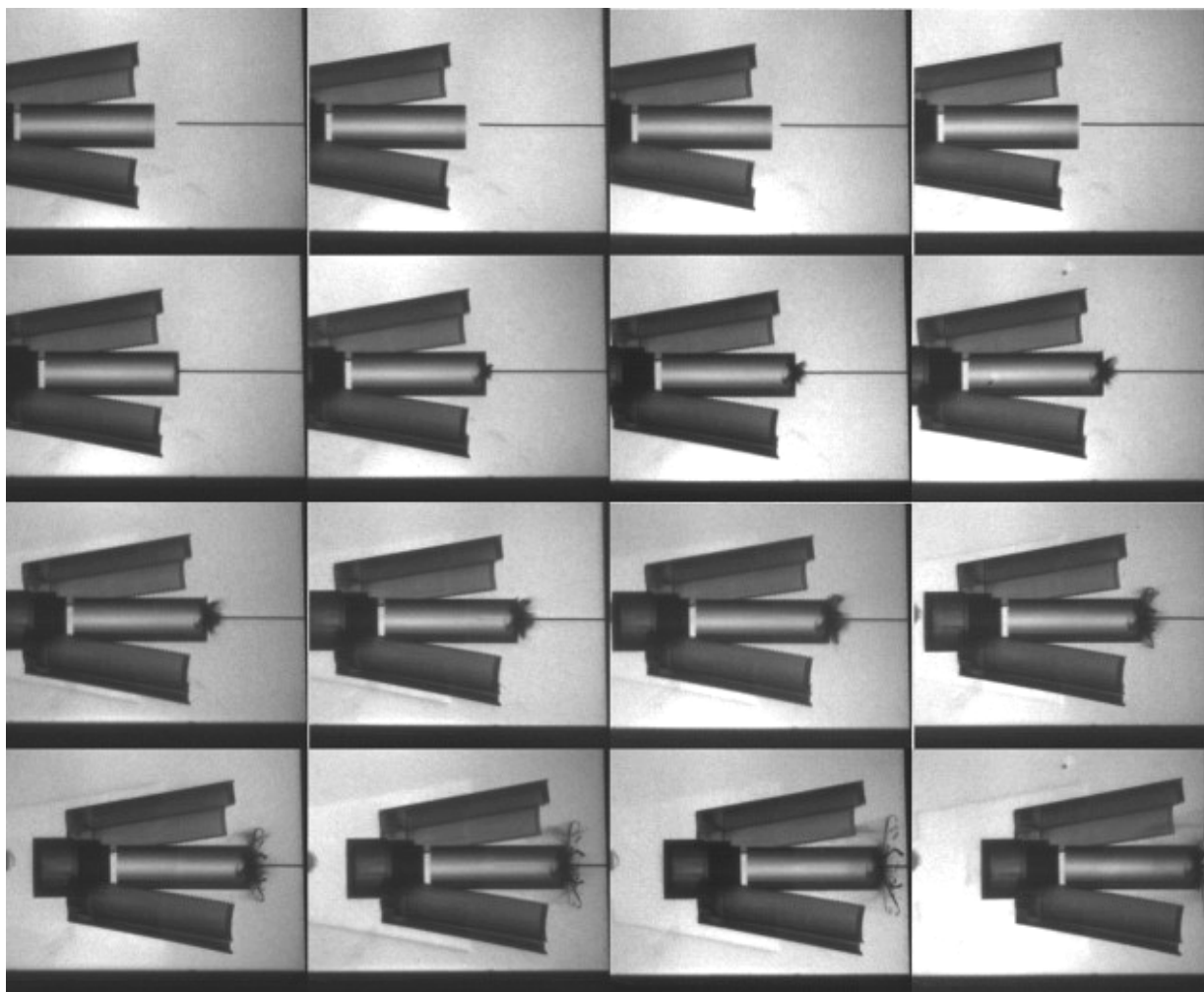
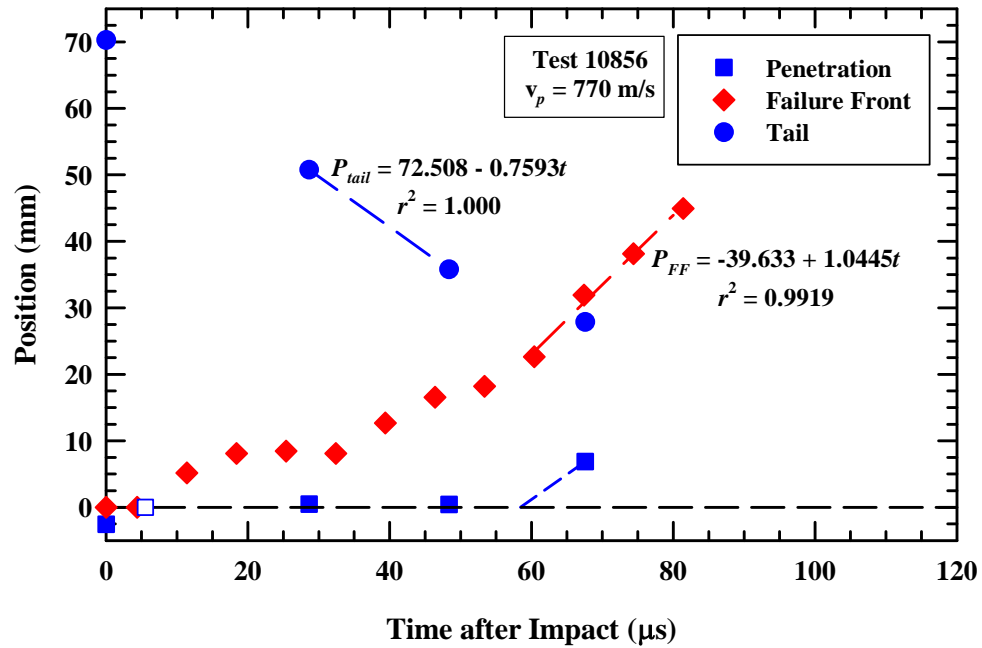**Figure A-2. Camera picture for Exp. 11107: bare glass, v_p = 386 m/s.**
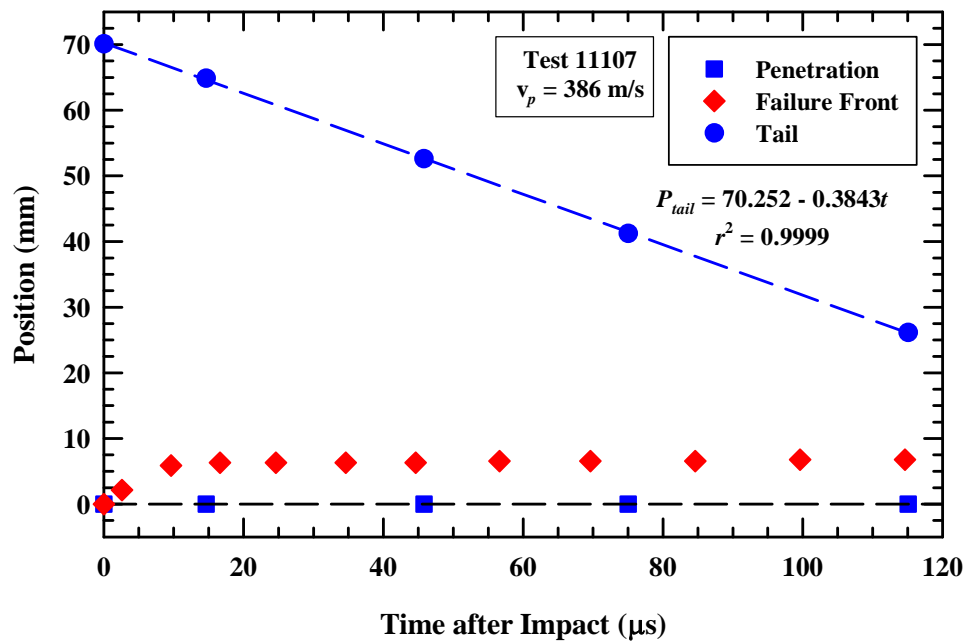
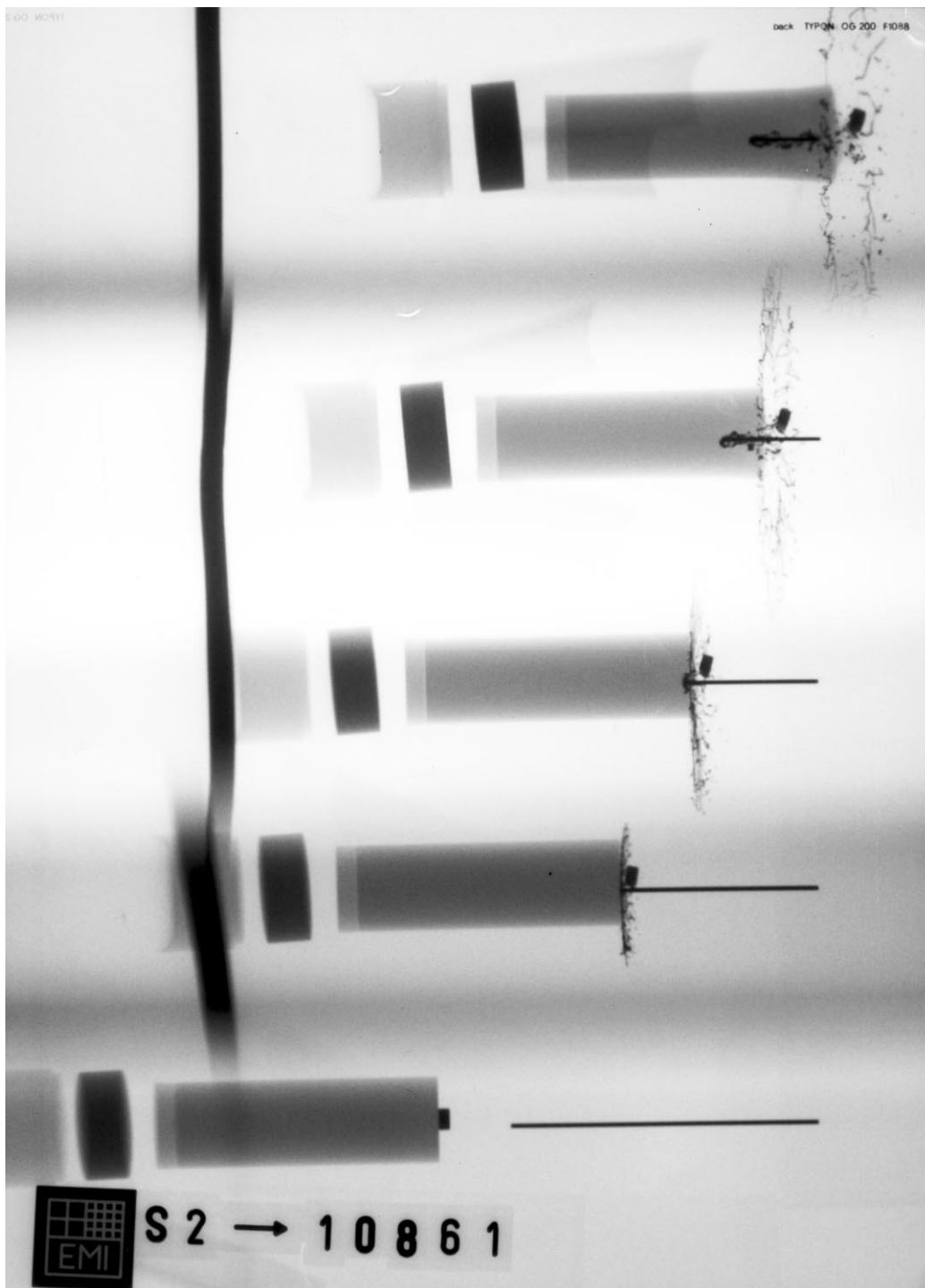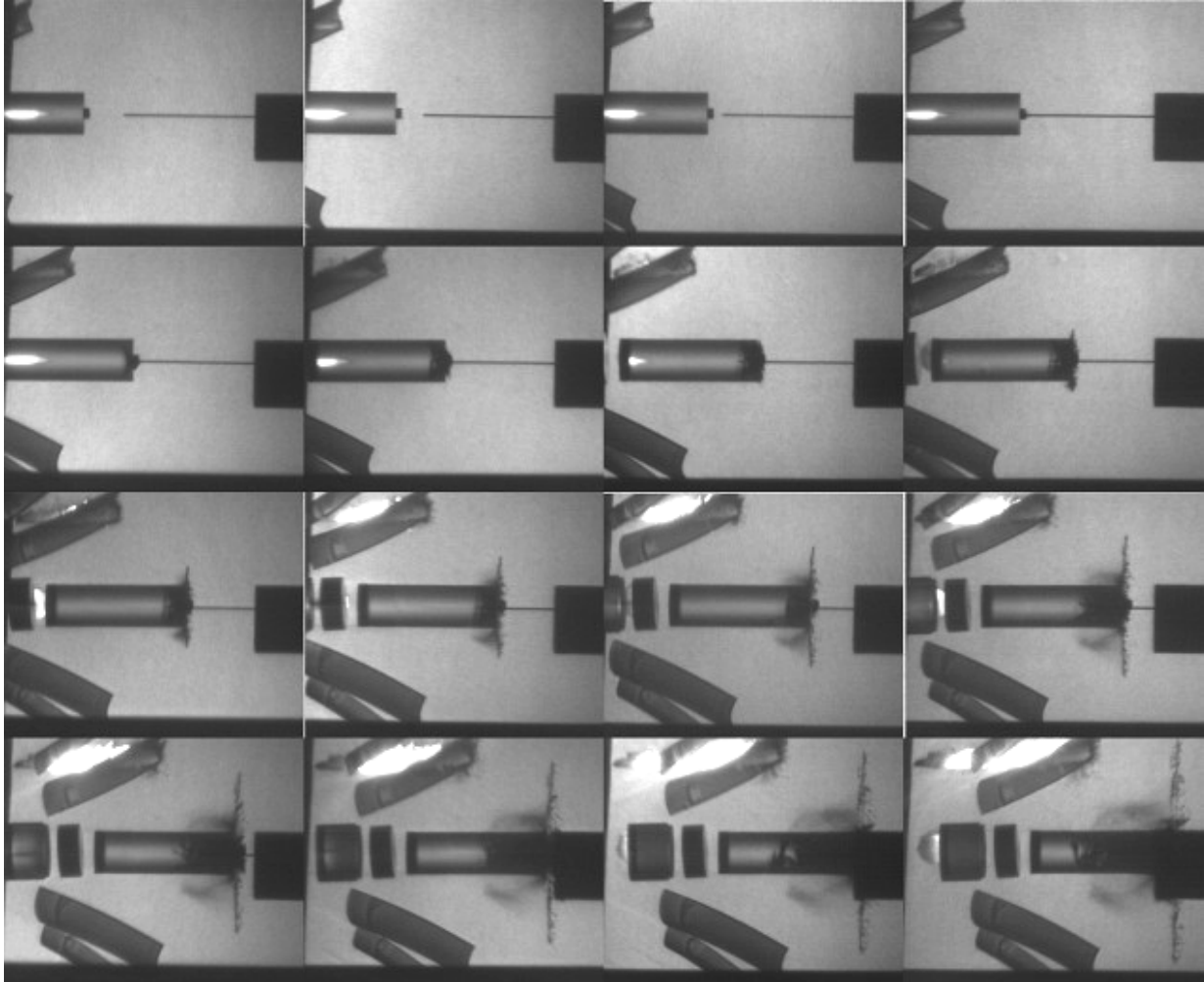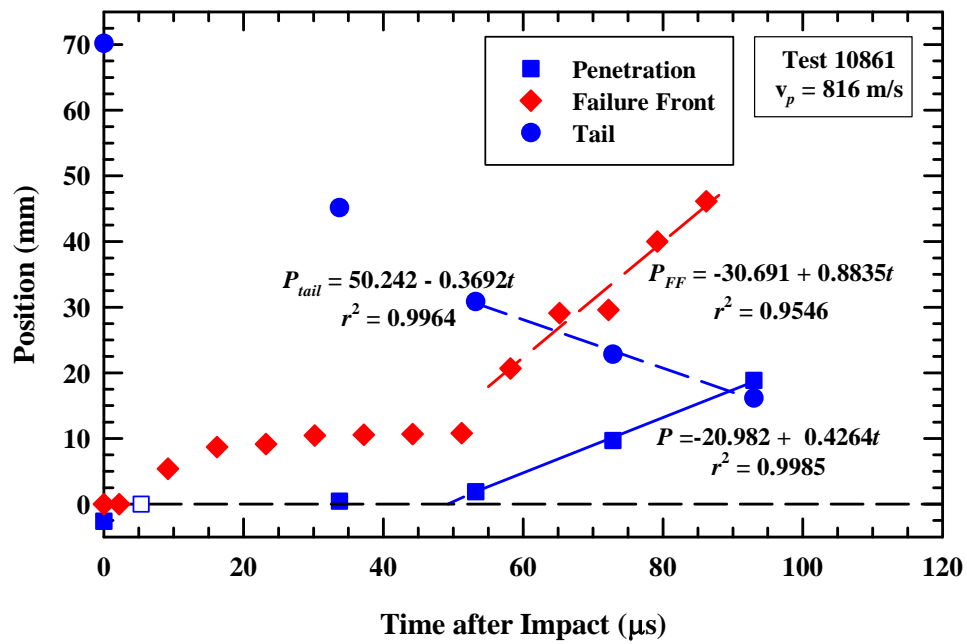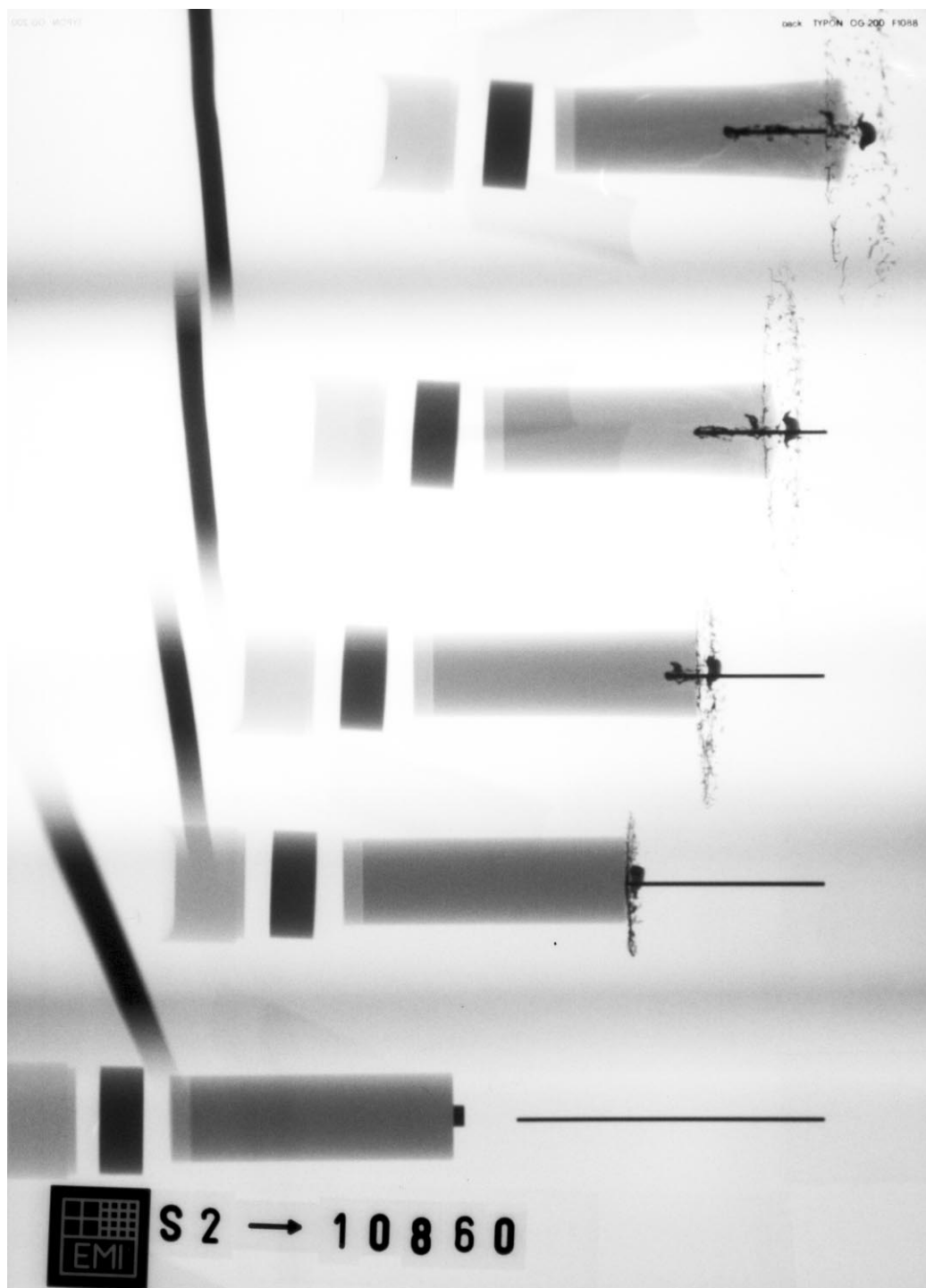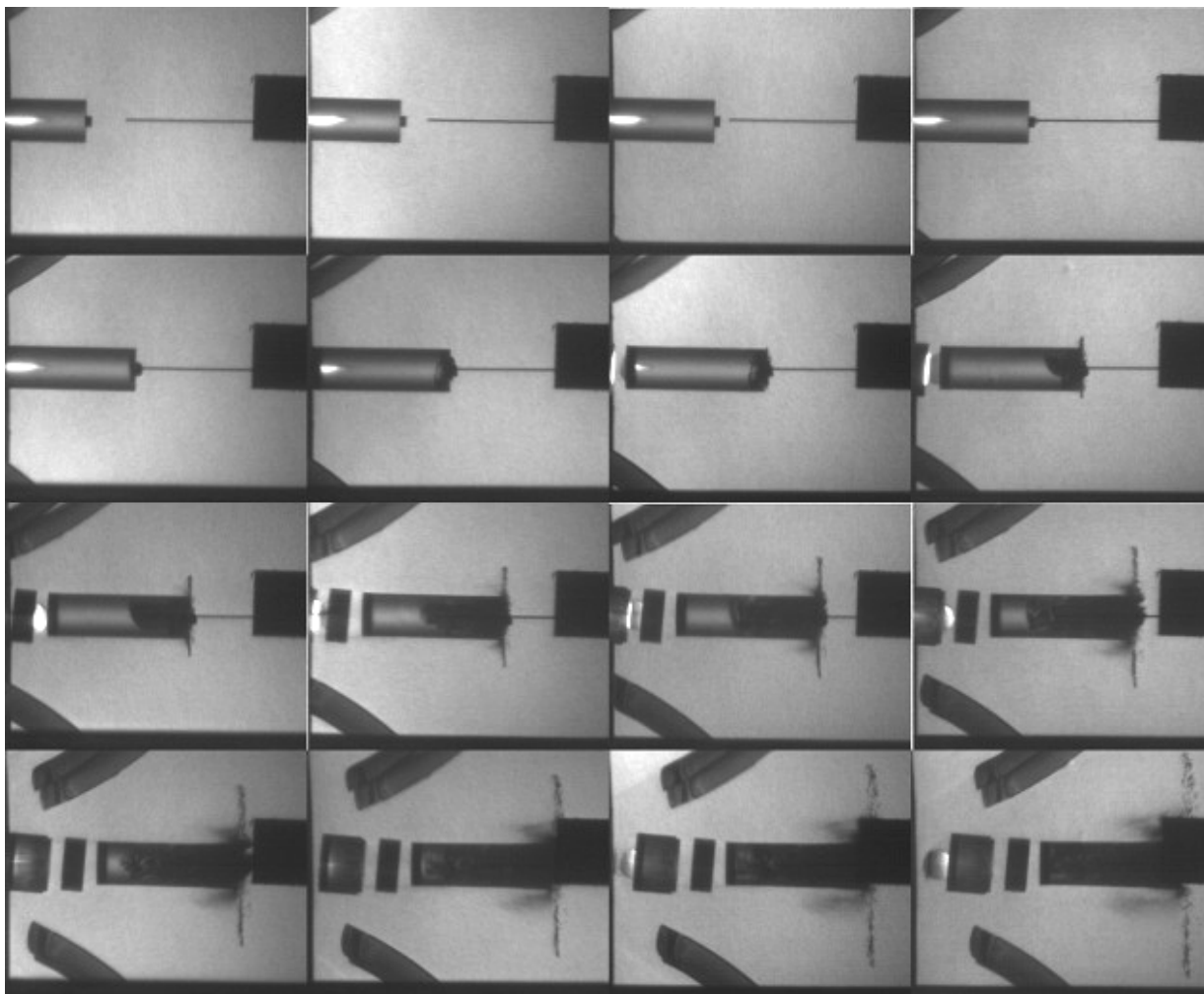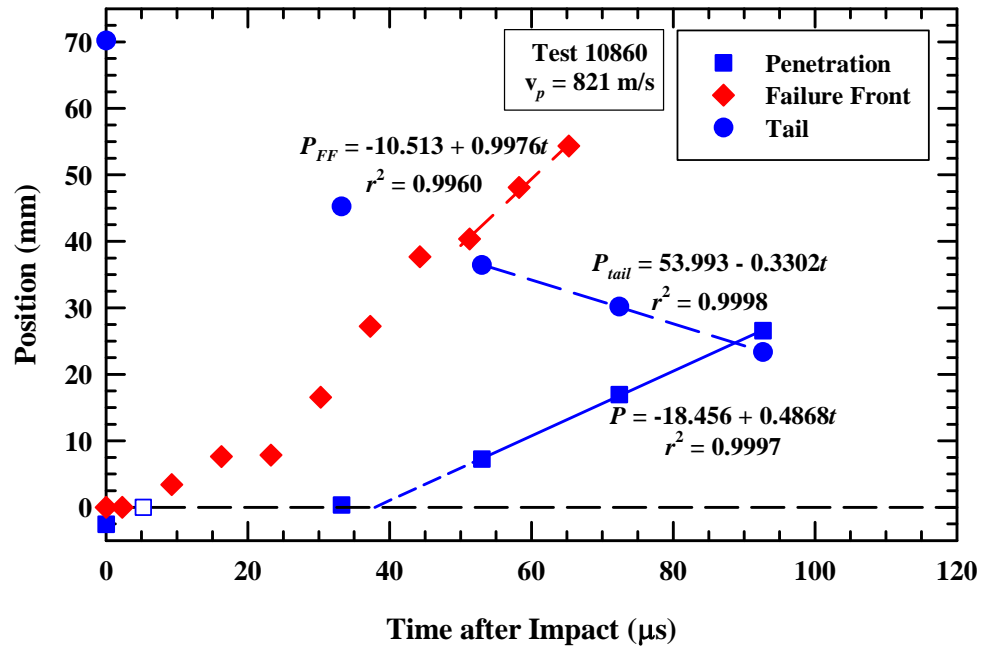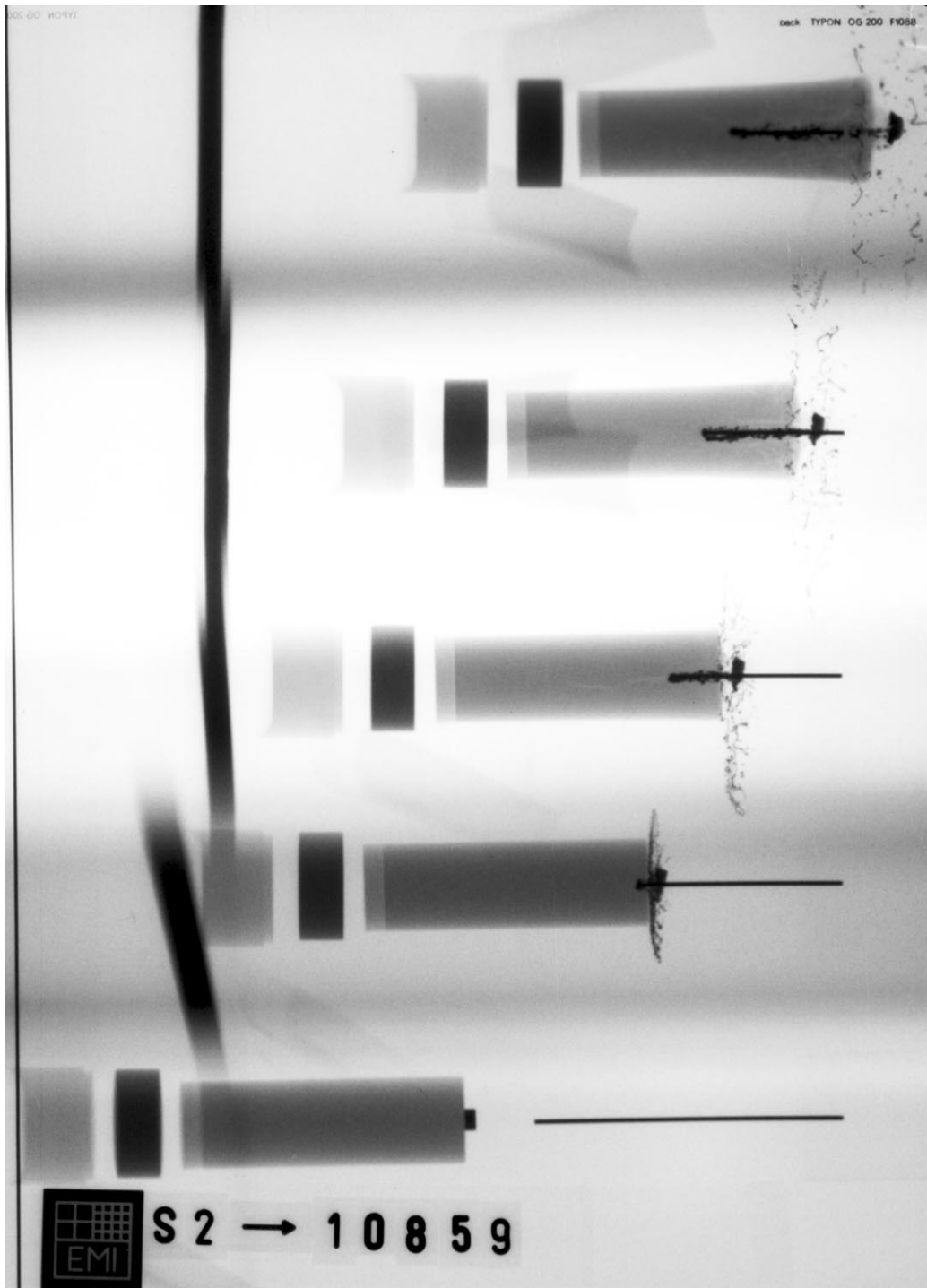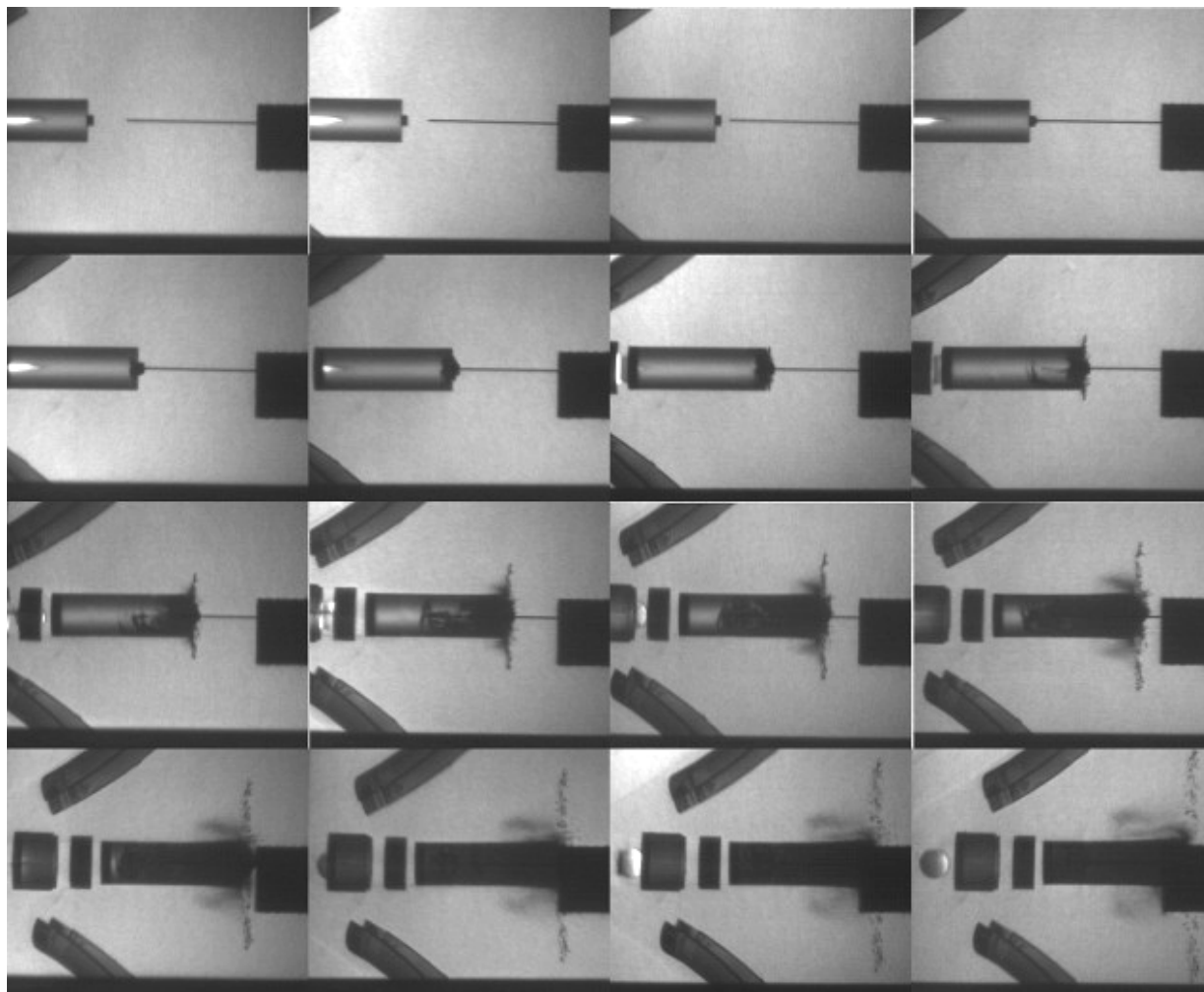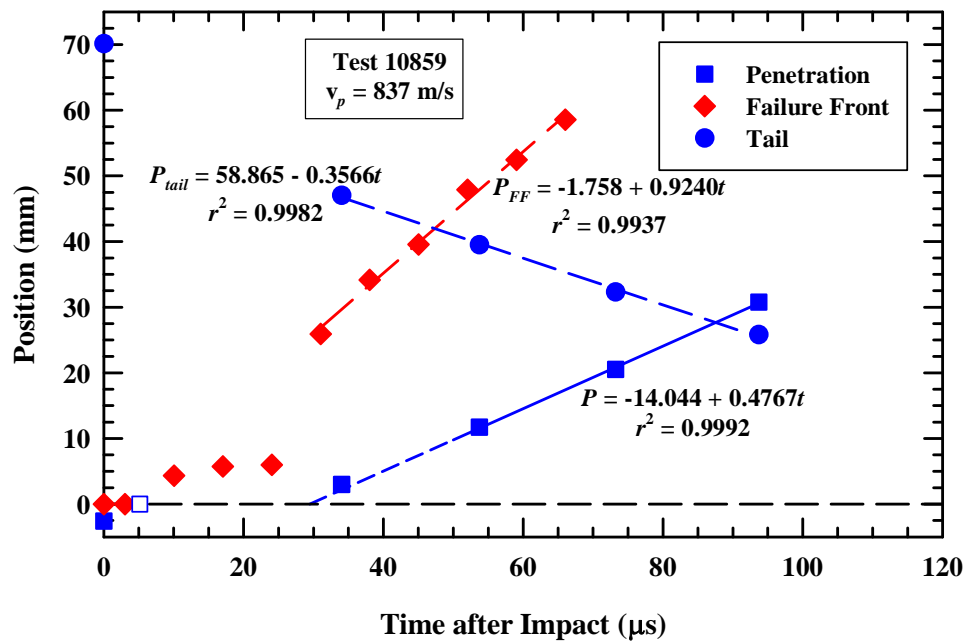**Figure A-3. Position vs. time for rod nose, tail, and failure front, Exp. 11107.**
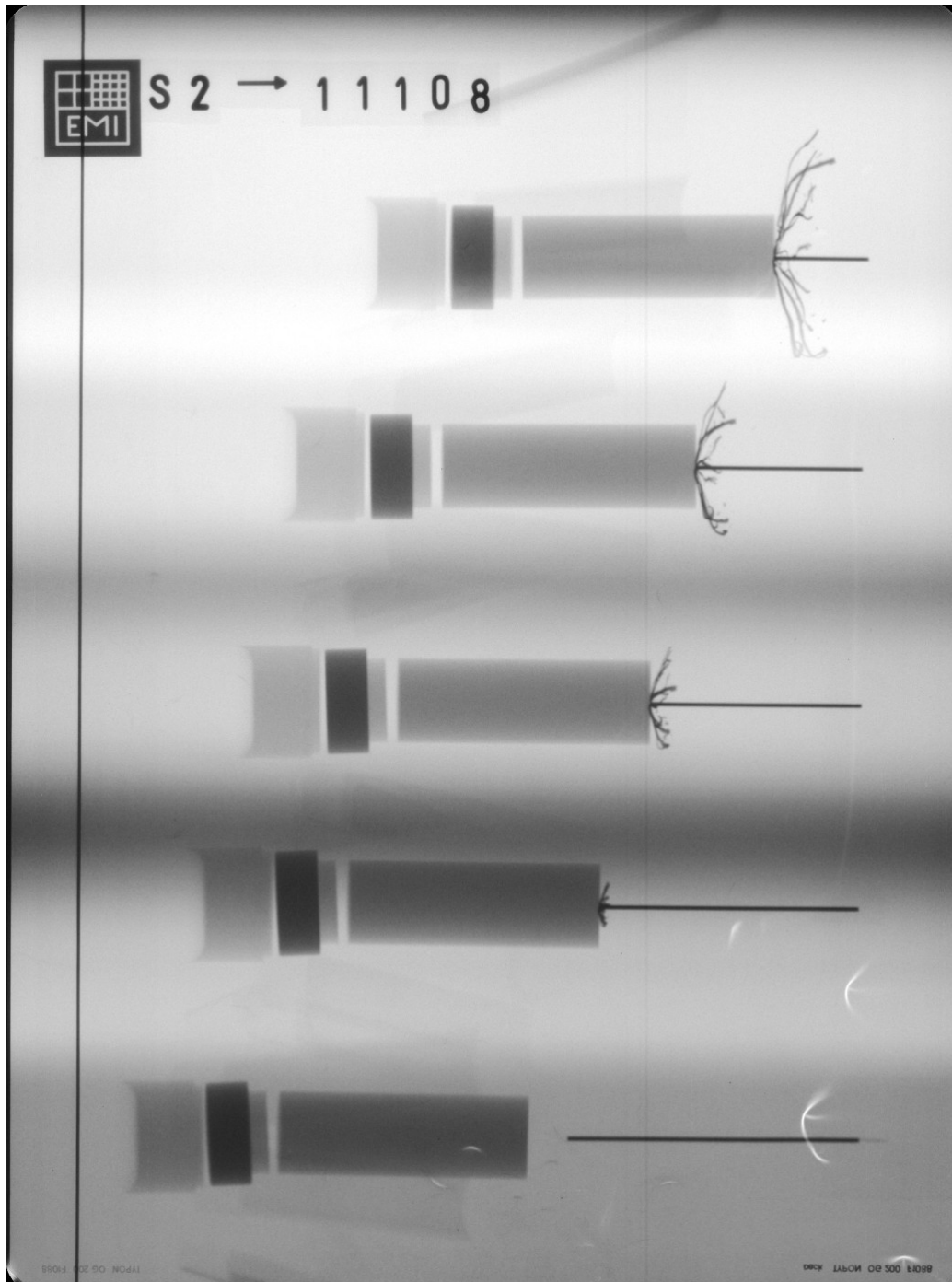
Figure A-4. X-ray picture for Exp. 11108: bare glass, v$_p$ = 441 m/s.
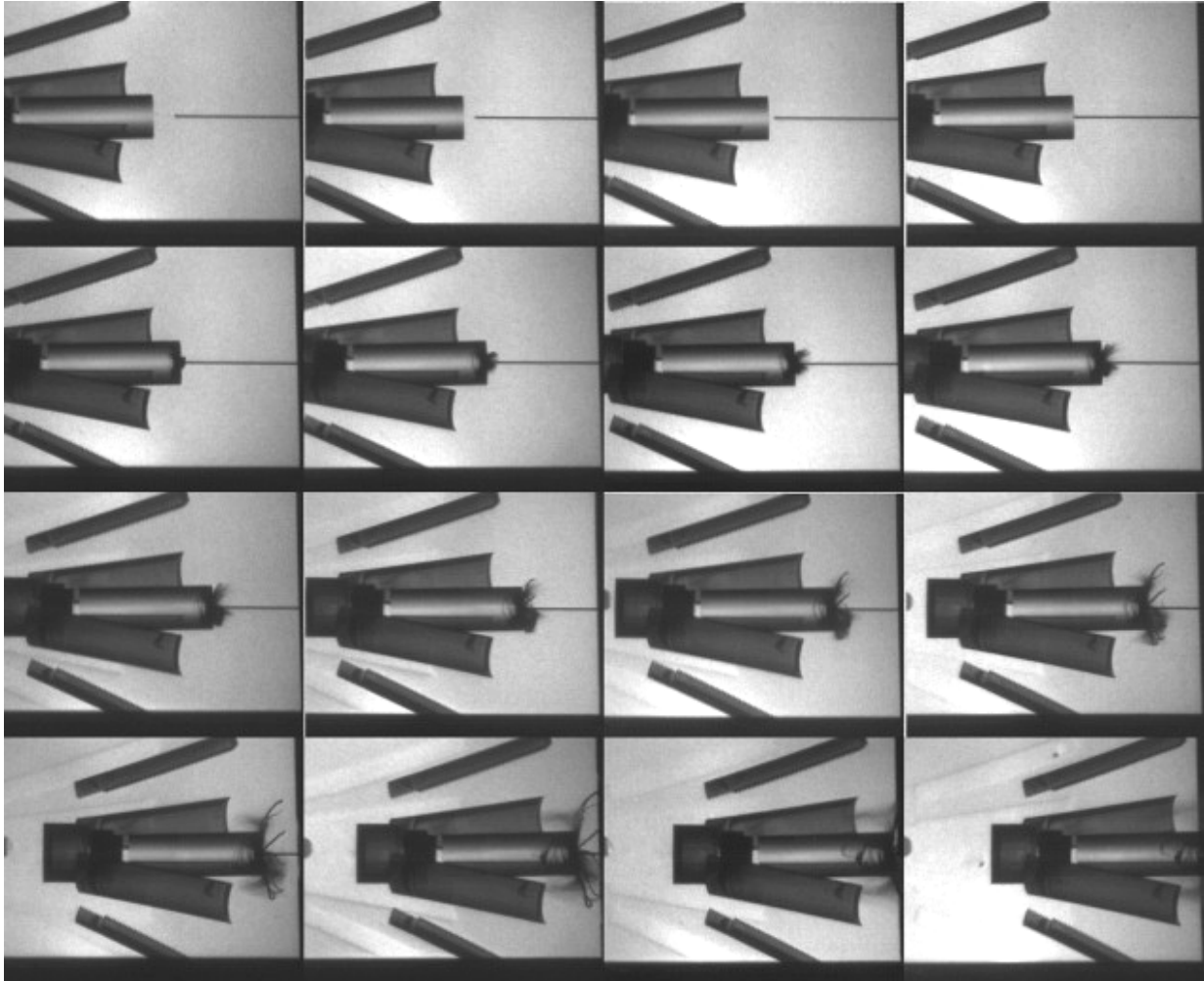
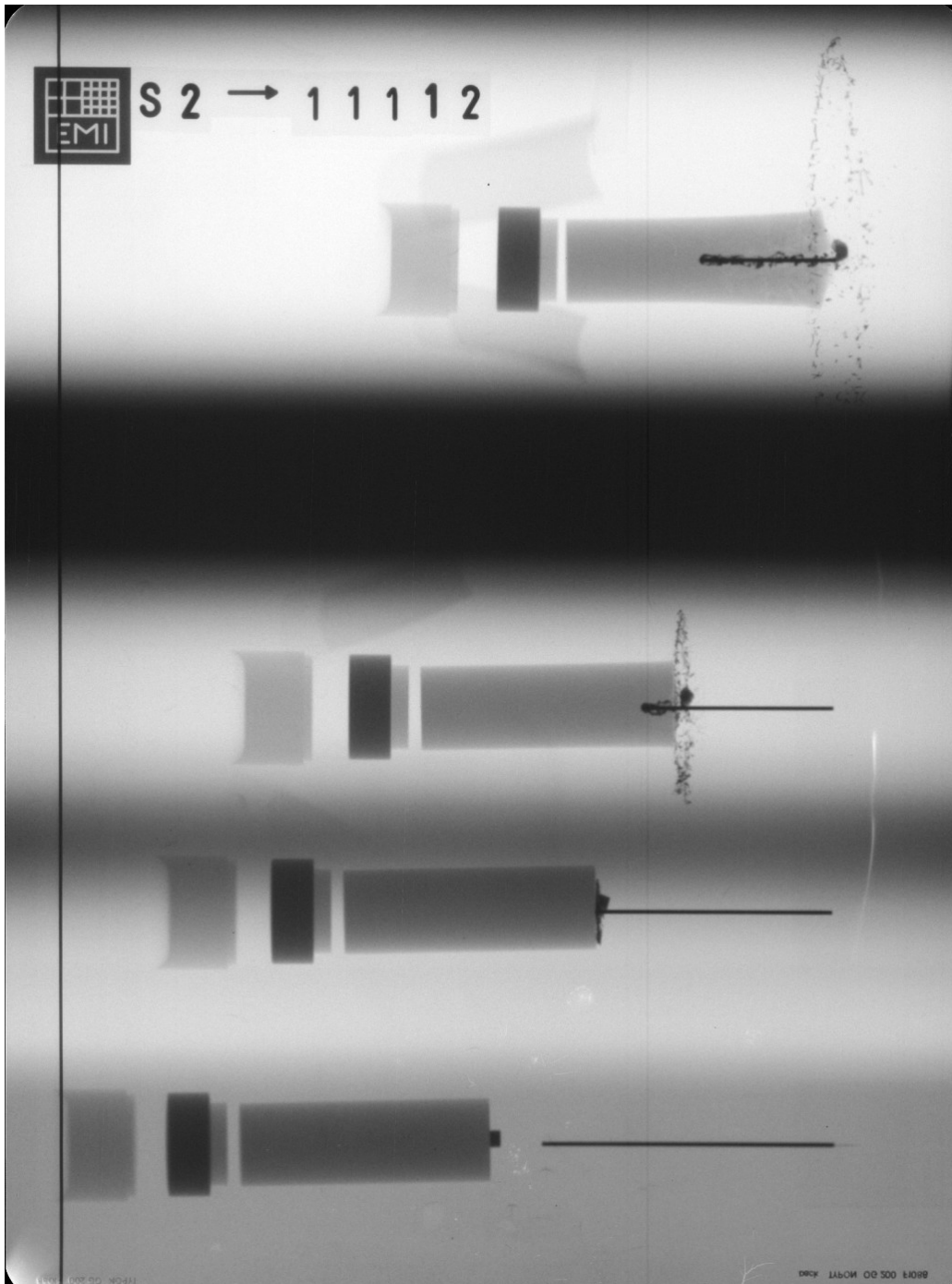**Figure A-5. Camera picture for Exp. 11108: bare glass, $v_p = 441$ m/s.**
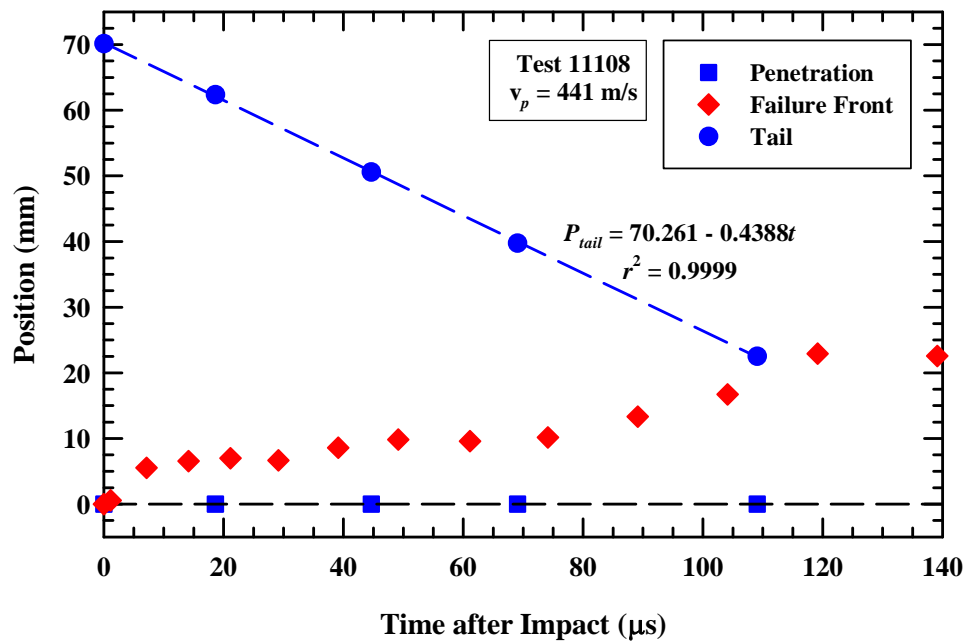
Figure A-6. Position vs. time for rod nose, tail, and failure front, Exp. 11108.
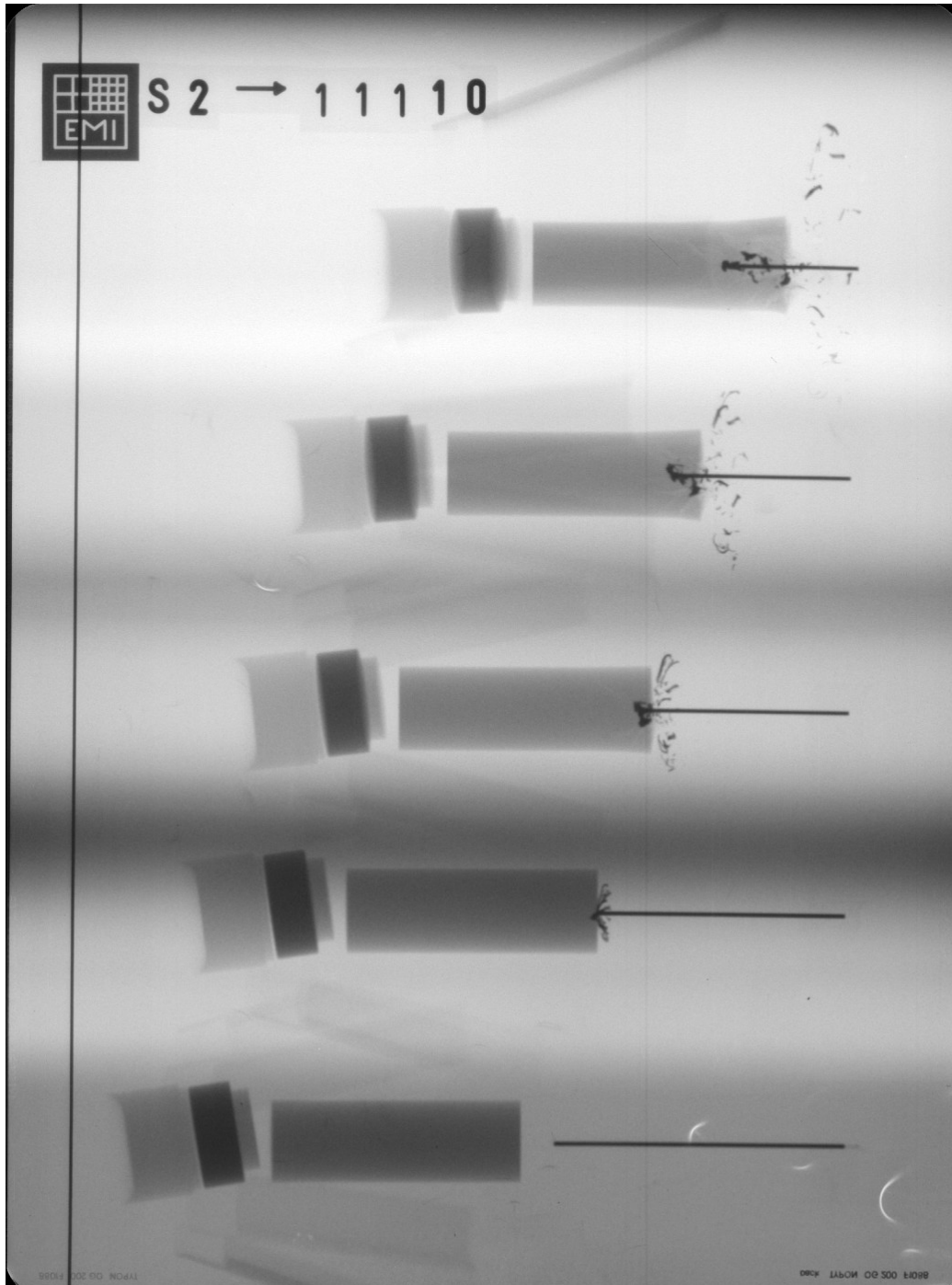
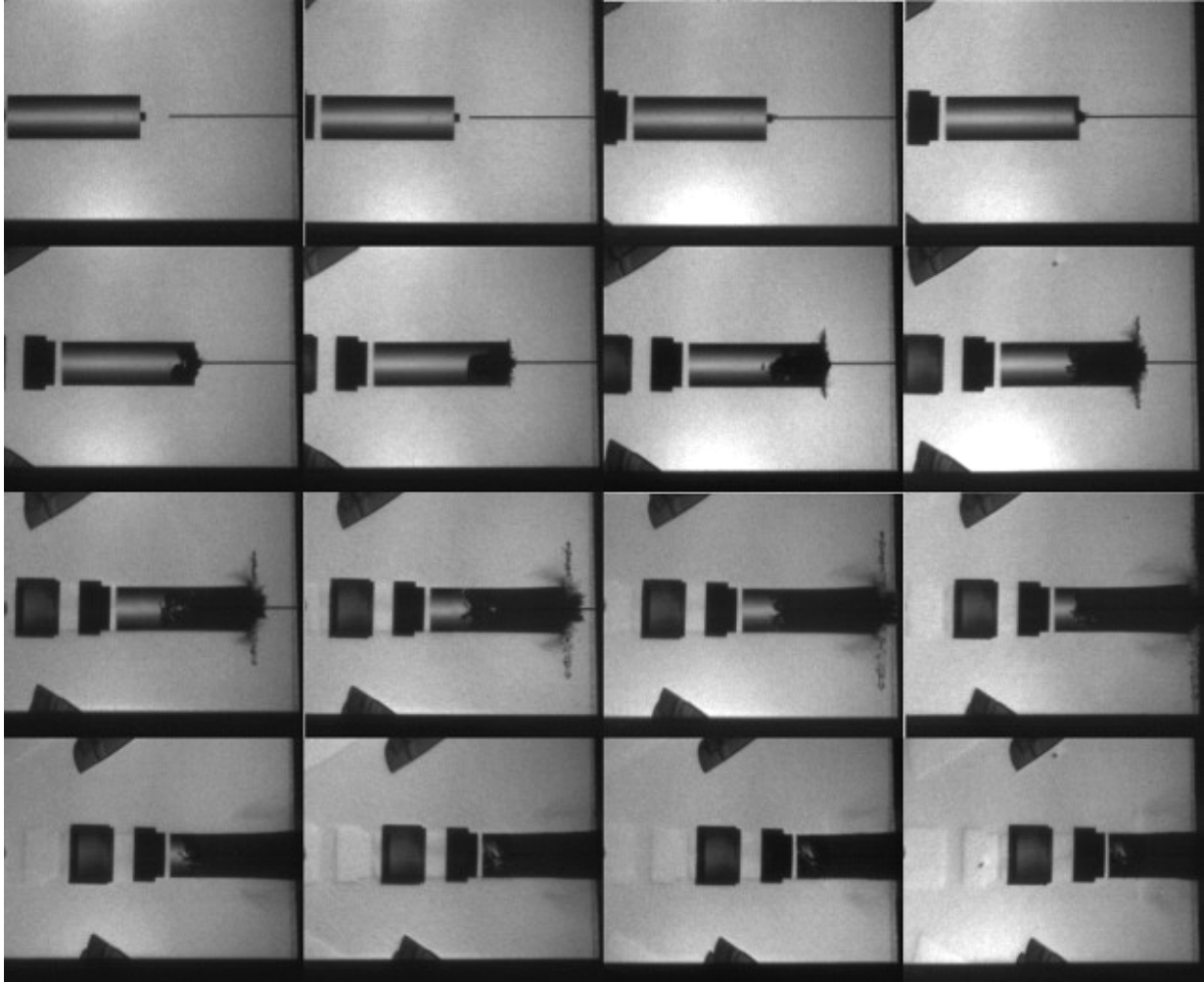**Figure A-7. X-ray picture for Exp. 11110: bare glass, v_p = 463 m/s.**
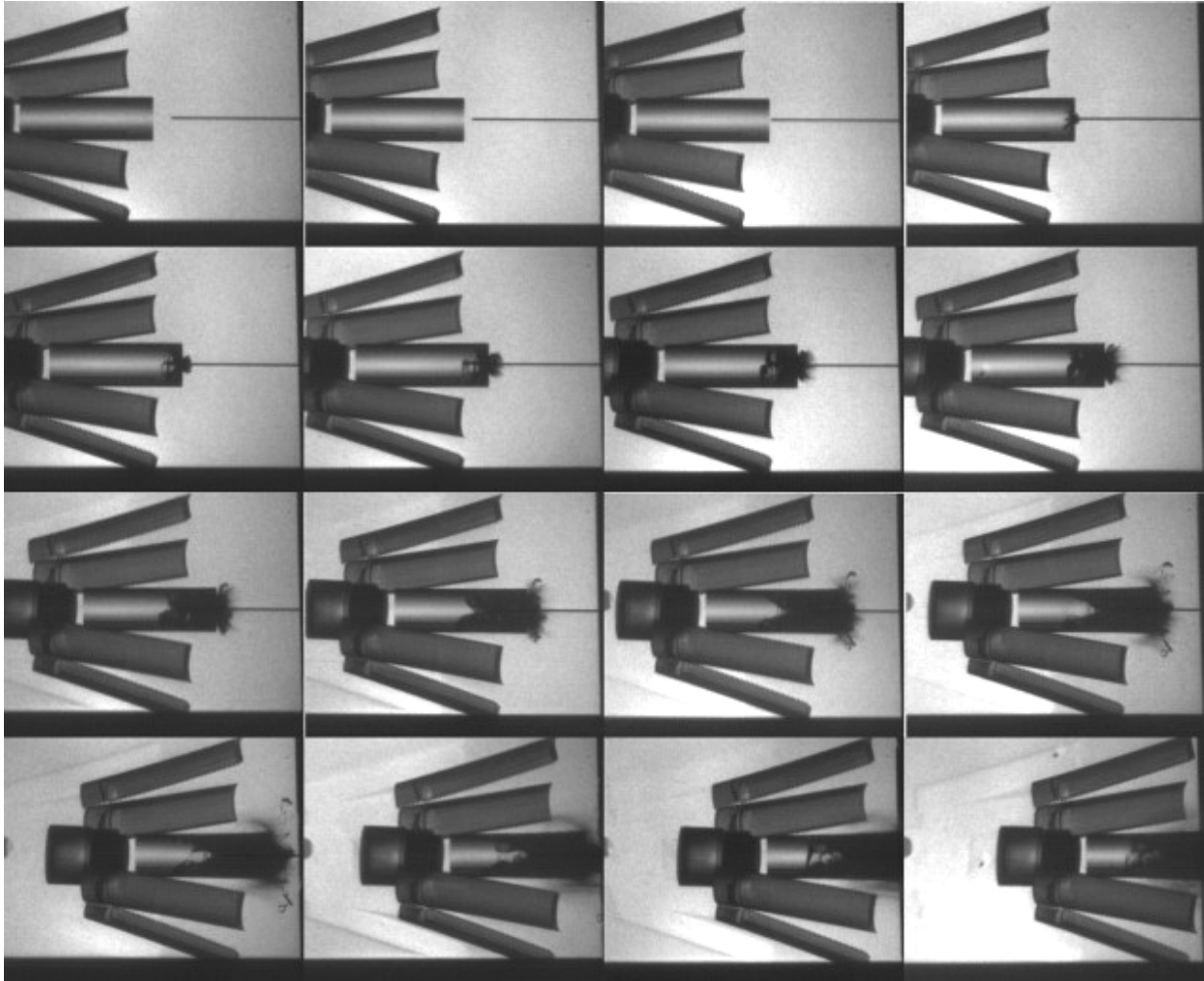
Figure A-8. Camera picture for Exp. 11110: bare glass, v_p = 463 m/s.
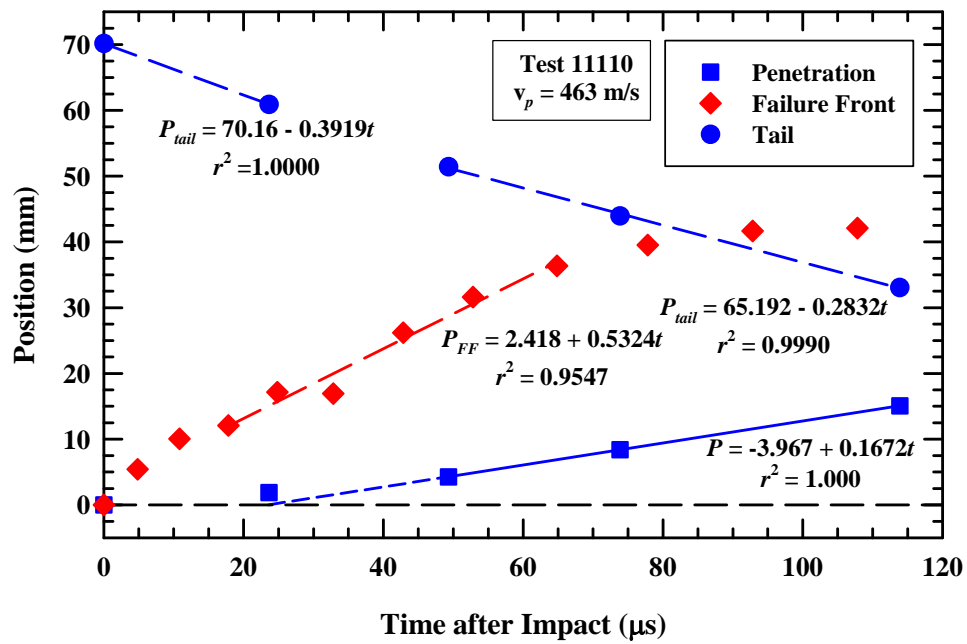
Figure A-9. Position vs. time for rod nose, tail, and failure front, Exp. 11110.
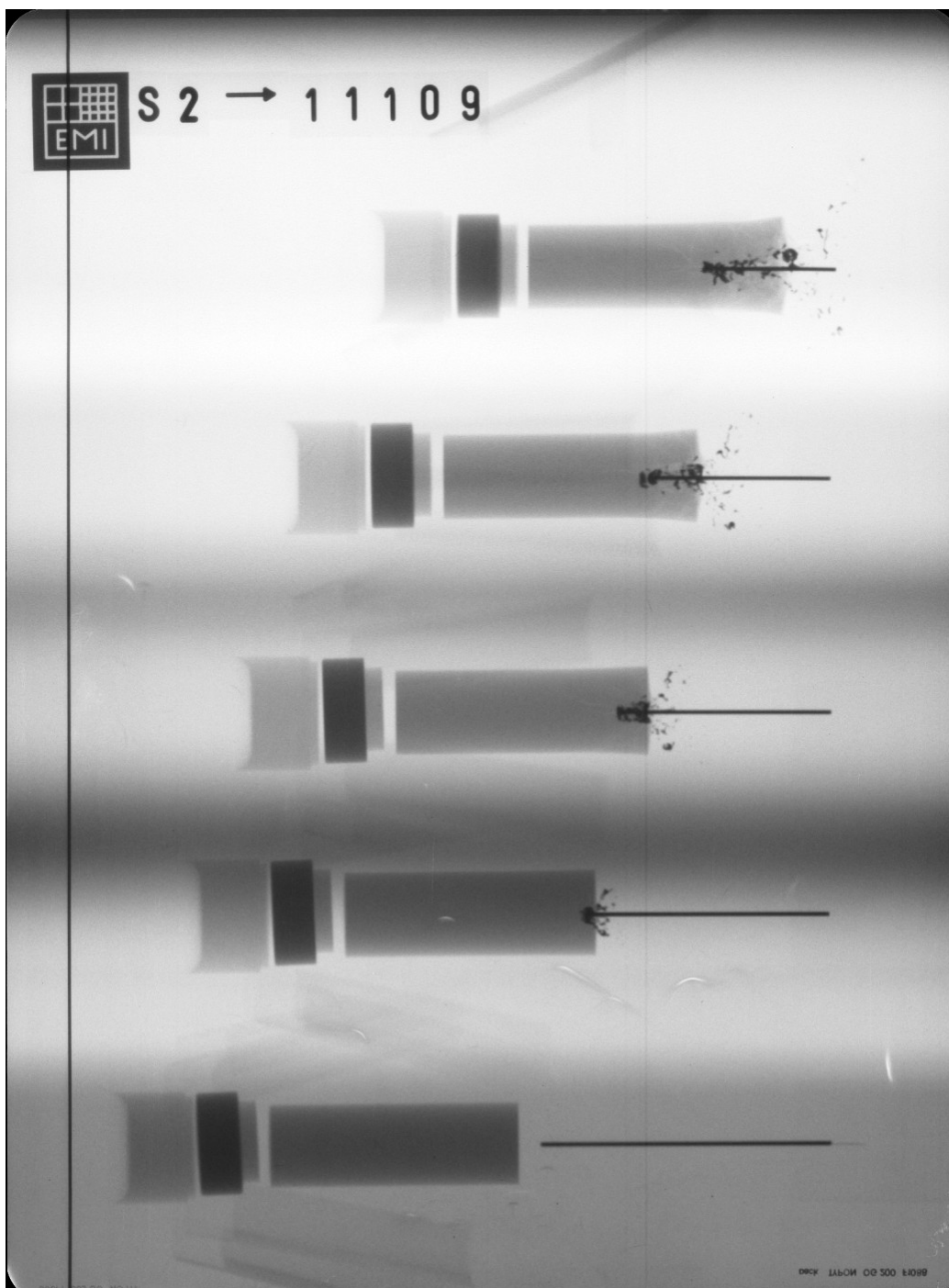
Figure A-10. X-ray picture for Exp. 11109: bare glass, $v_p = 475$ m/s.
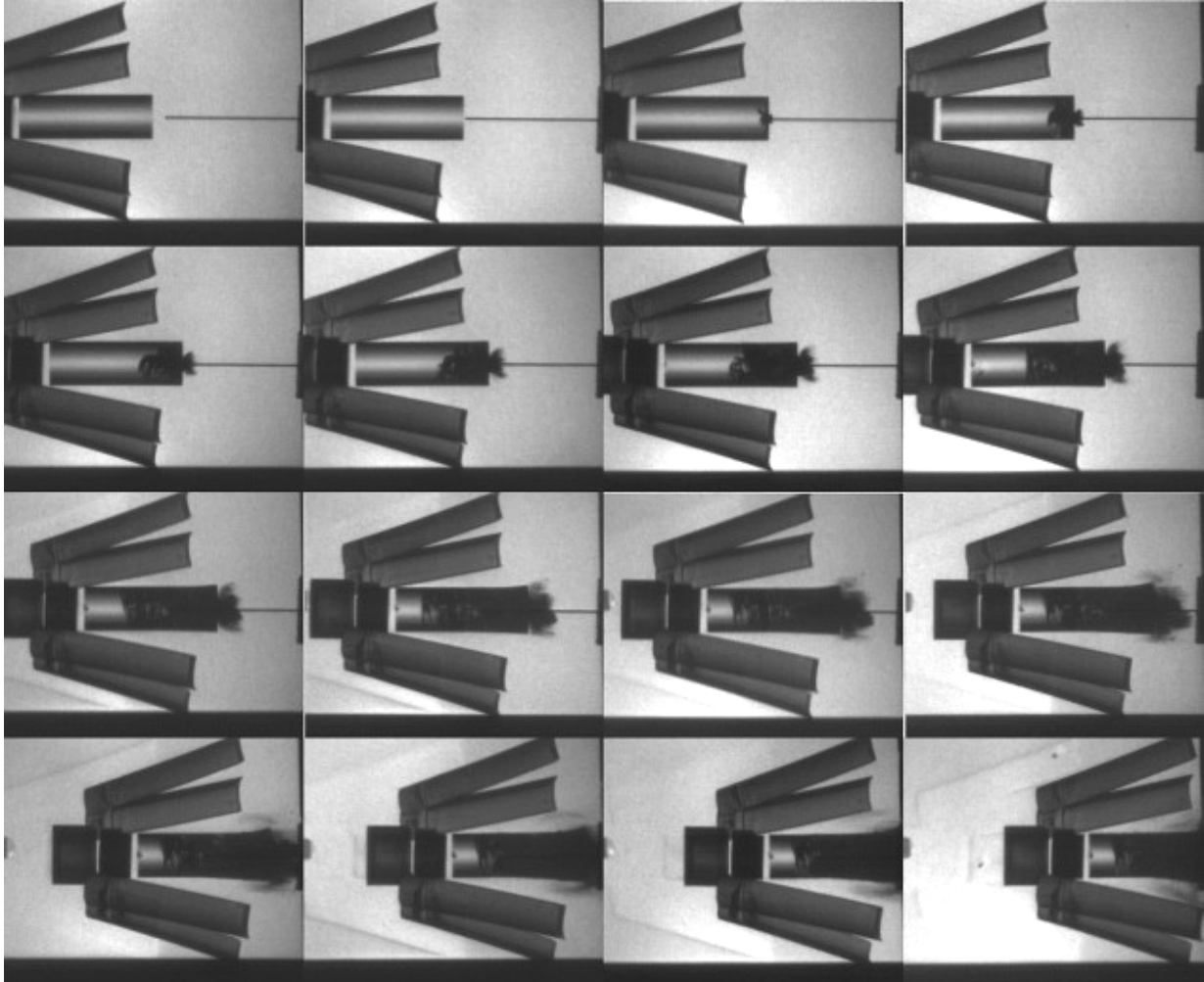
Figure A-11. Camera picture for Exp. 11109: bare glass, v_p = 475 m/s.
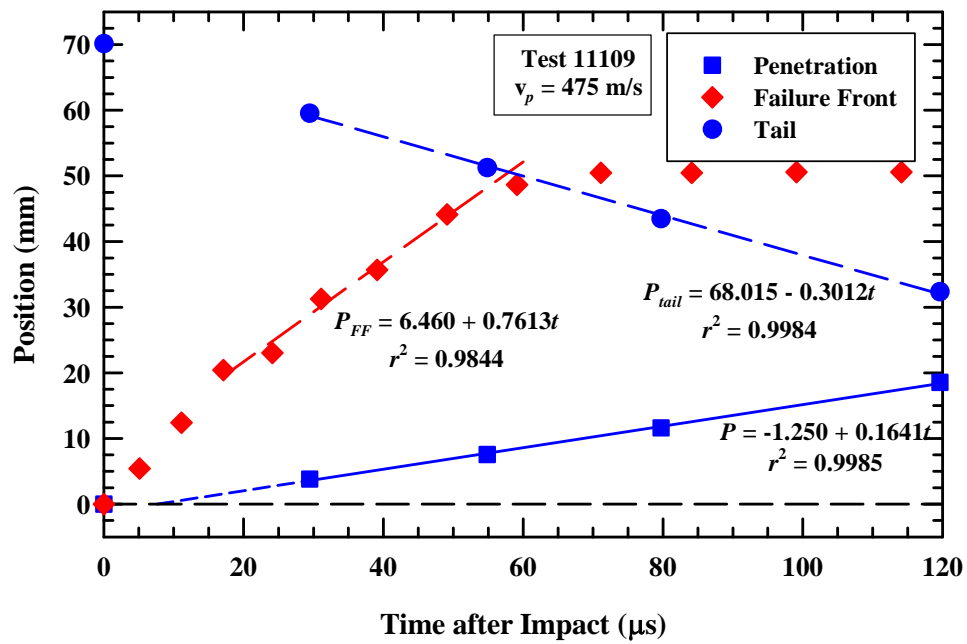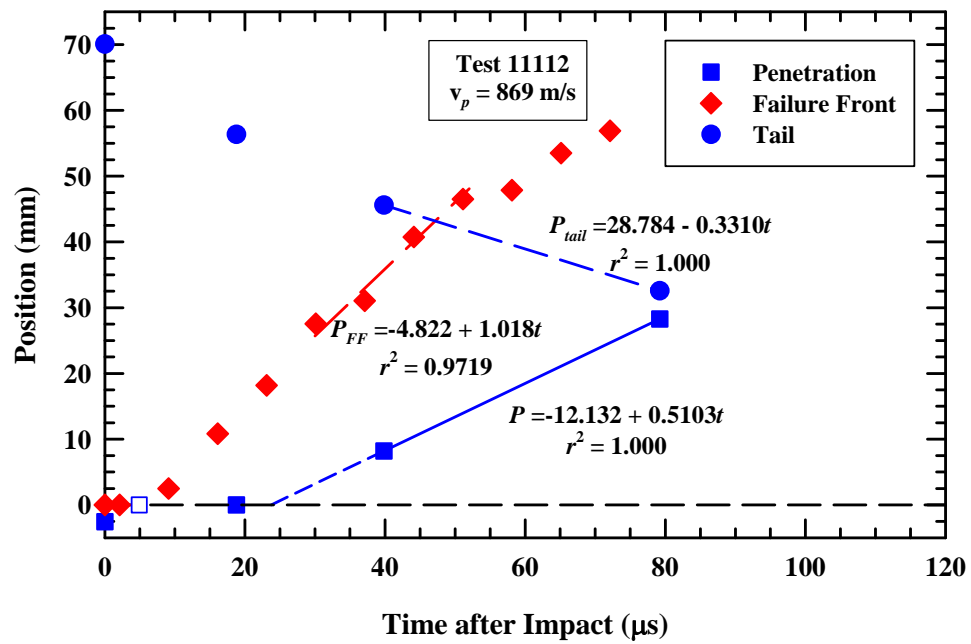
Figure A-12. Position vs. time for rod nose, tail, and failure front, Exp. 11109.

Figure A-13. X-ray picture for Exp. 10850: buffered glass, $v_p = 583$ m/s.
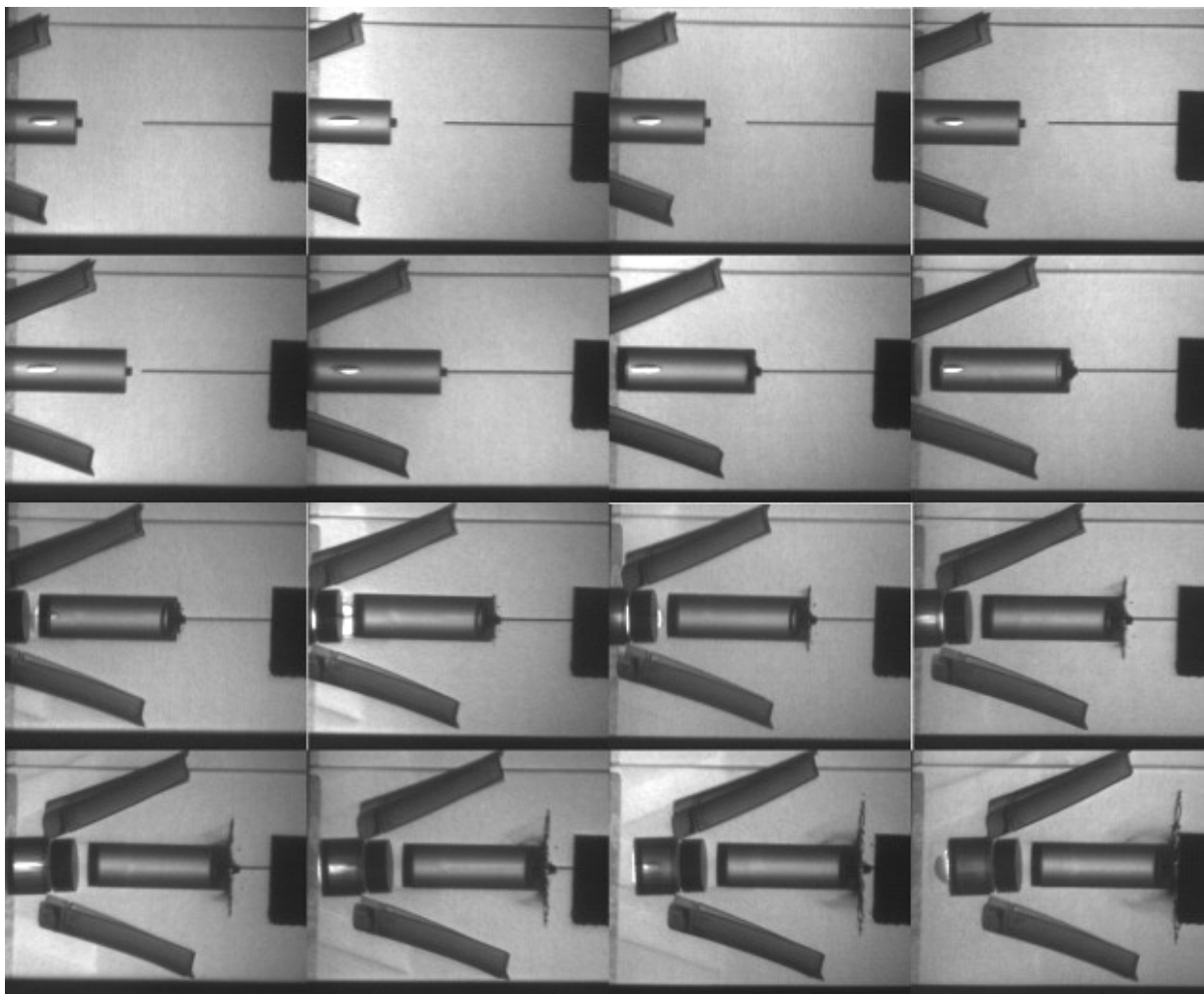
Figure A-14. Camera picture for Exp. 10850: buffered glass, $v_p = 583$ m/s.
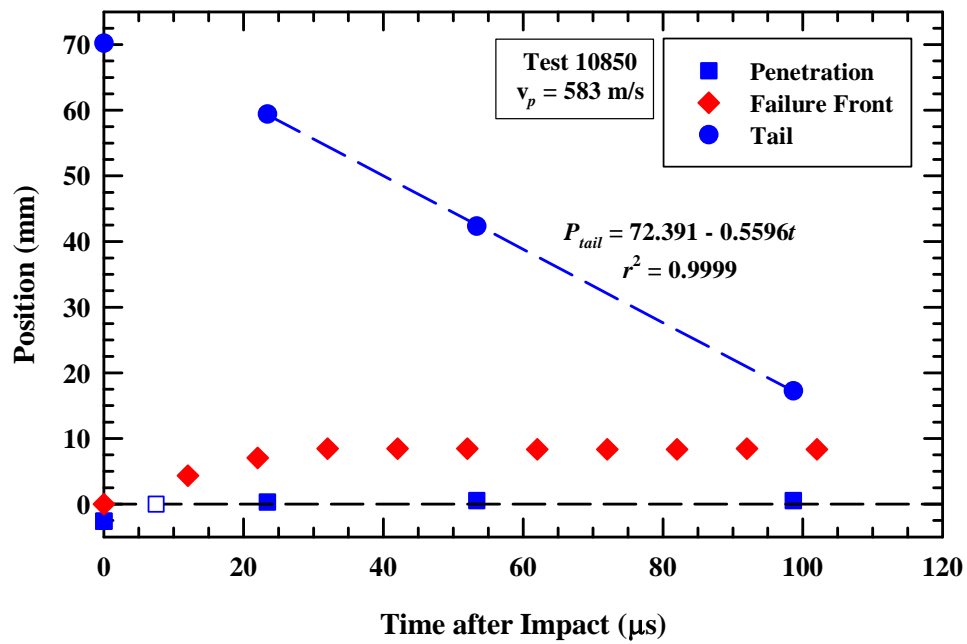
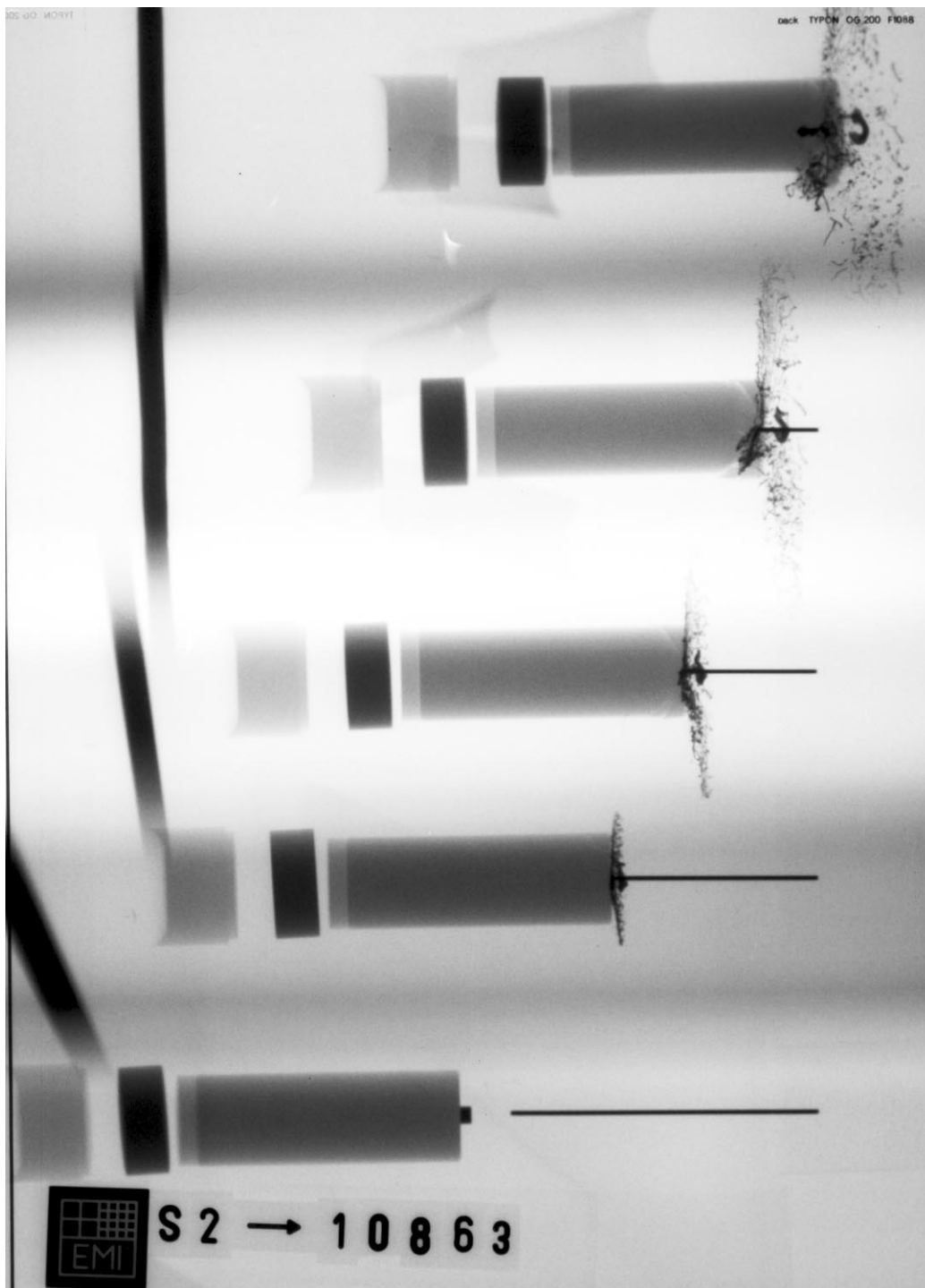**Figure A-15. Position vs. time for rod nose, tail, and failure front, Exp. 10850.**
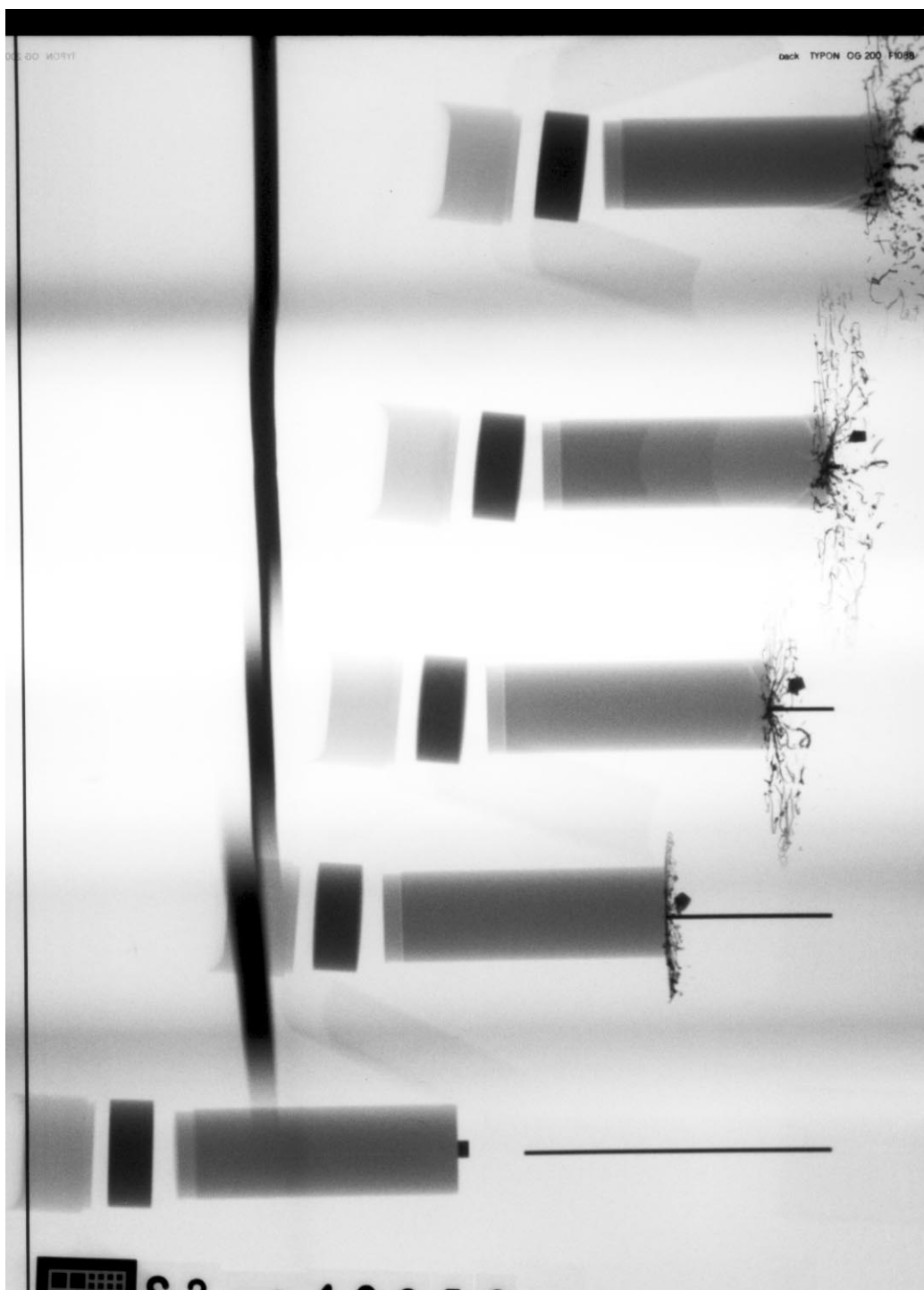
Figure A-16. X-ray picture for Exp. 10853: buffered glass, $v_p = 649$ m/s.
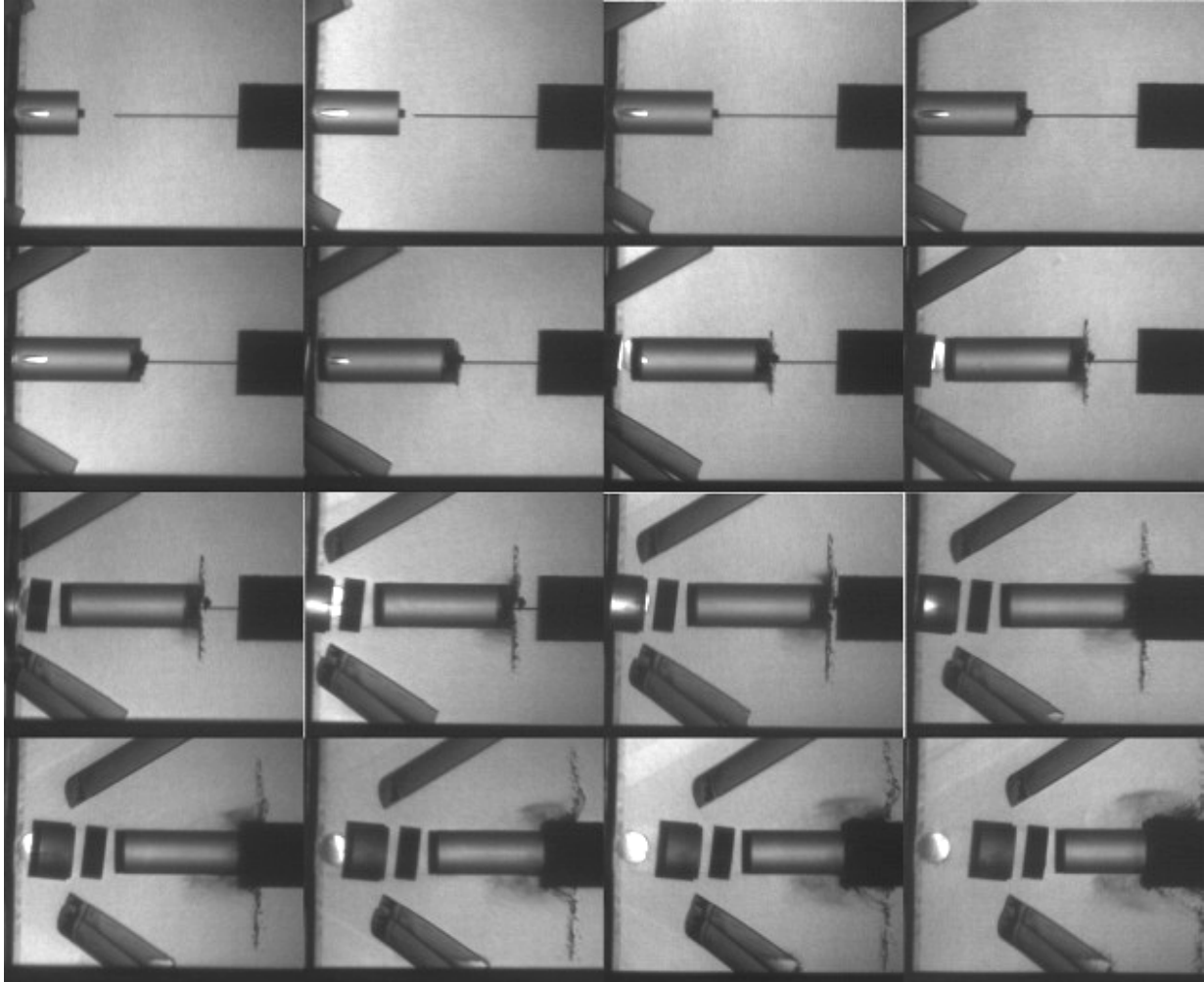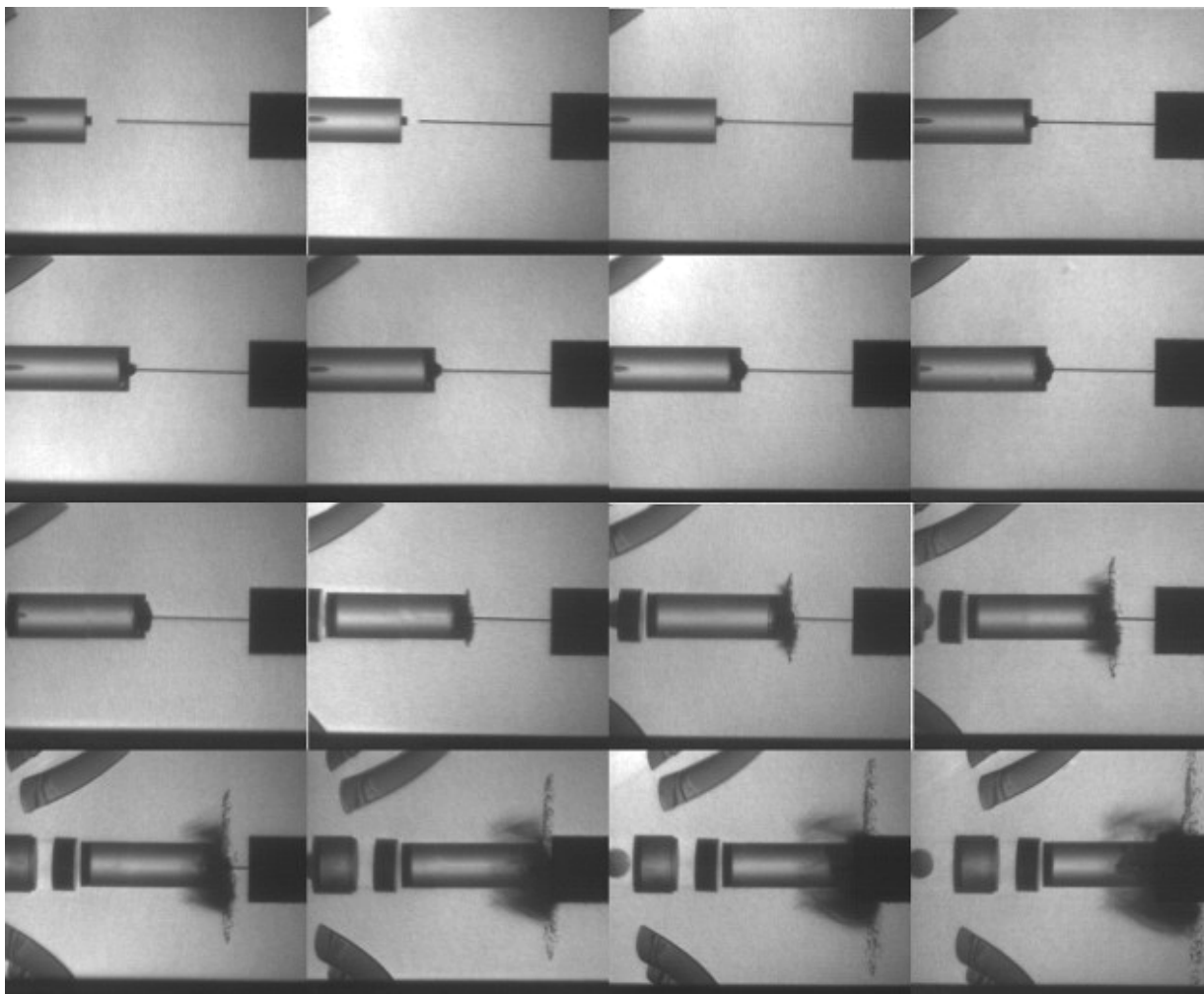
Figure A-17. Camera picture for Exp. 10853: buffered glass, v_p = 649 m/s.
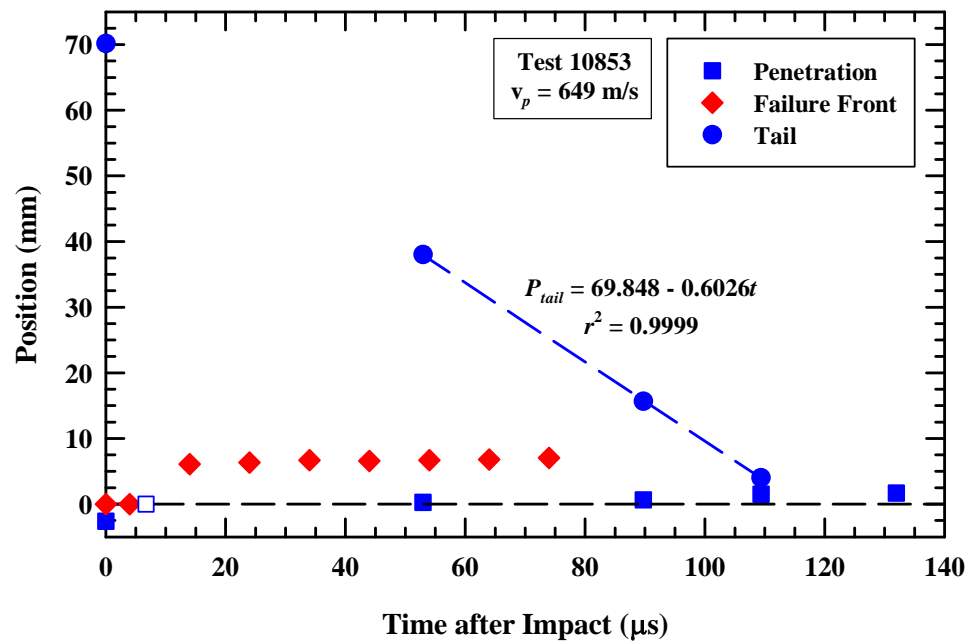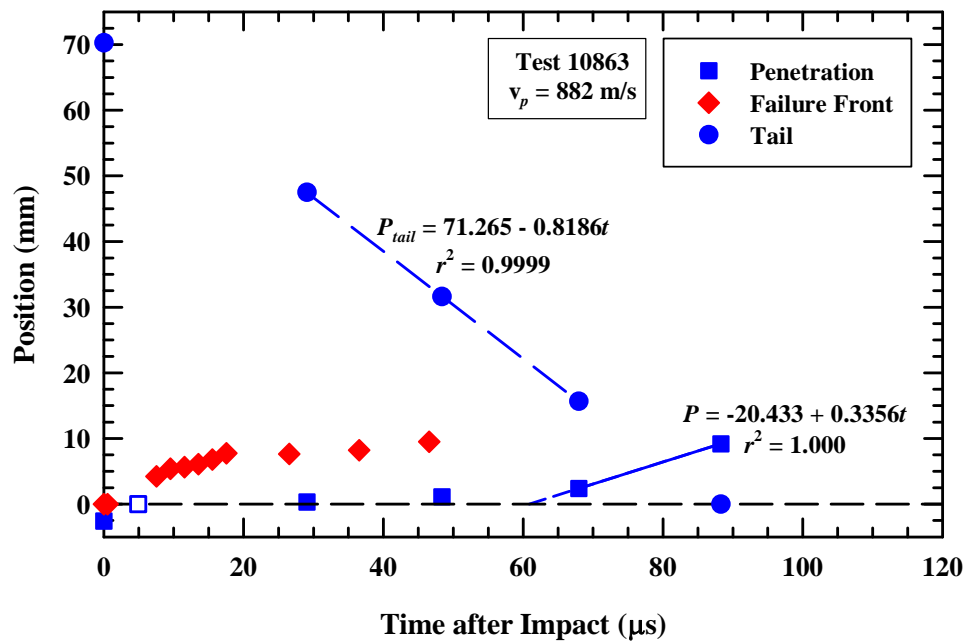
Figure A-18. Position vs. time for rod nose, tail, and failure front, Exp. 10853.
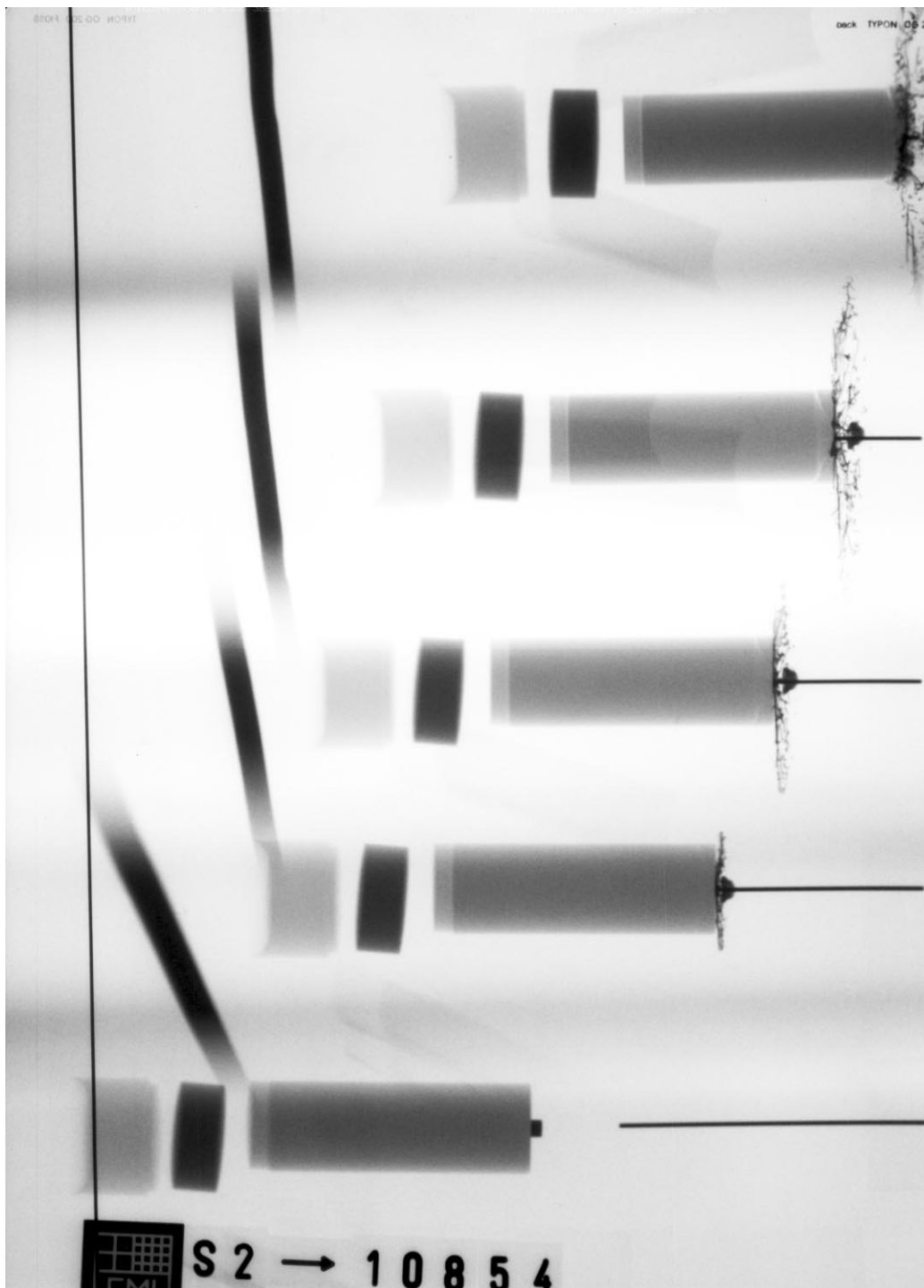
Figure A-19. X-ray picture for Exp. 10854: buffered glass, $v_p = 720$ m/s.
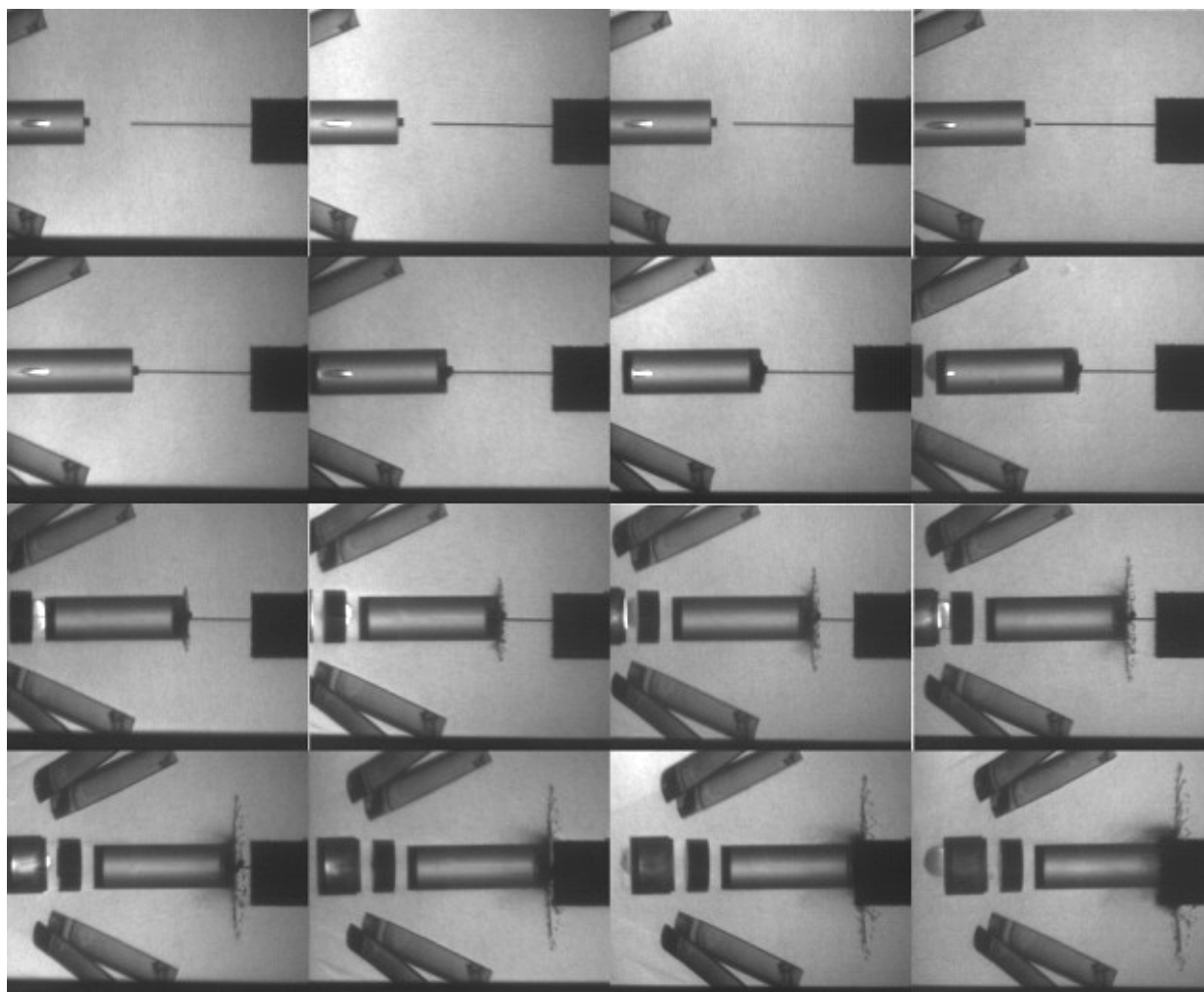
Figure A-20. Camera picture for Exp. 10854: buffered glass, $v_p = 720$ m/s.
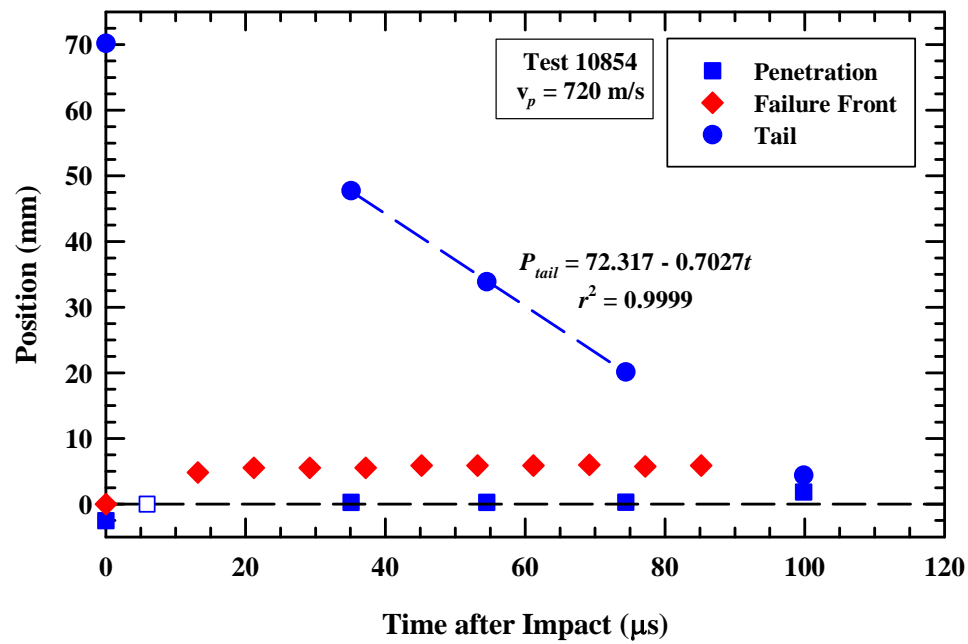
Figure A-21. Position vs. time for rod nose, tail, and failure front, Exp. 10854.
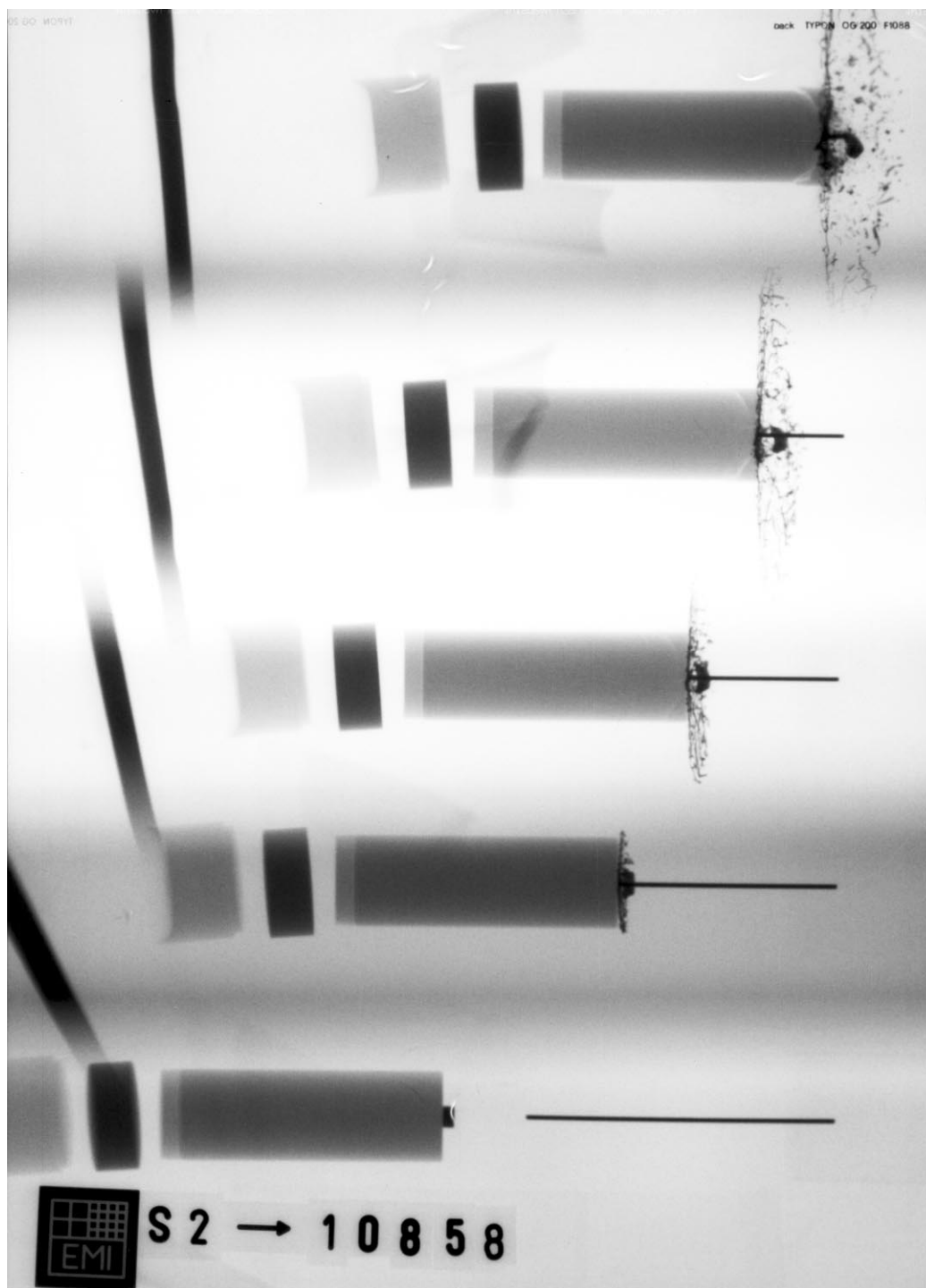
Figure A-22. X-ray picture for Exp. 10858: buffered glass, v$_p$ = 782 m/s.
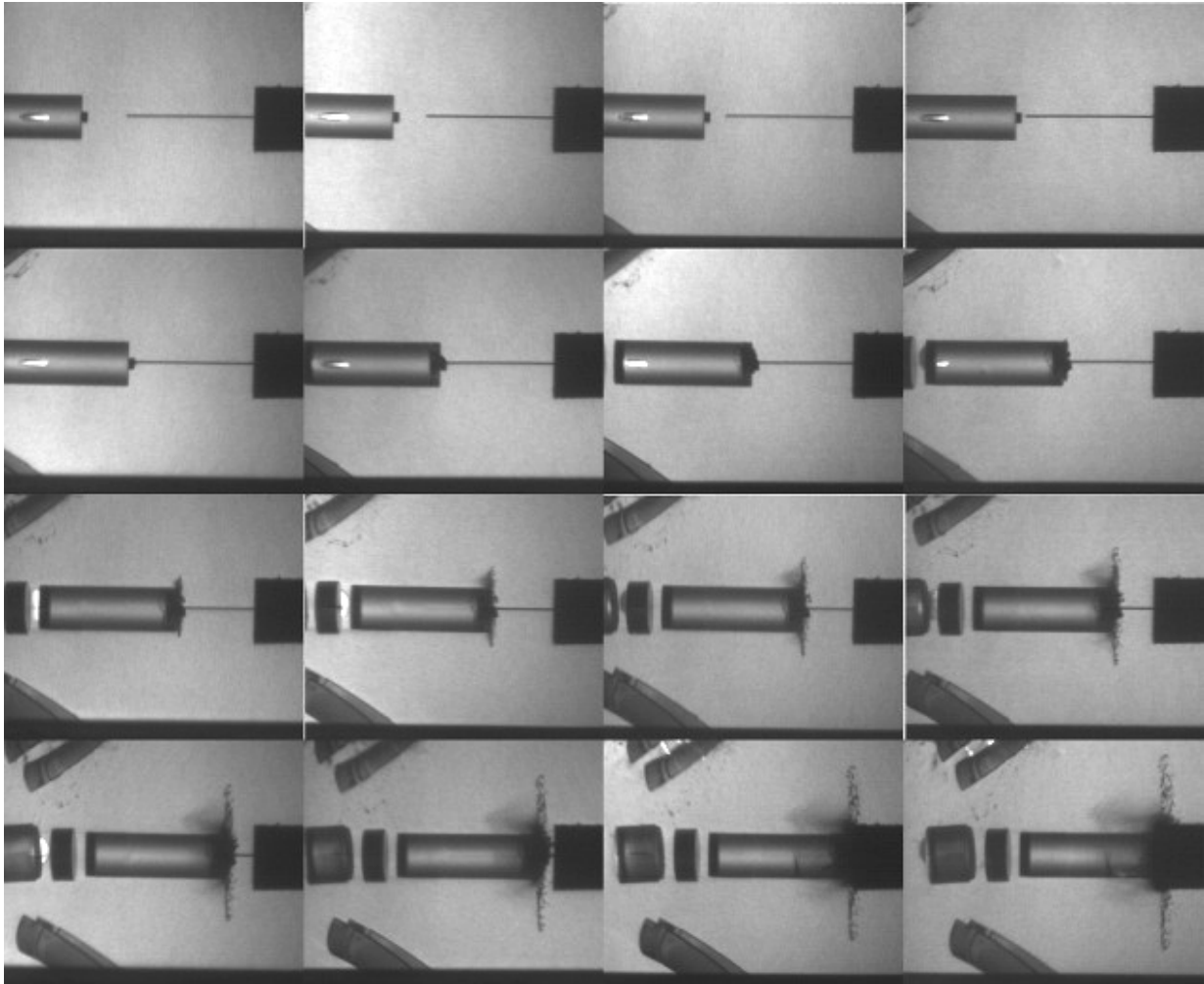
Figure A-23. Camera picture for Exp. 10858: buffered glass, v_p = 782 m/s.
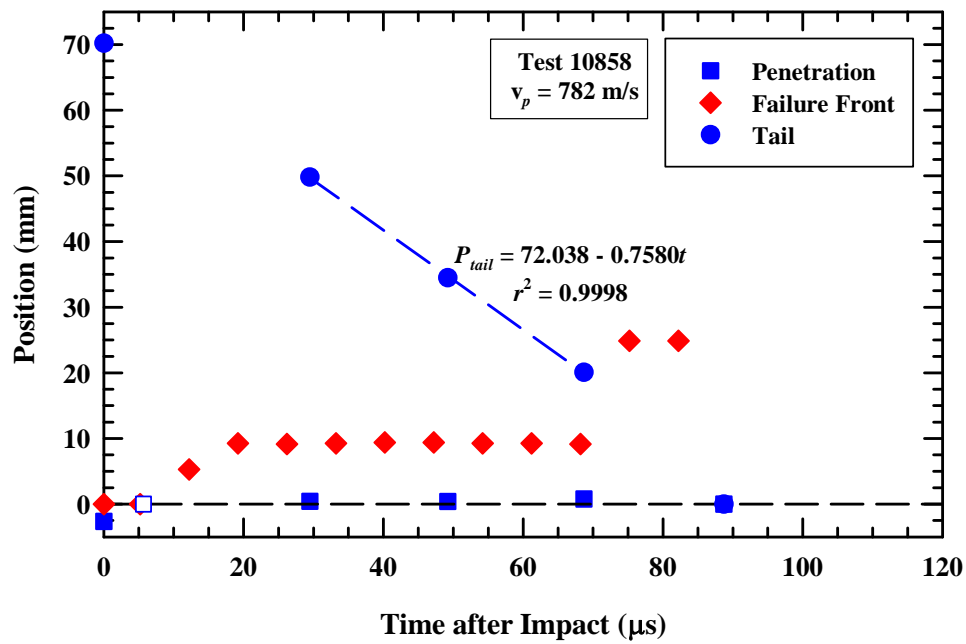
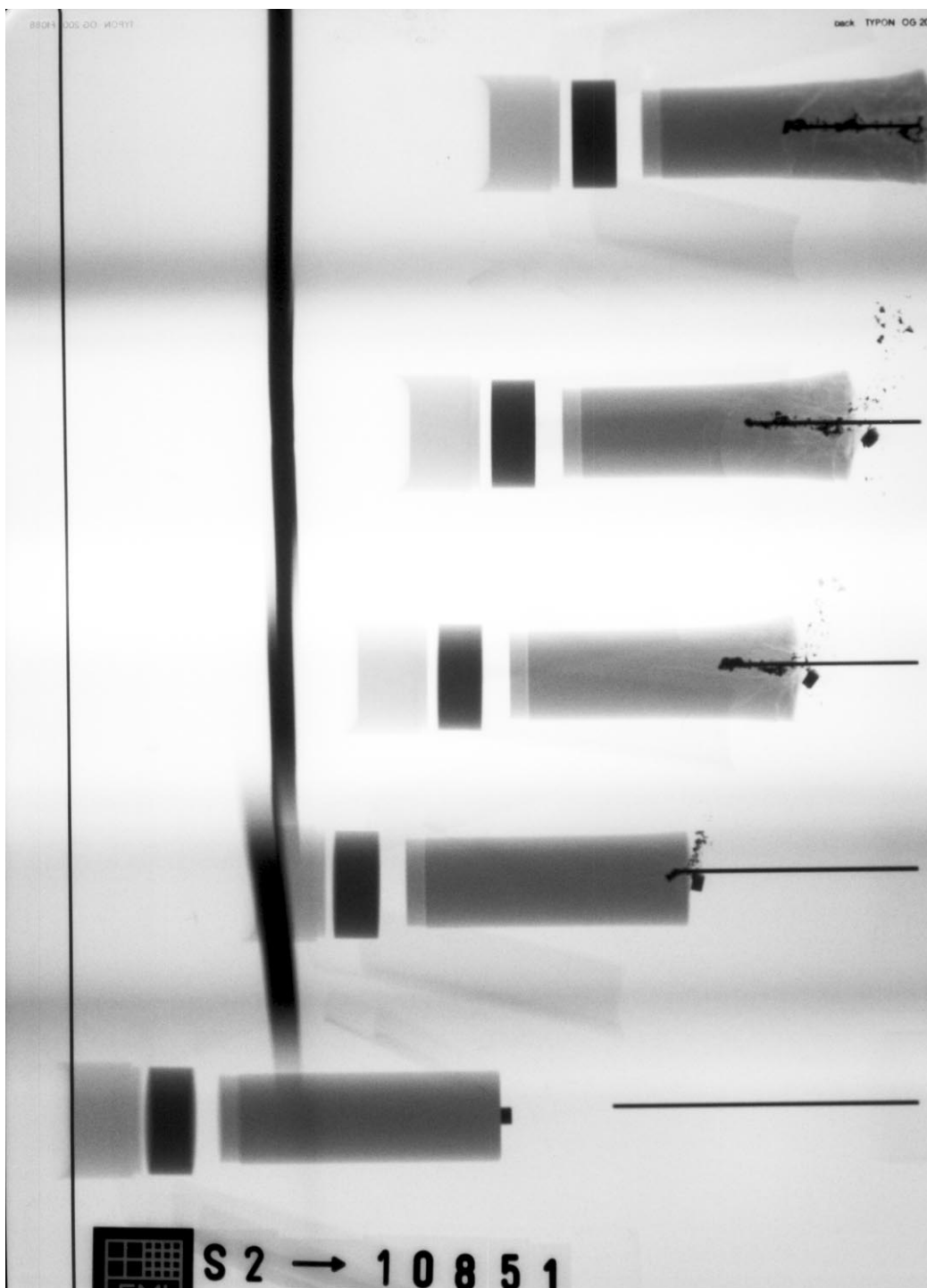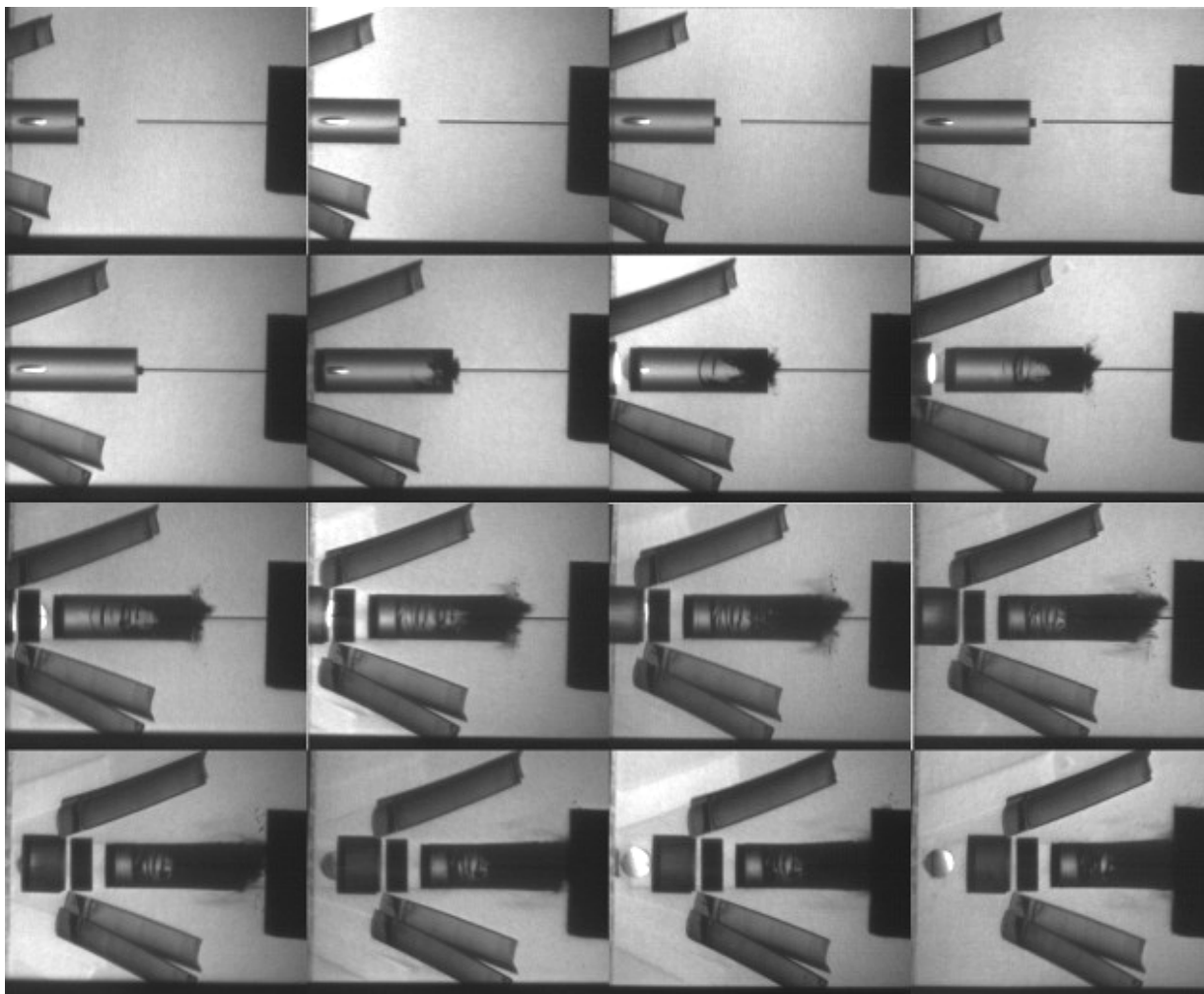**Figure A-24. Position vs. time for rod nose, tail, and failure front, Exp. 10858.**
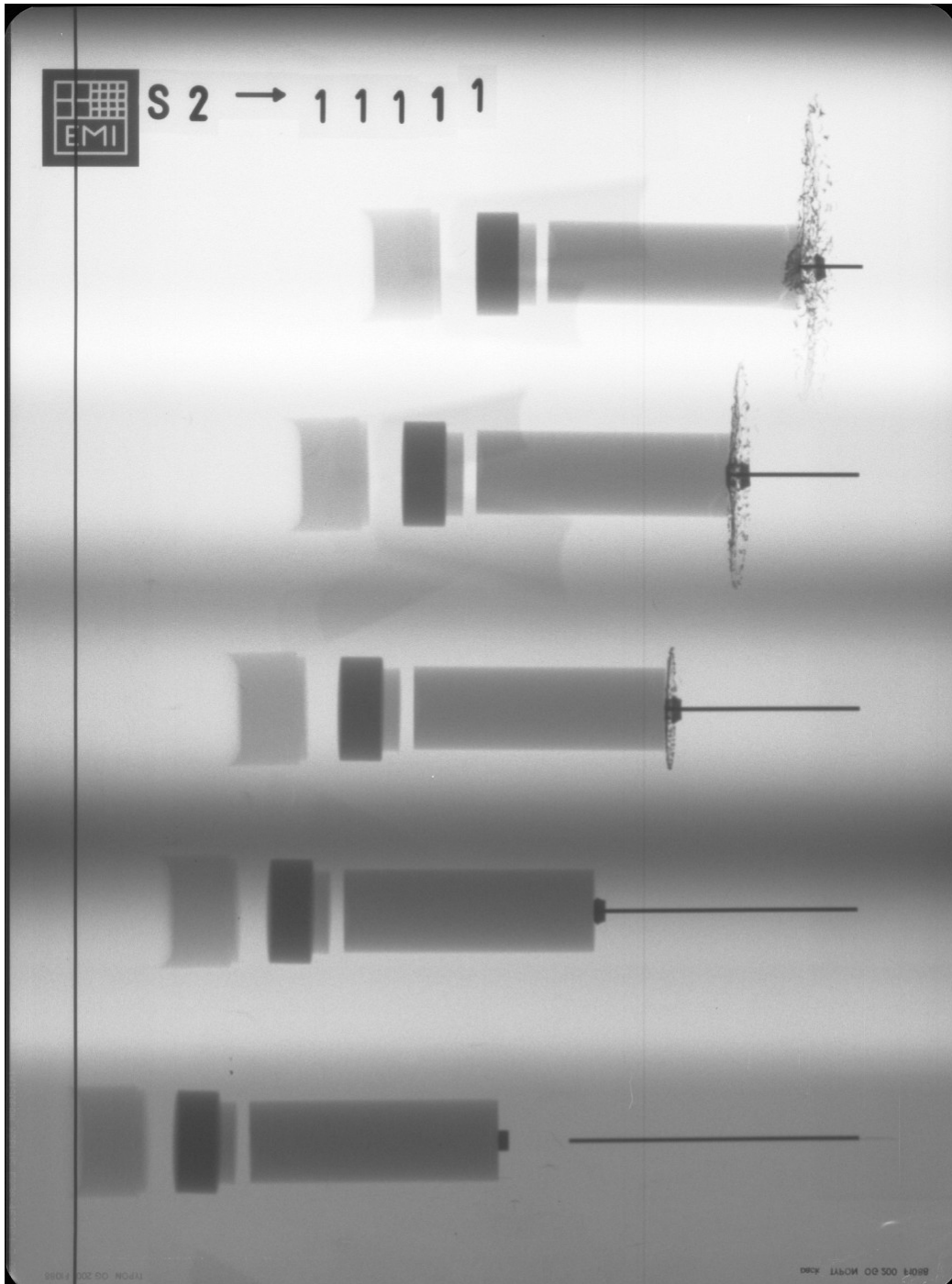
Figure A-25. X-ray picture for Exp. 11111: buffered glass, v_p = 800 m/s.
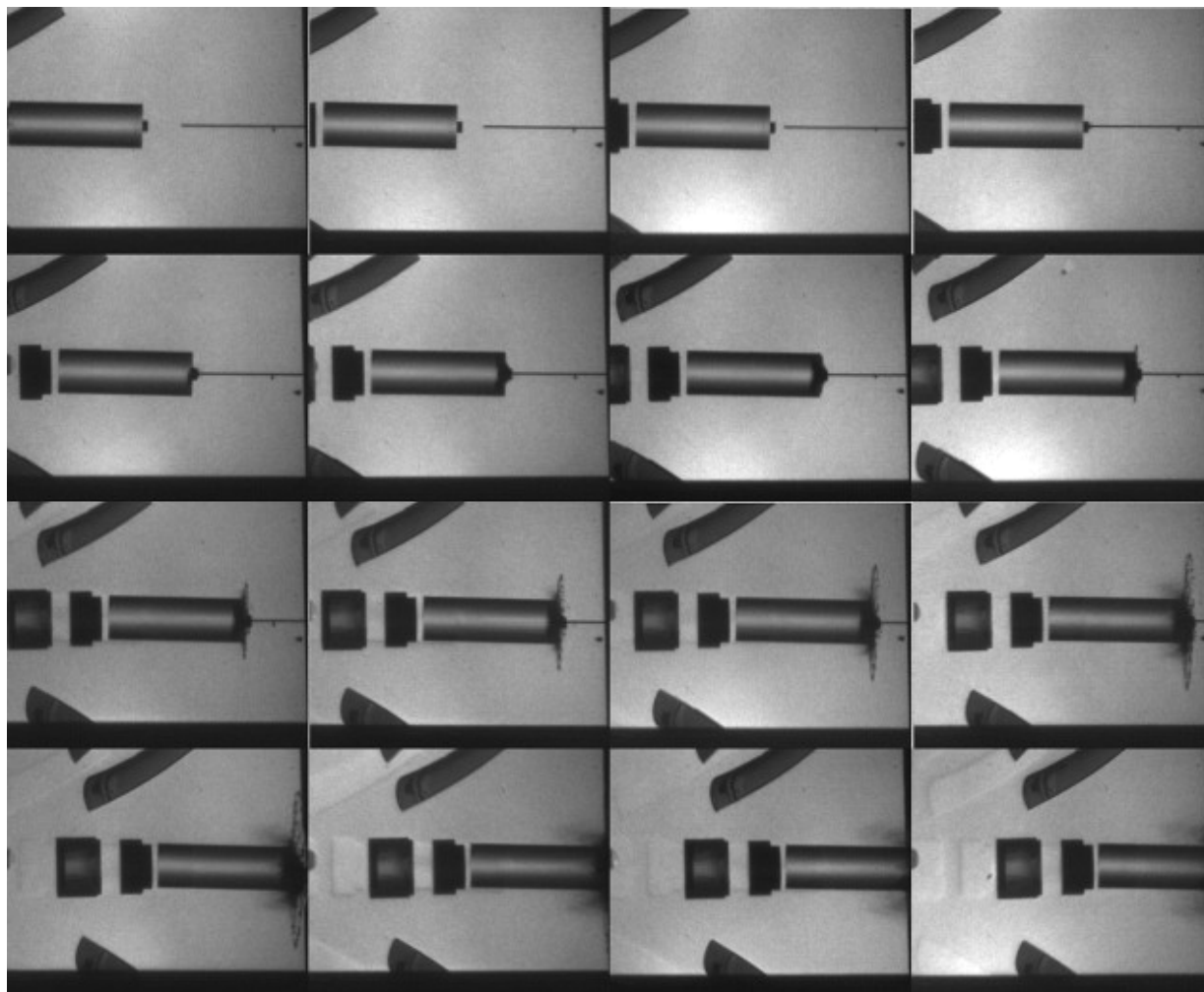
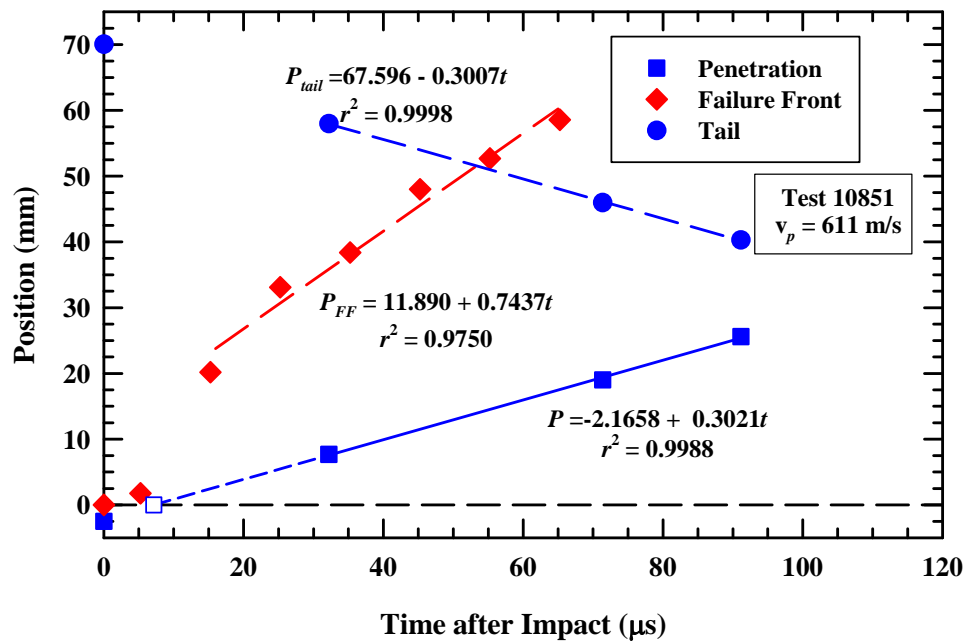**Figure A-26. Camera picture for Exp. 11111: buffered glass, $v_p = 800$ m/s.**
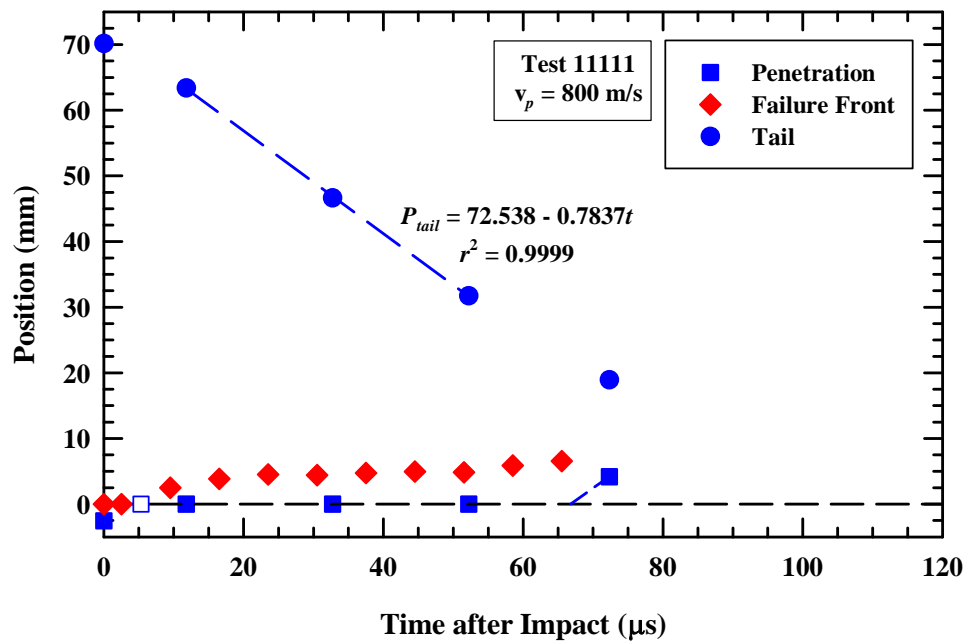
Figure A-27. Position vs. time for rod nose, tail, and failure front, Exp. 11111.
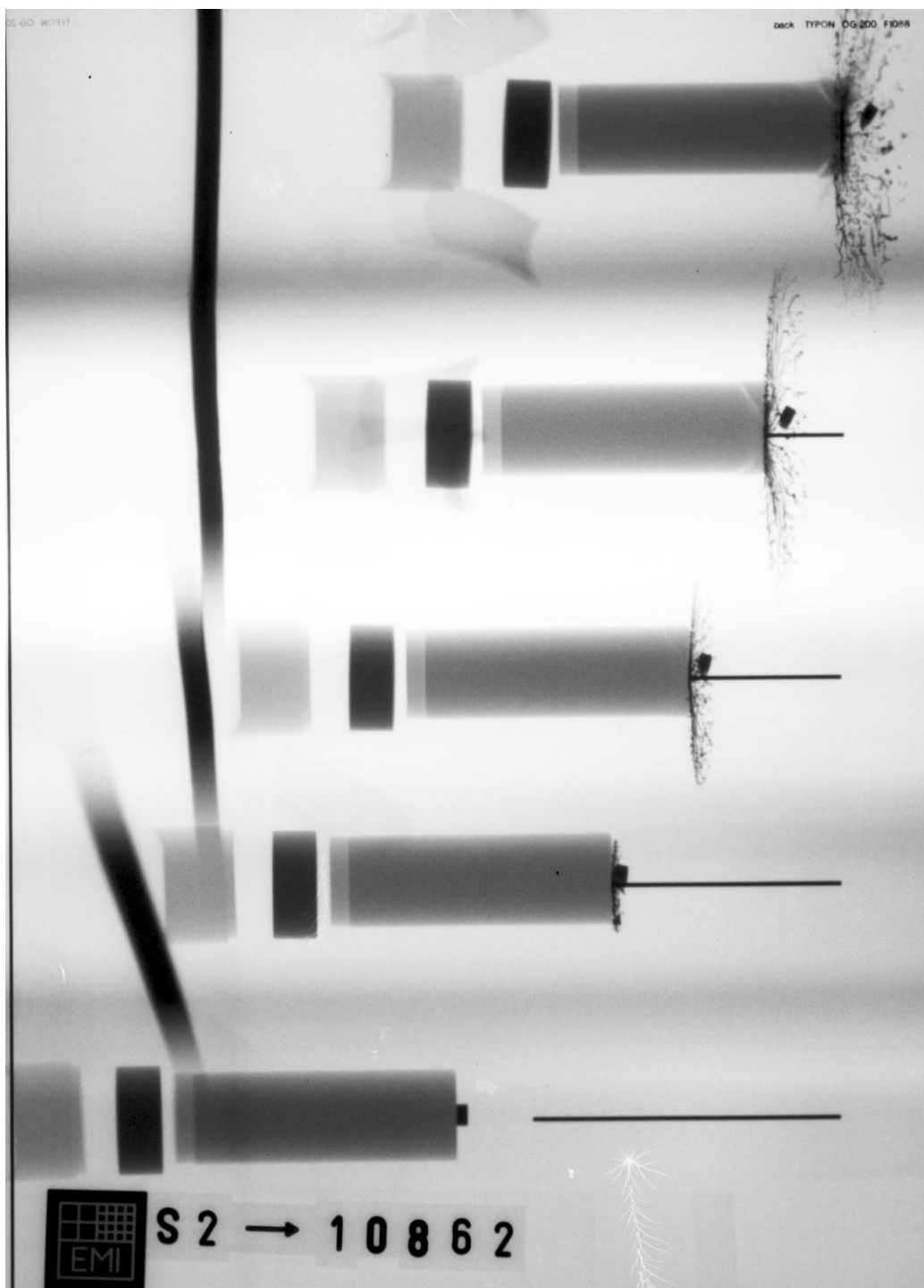
Figure A-28. X-ray picture for Exp. 10862: buffered glass, v_p = 890 m/s.
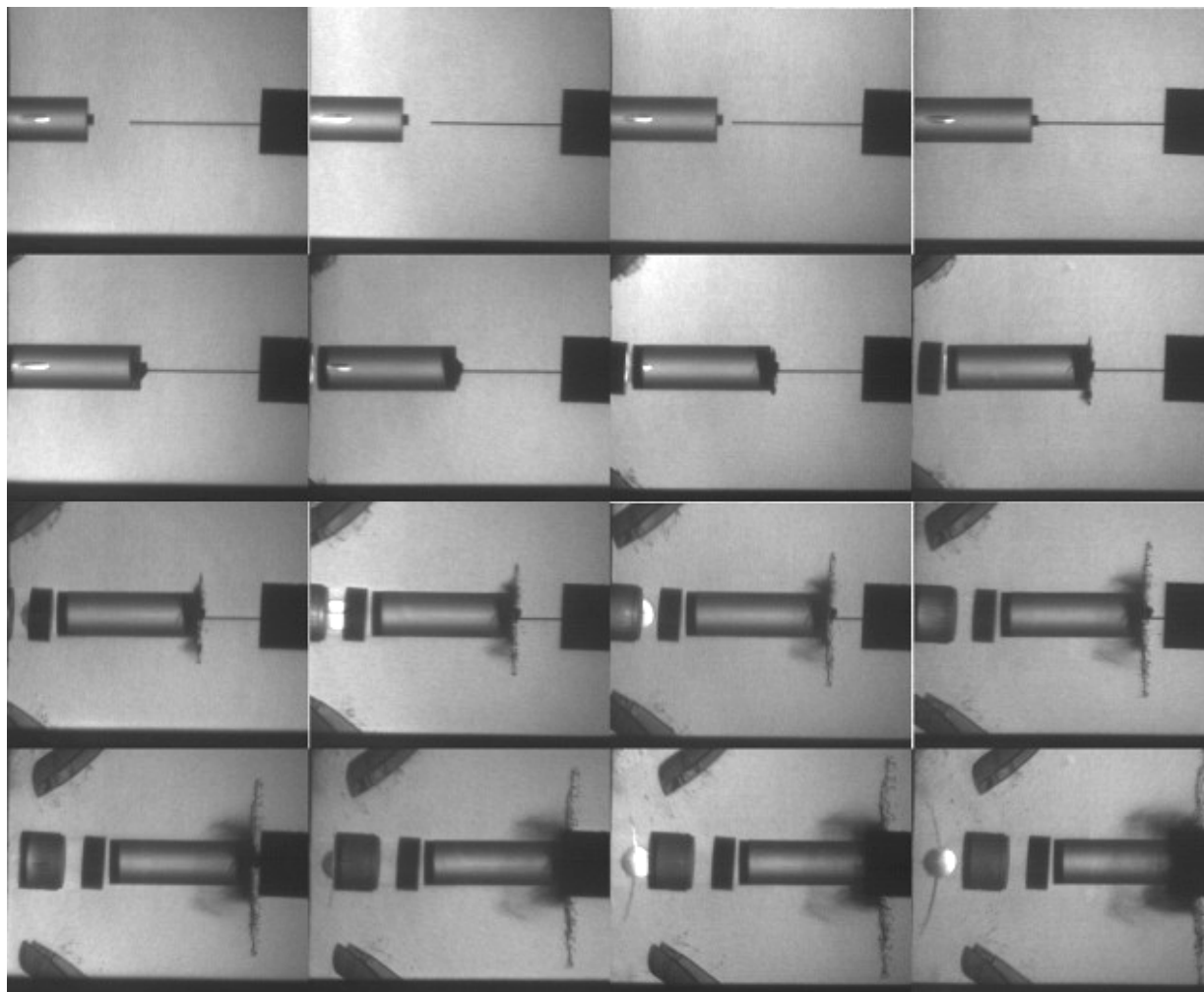
Figure A-29. Camera picture for Exp. 10862: buffered glass, $v_p = 890$ m/s.
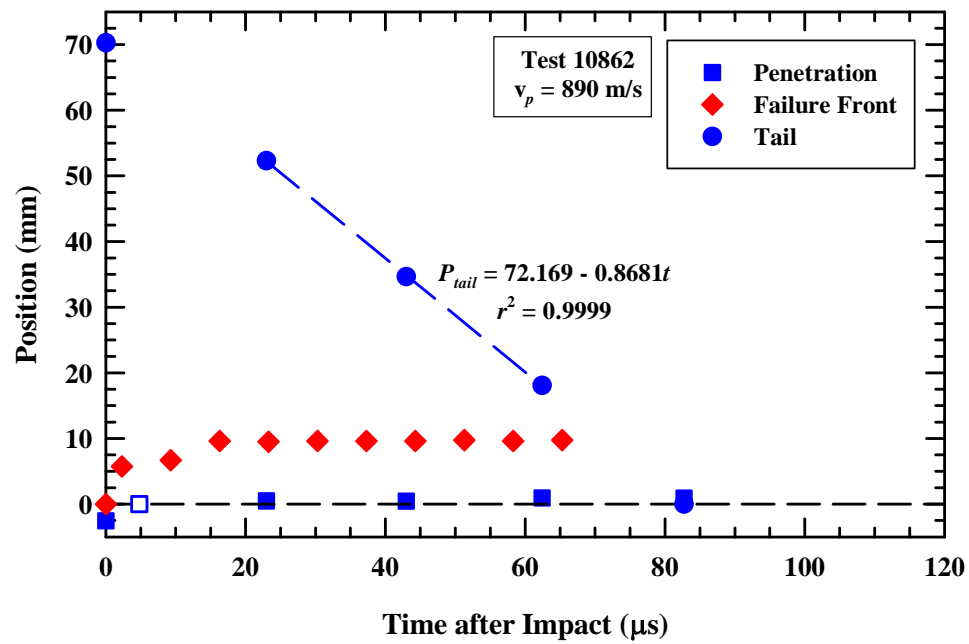
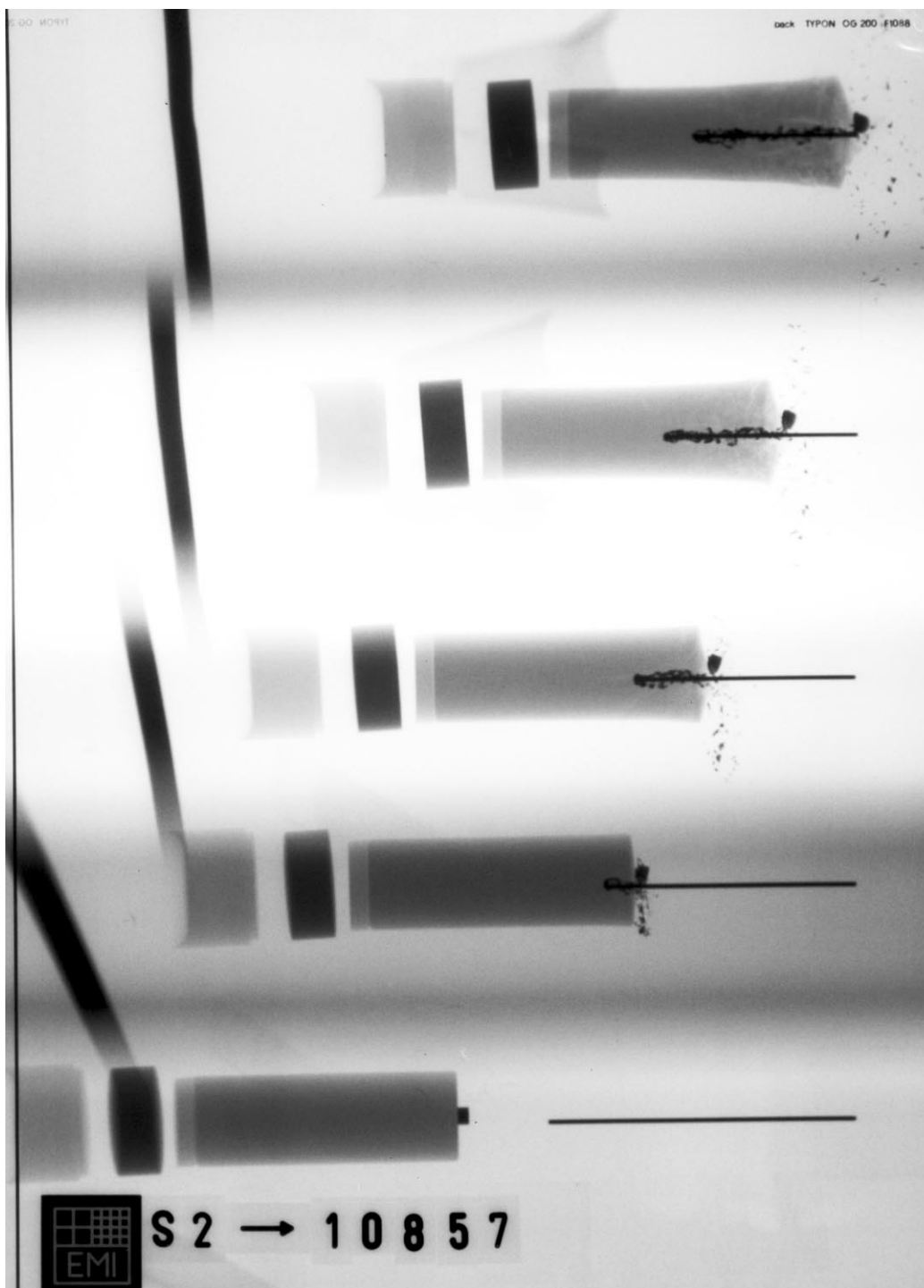**Figure A-30. Position vs. time for rod nose, tail, and failure front, Exp. 10862.**

Figure A-31. X-ray picture for Exp. 10852: buffered glass, v_p = 616 m/s.
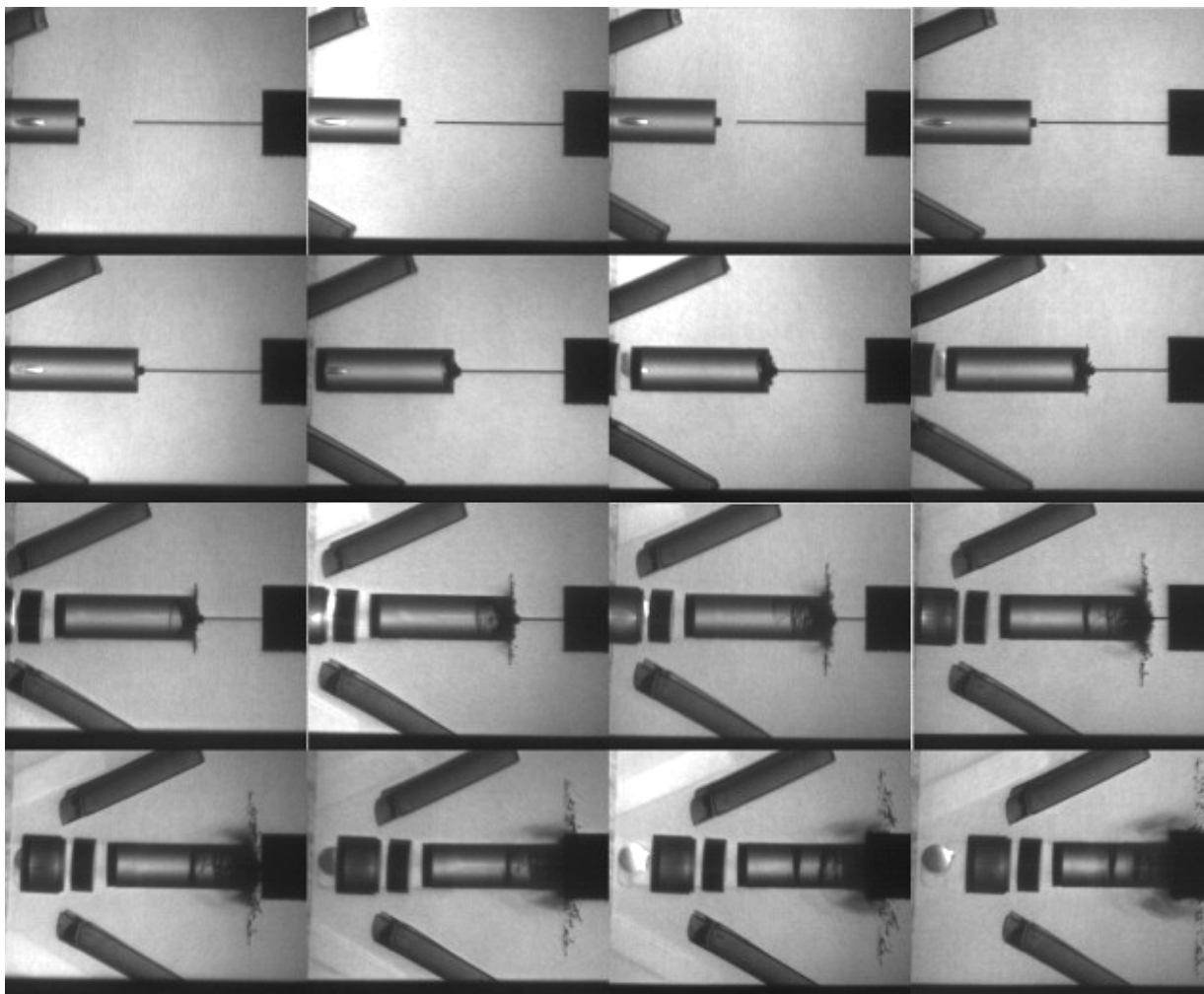
Figure A-32. Camera picture for Exp. 10852: buffered glass, v_p = 616 m/s.
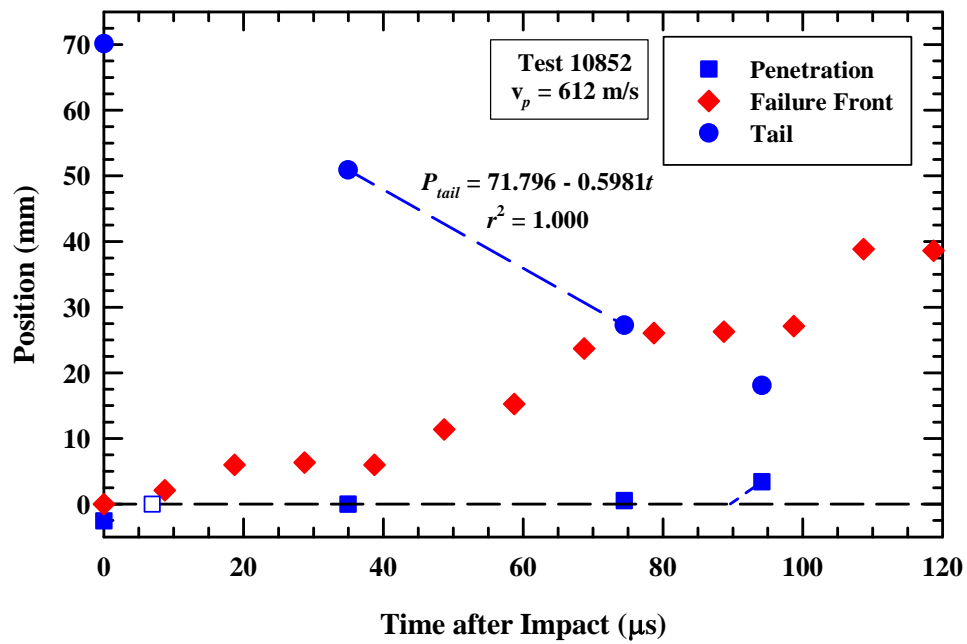
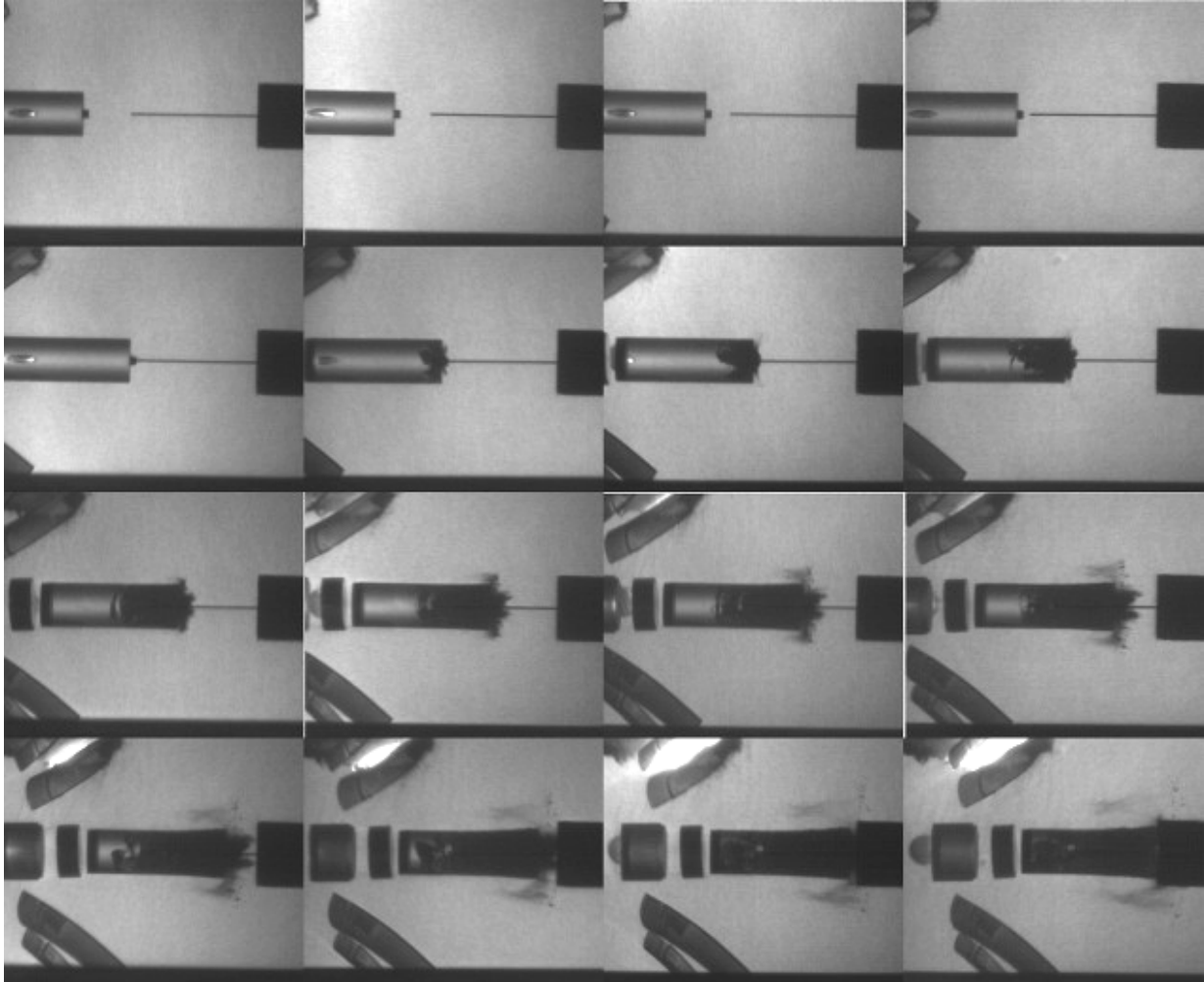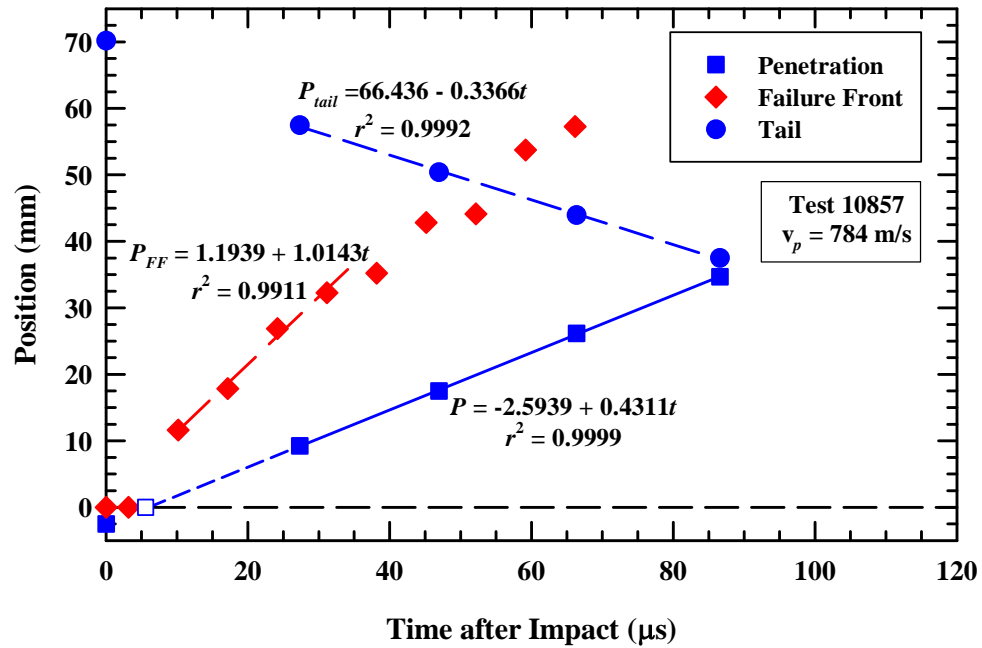**Figure A-33. Position vs. time for rod nose, tail, and failure front, Exp. 10852.**
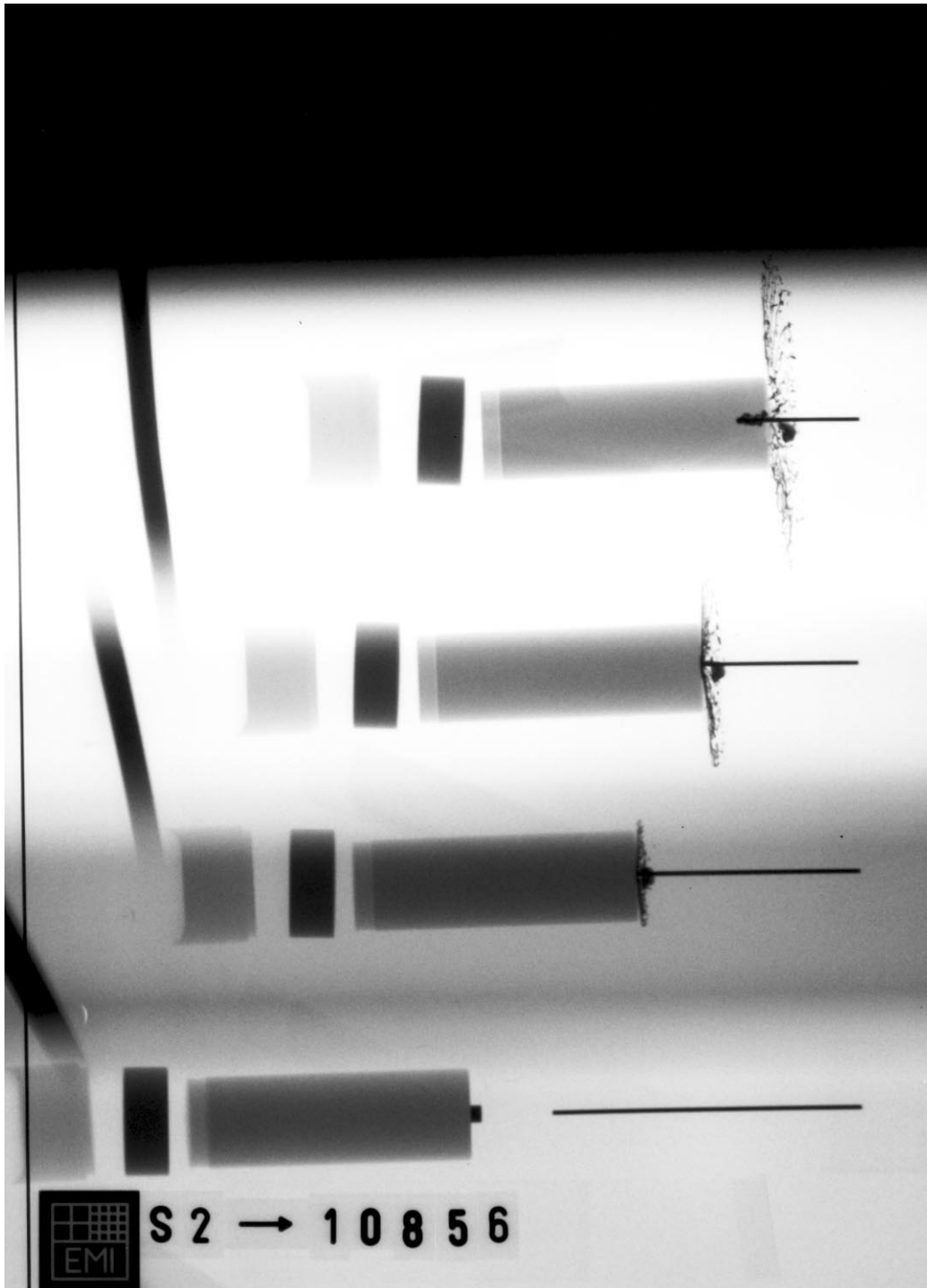
Figure A-34. X-ray picture for Exp. 10856: buffered glass, v_p = 770 m/s.
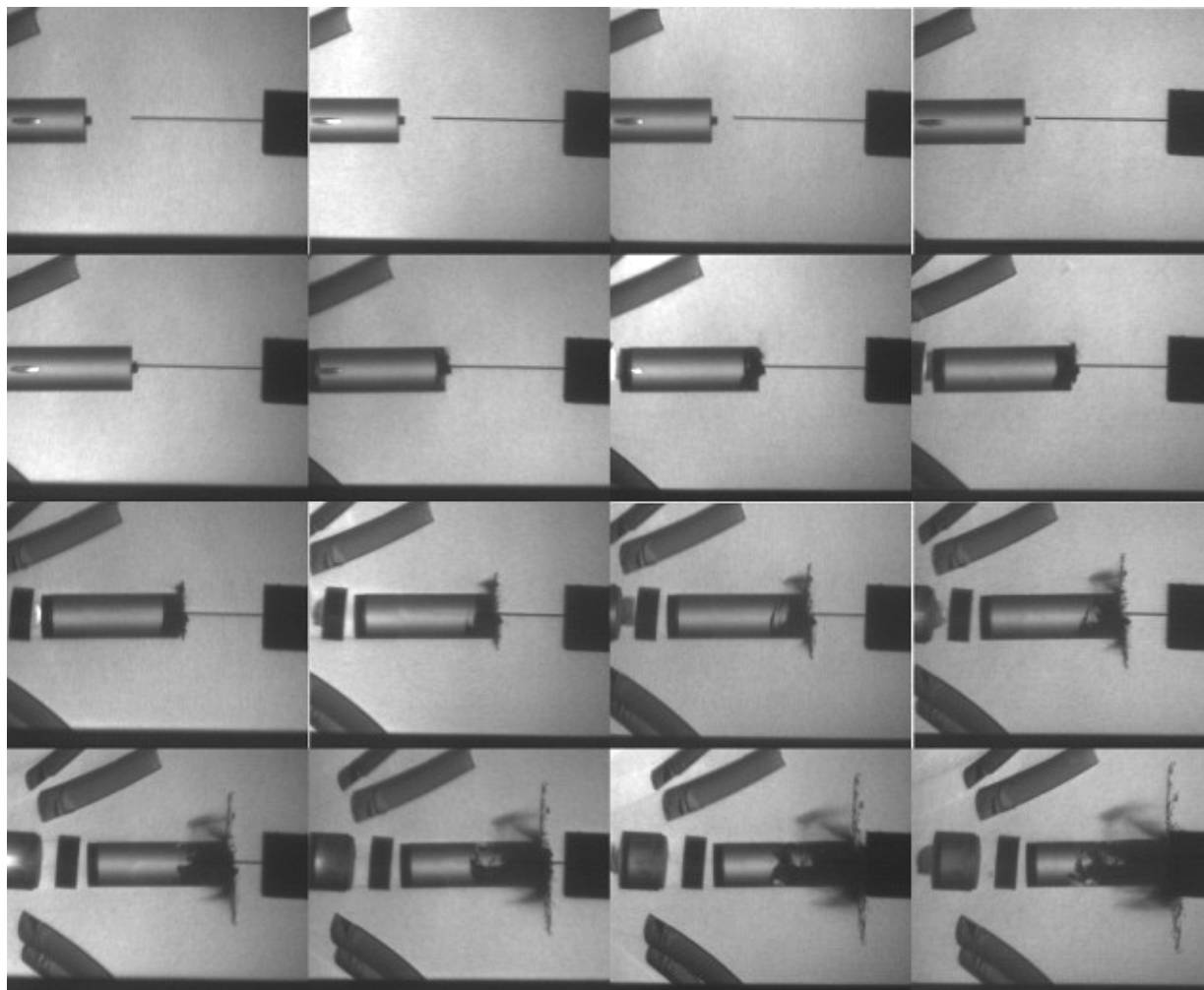
Figure A-35. Camera picture for Exp. 10856: buffered glass, v_p = 770 m/s.

Figure A-36. Position vs. time for rod nose, tail, and failure front, Exp. 10856.

Figure A-37. X-ray picture for Exp. 10861: buffered glass, $v_p = 816$ m/s.

Figure A-38. Camera picture for Exp. 10861: buffered glass, v_p = 816 m/s.

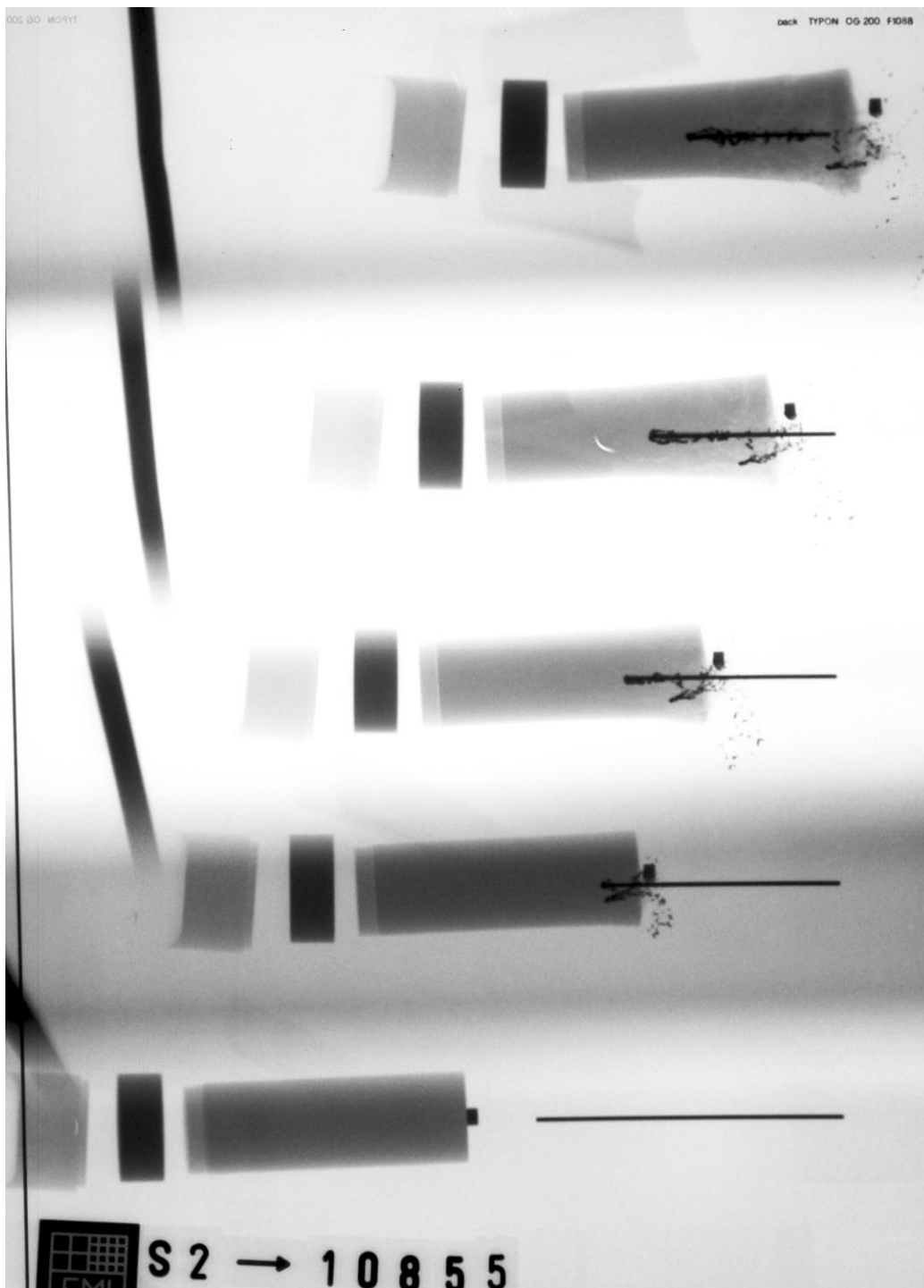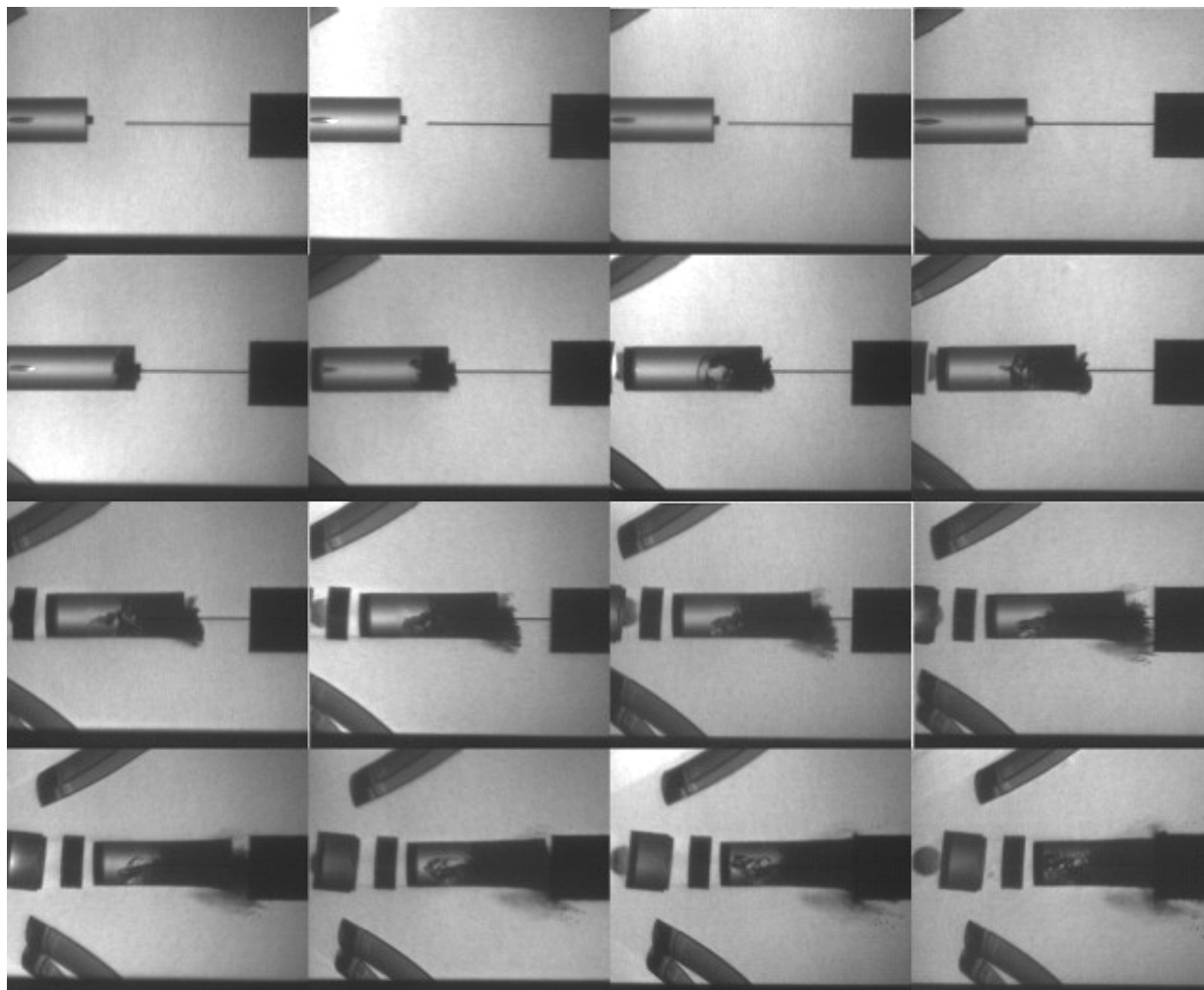**Figure A-39. Position vs. time for rod nose, tail, and failure front, Exp. 10861.**

Figure A-40. X-ray picture for Exp. 10860: buffered glass, v_p = 821 m/s.

Figure A-41. Camera picture for Exp. 10860: buffered glass, $v_p = 821$ m/s.

Figure A-42. Position vs. time for rod nose, tail, and failure front, Exp. 10860.

Figure A-43. X-ray picture for Exp. 10859: buffered glass, v_p = 837 m/s.

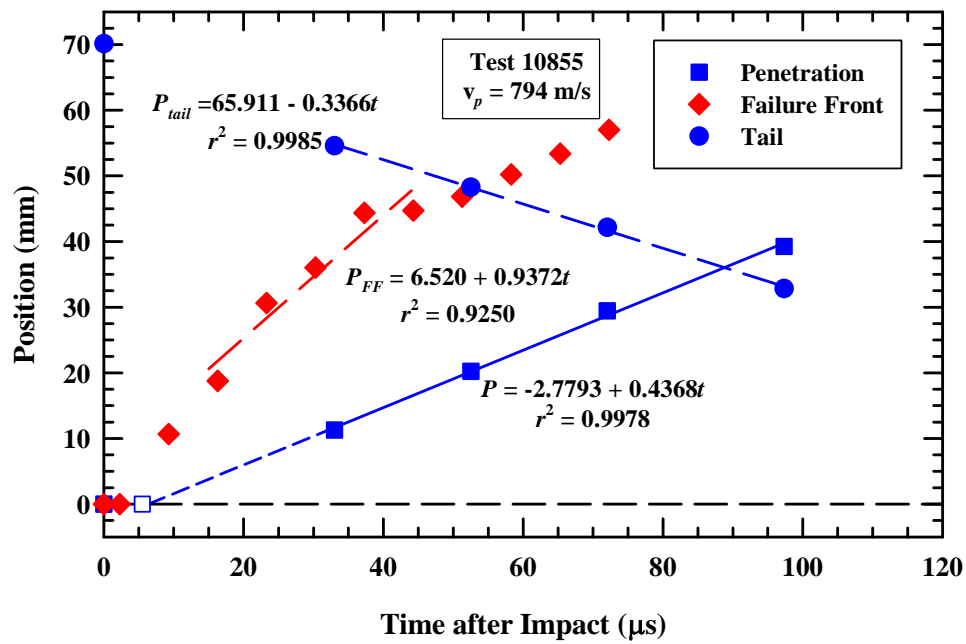**Figure A-44. Camera picture for Exp. 10859: buffered glass, $v_p = 837$ m/s.**

Figure A-45. Position vs. time for rod nose, tail, and failure front, Exp. 10859.

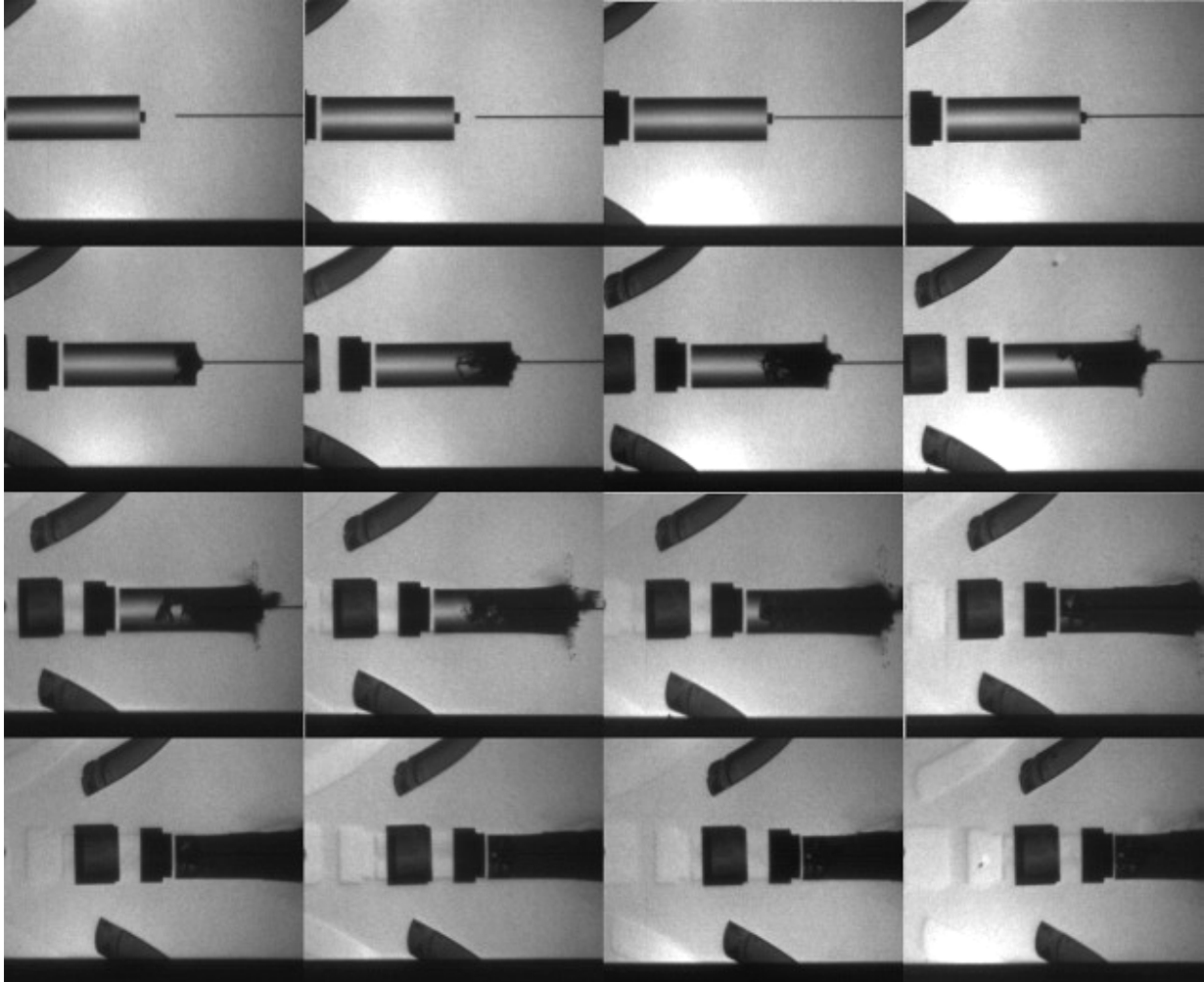**Figure A-46. X-ray picture for Exp. 11112: buffered glass, v_p = 869 m/s.**

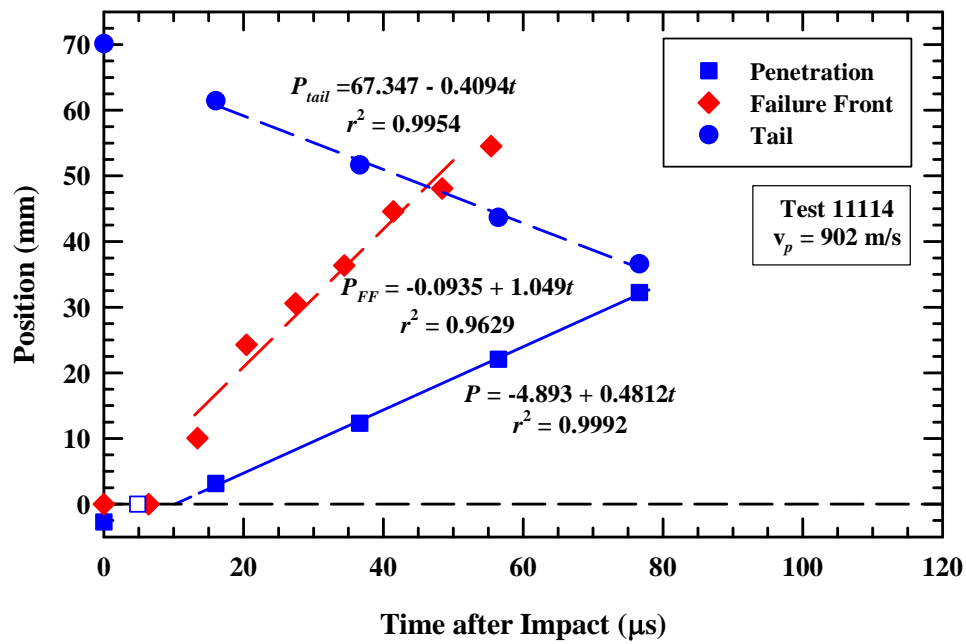**Figure A-47. Camera picture for Exp. 11112: buffered glass, v_p = 869 m/s.**

Figure A-48. Position vs. time for rod nose, tail, and failure front, Exp. 11112.

Figure A-49. X-ray picture for Exp. 10863: buffered glass, v_p = 882 m/s.

Figure A-50. Camera picture for Exp. 10863: buffered glass, v$_p$ = 882 m/s.

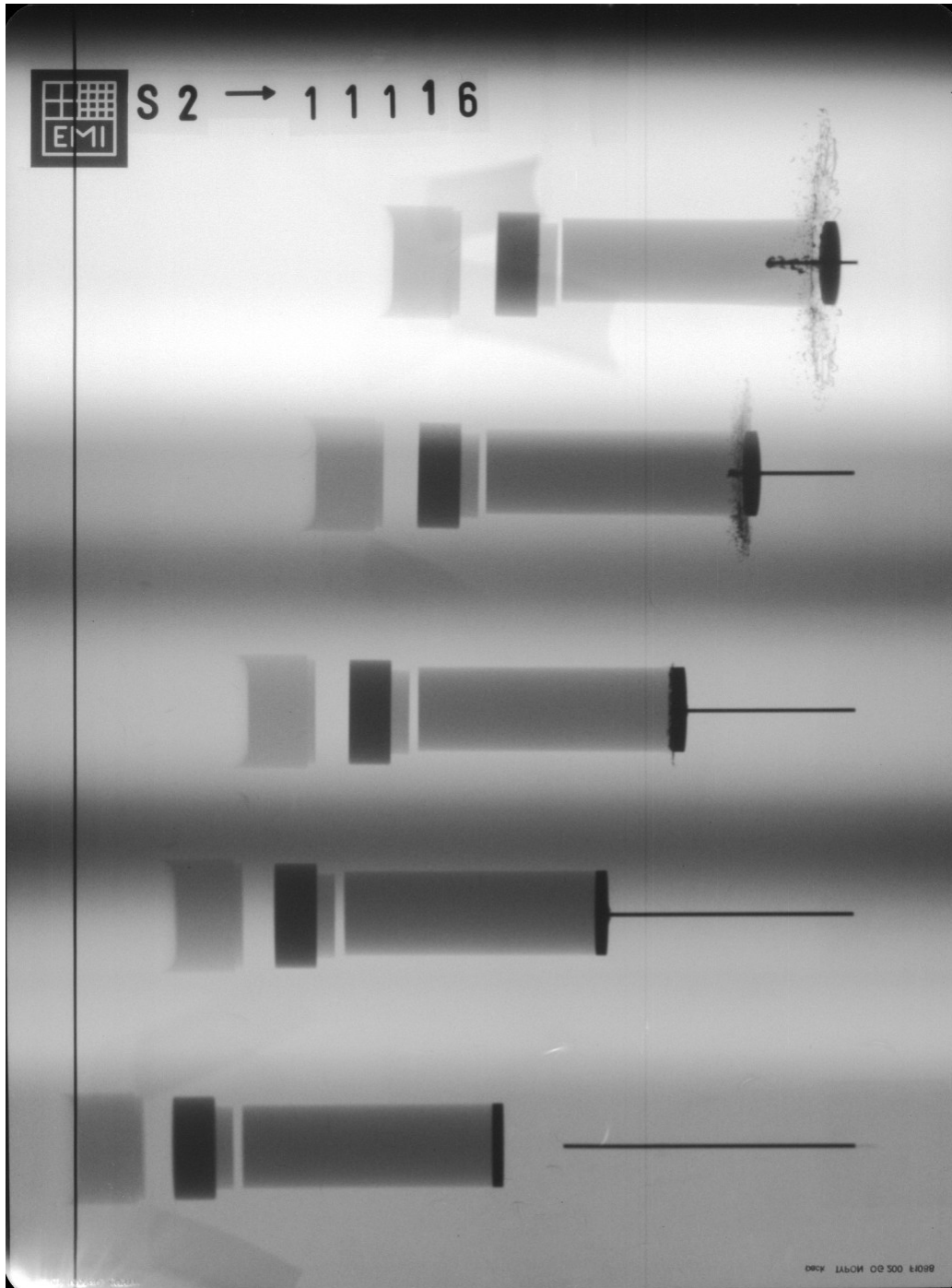**Figure A-51. Position vs. time for rod nose, tail, and failure front, Exp. 10863.**

Figure A-52. X-ray picture for Exp. 10851: buffered glass, v_p = 611 m/s.

Figure A-53. Camera picture for Exp. 10851: buffered glass, v_p = 611 m/s.

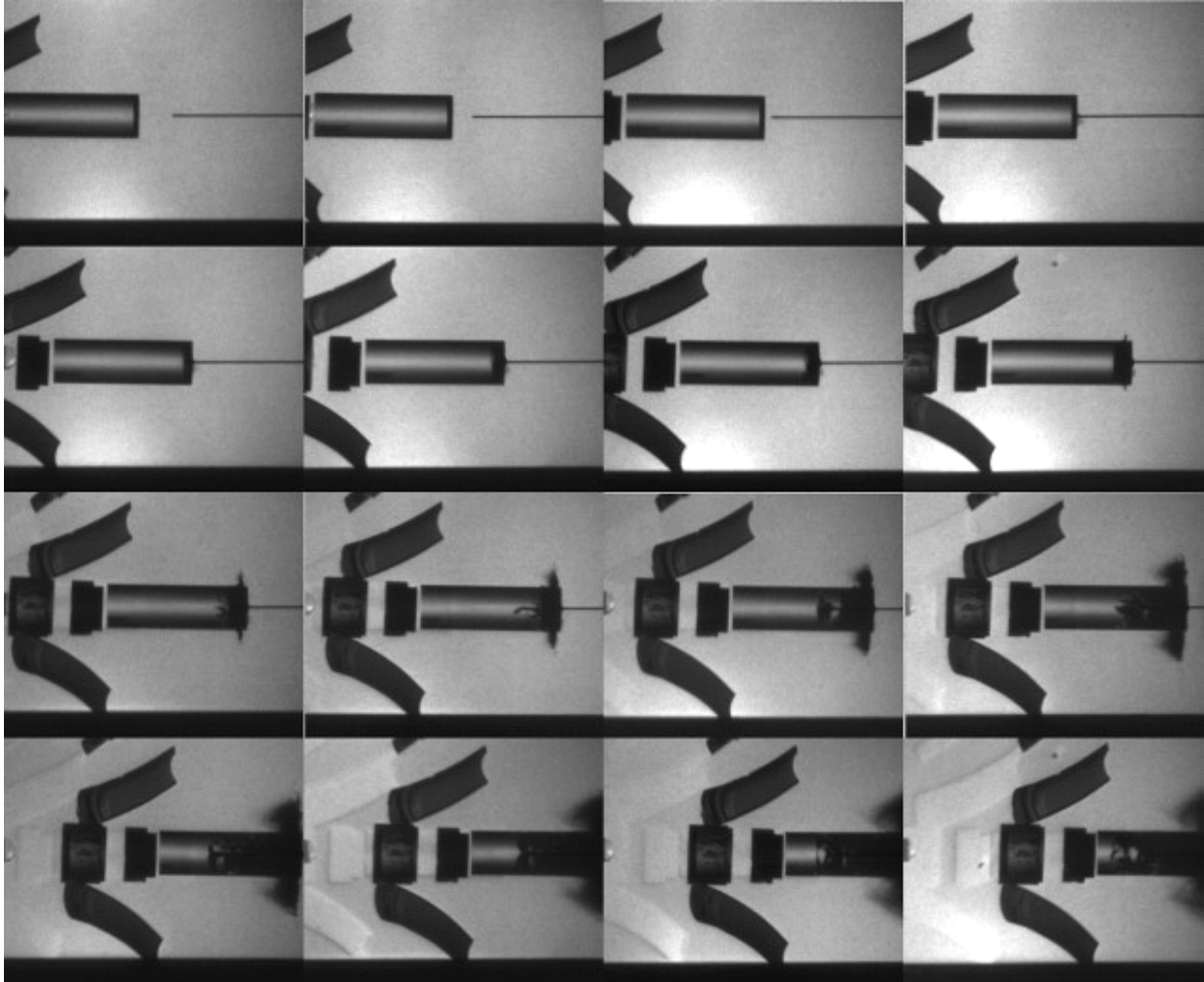**Figure A-54. Position vs. time for rod nose, tail, and failure front, Exp. 10851.**

Figure A-55. X-ray picture for Exp. 10857: buffered glass, $v_p = 784$ m/s.

**Figure A-56. Camera picture for Exp. 10857: buffered glass, v_p = 784 m/s.**

Figure A-57. Position vs. time for rod nose, tail, and failure front, Exp. 10857.

Figure A-58. X-ray picture for Exp. 10855: buffered glass, $v_p = 794$ m/s.

Figure A-59. Camera picture for Exp. 10855: buffered glass, $v_p = 794$ m/s.

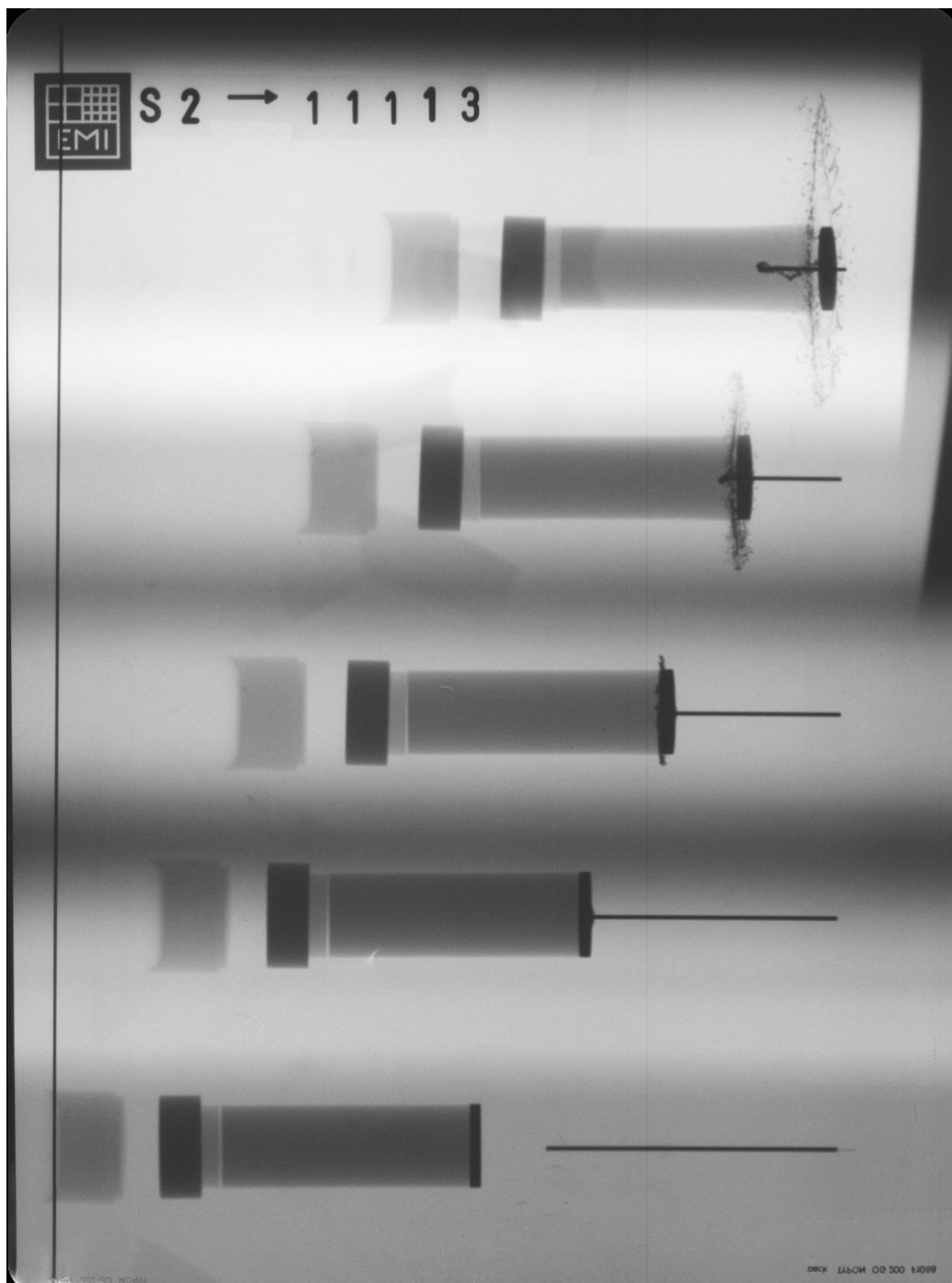**Figure A-60. Position vs. time for rod nose, tail, and failure front, Exp. 10855.**

Figure A-61. X-ray picture for Exp. 11114: buffered glass, $v_p = 902$ m/s.

Figure A-62. Camera picture for Exp. 11114: buffered glass, v_p = 902 m/s.

Figure A-63. Position vs. time for rod nose, tail, and failure front, Exp. 11114.

Figure A-64. X-ray picture for Exp. 11116: cover plate glass, v_p = 856 m/s.
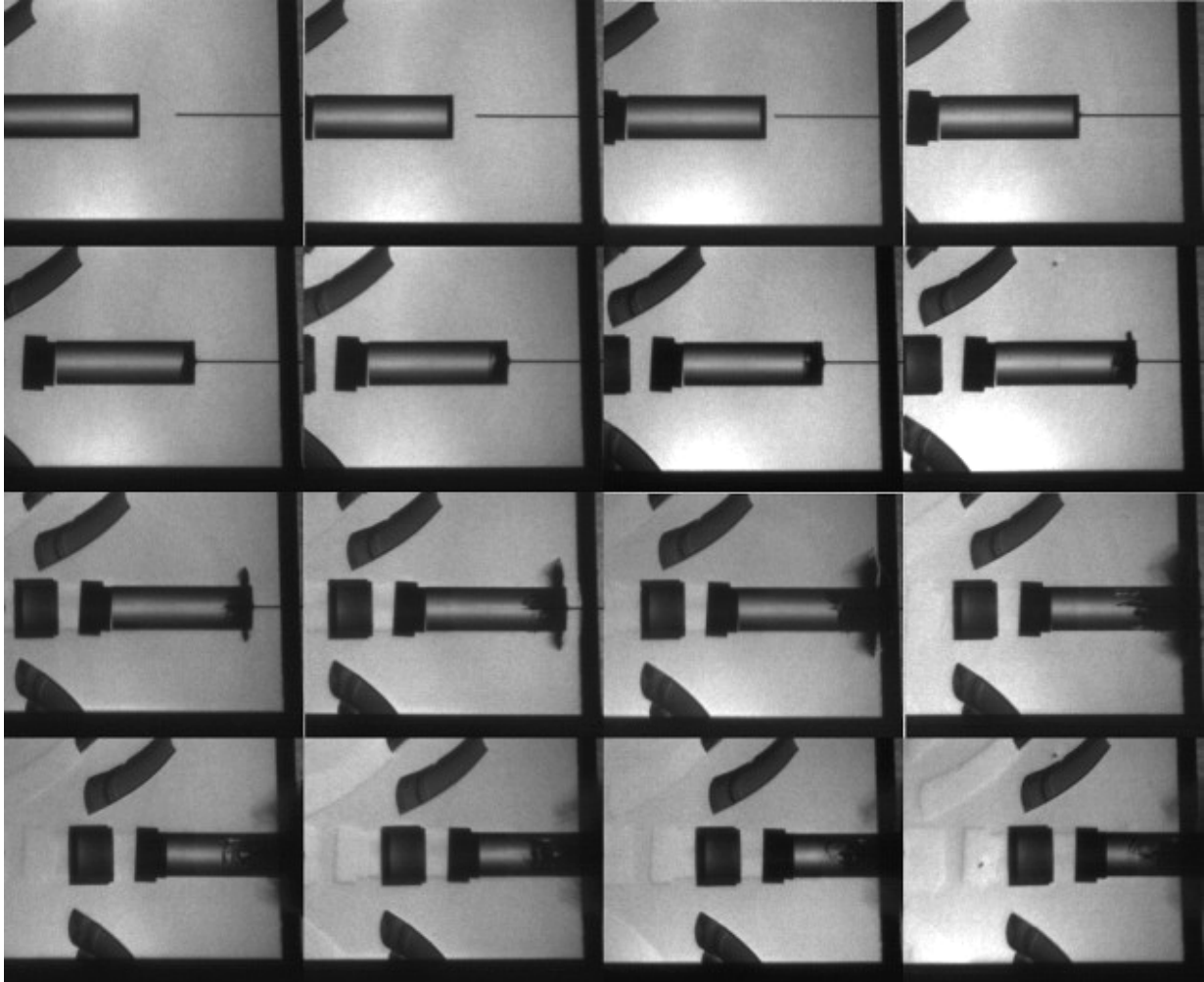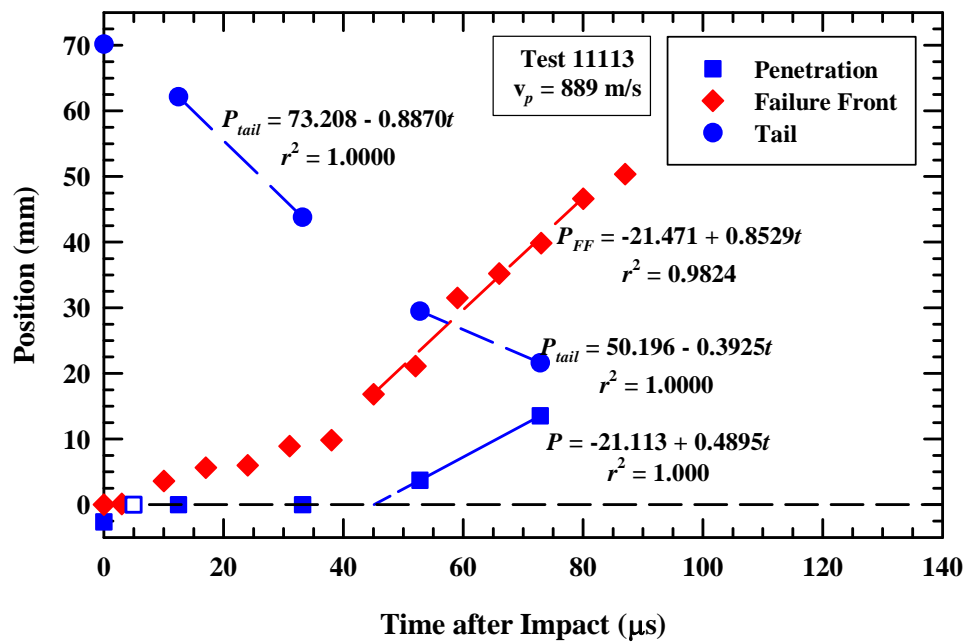
Figure A-65. Camera picture for Exp. 11116: cover plate glass, v_p = 856 m/s.
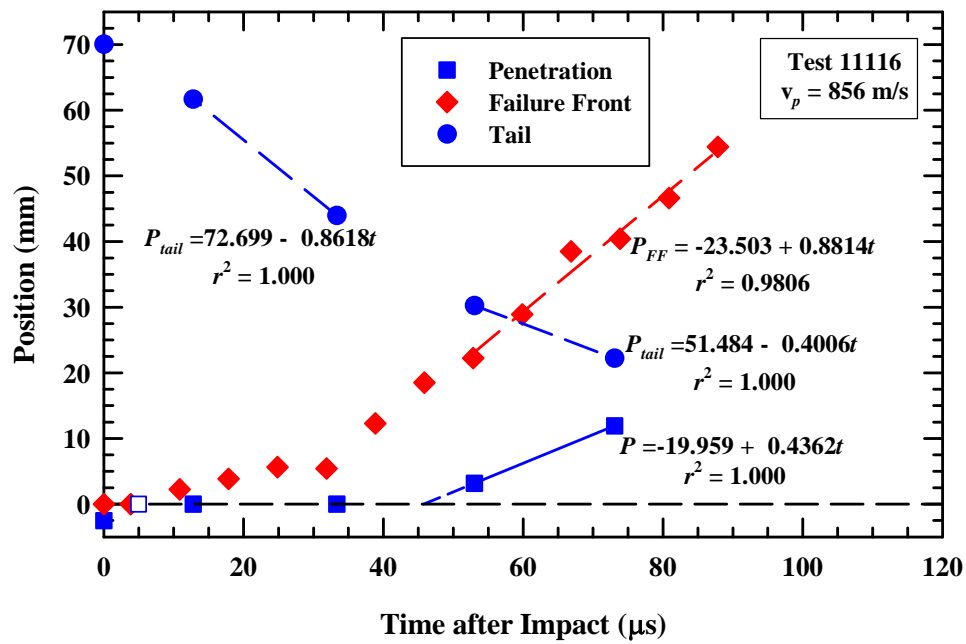
Figure A-66. Position vs. time for rod nose, tail, and failure front, Exp. 11116.

Figure A-67. X-ray picture for Exp. 11113: cover plate glass, v_p = 889 m/s.

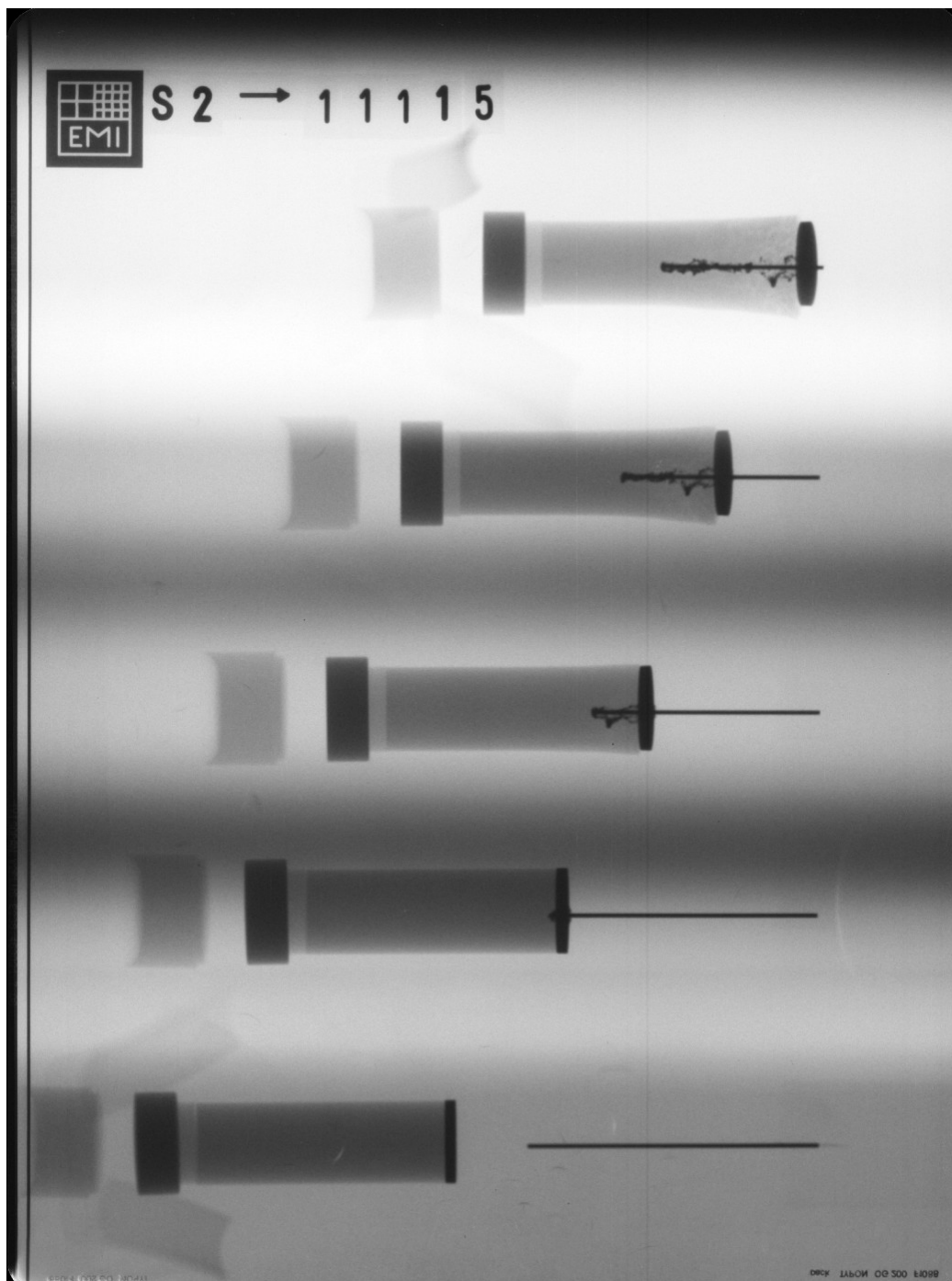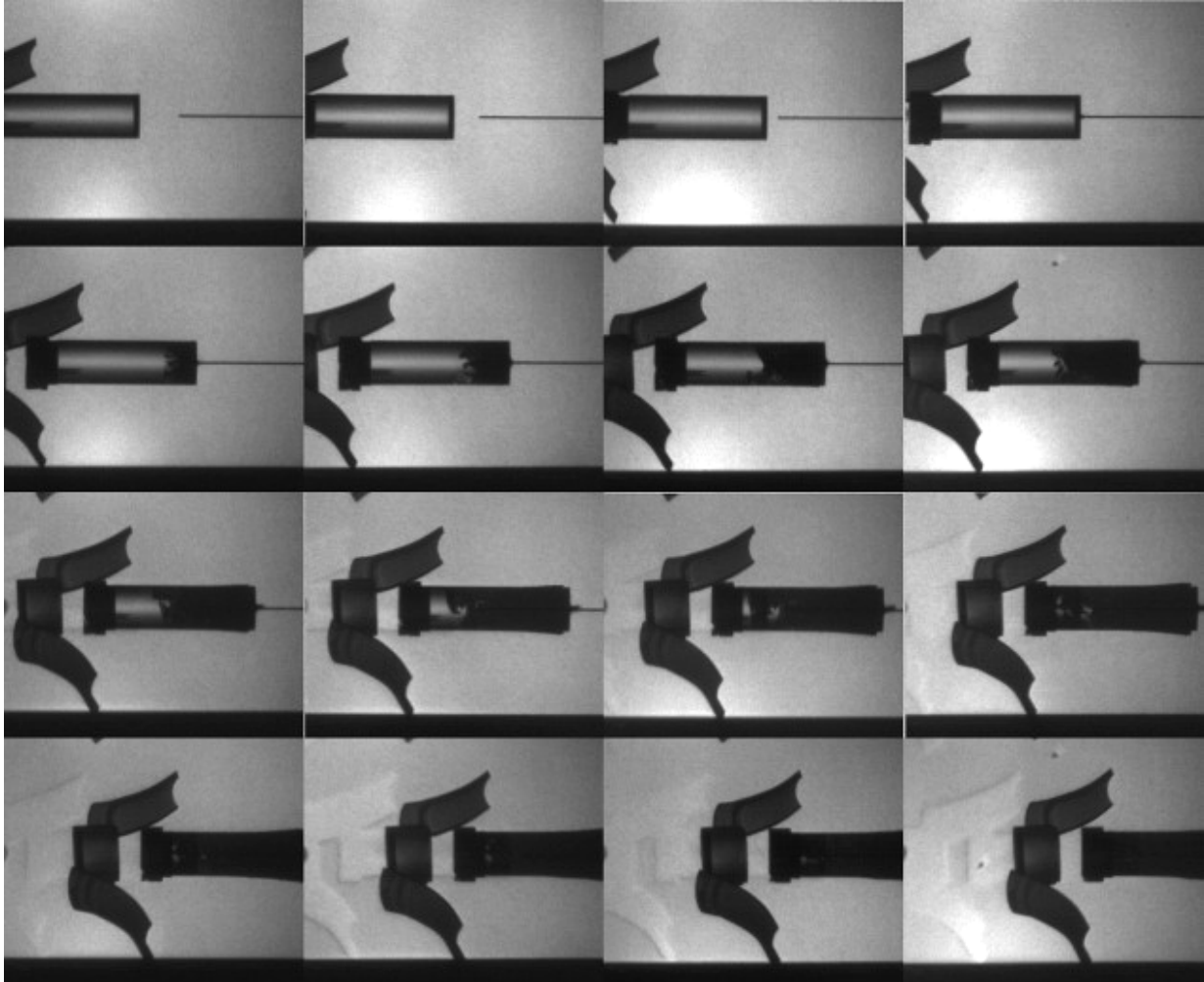**Figure A-68. Camera picture for Exp. 11113: cover plate glass, $v_p = 889$ m/s.**

Figure A-69. Position vs. time for rod nose, tail, and failure front, Exp. 11113.

Figure A-70. X-ray picture for Exp. 11115: cover plate glass, $v_p = 912$ m/s.

A-79

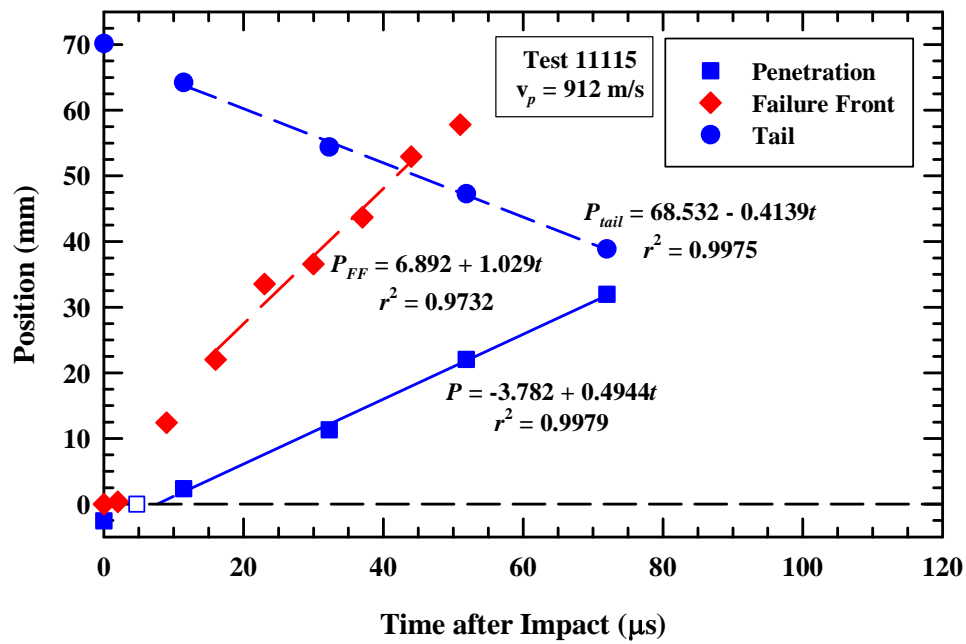**Figure A-71. Camera picture for Exp. 11115: cover plate glass, v_p = 912 m/s.**

Figure A-72. Position vs. time for rod nose, tail, and failure front, Exp. 11115.

A-82